

วิธีเชิงตัวเลขบนพื้นฐานของวิธีการเคอร์คินไม่ต่อเนื่องและปริมาตรอันตะสำหรับแบบจำลองการไหลน้ำใต้ดิน
และการประยุกต์

นางสาวธิดา พงศ์สงวนสิน

วิทยานิพนธ์นี้เป็นส่วนหนึ่งของการศึกษาตามหลักสูตรปริญญาวิทยาศาสตรดุษฎีบัณฑิต
สาขาวิชาคณิตศาสตร์ประยุกต์และวิทยาการคอมพิวเตอร์ ภาควิชาคณิตศาสตร์ และวิทยาการคอมพิวเตอร์
คณะวิทยาศาสตร์ จุฬาลงกรณ์มหาวิทยาลัย
ปีการศึกษา 2559
ลิขสิทธิ์ของจุฬาลงกรณ์มหาวิทยาลัย

บทคัดย่อและแฟ้มข้อมูลฉบับเต็มของวิทยานิพนธ์ตั้งแต่ปีการศึกษา 2554 ที่ให้บริการในคลังปัญญาจุฬาฯ (CUIR)
เป็นแฟ้มข้อมูลของนิสิตเจ้าของวิทยานิพนธ์ที่ส่งผ่านทางบัณฑิตวิทยาลัย

The abstract and full text of theses from the academic year 2011 in Chulalongkorn University Intellectual Repository (CUIR)
are the thesis authors' files submitted through the Graduate School.

NUMERICAL METHODS BASED ON DISCONTINUOUS GALERKIN AND
FINITE VOLUME METHODS FOR SHALLOW WATER MODEL AND
APPLICATIONS

Miss Thida Pongsanguansin

A Dissertation Submitted in Partial Fulfillment of the Requirements
for the Degree of Doctor of Philosophy Program in Applied Mathematics and
Computational Science

Department of Mathematics and Computer Science

Faculty of Science

Chulalongkorn University

Academic Year 2016

Copyright of Chulalongkorn University

Thesis Title Numerical methods based on discontinuous Galerkin and
 finite volume methods for shallow water model and applications
By Miss Thida Pongsanguansin
Field of Study Applied Mathematics and Computational Science
Thesis Advisor Assistant Professor Khamron Mekchay, Ph.D.
Thesis Co-advisor Associate Professor Montri Maleewong, Ph.D.

Accepted by the Faculty of Science, Chulalongkorn University in Partial
Fulfillment of the Requirements for the Doctoral Degree

.....Dean of the Faculty of Science
(Associate Professor Polkit Sangvanich, Ph.D.)

THESIS COMMITTEE

.....Chairman
(Associate Professor Pornchai Satravaha, Ph.D.)

.....Dissertation Advisor
(Assistant Professor Khamron Mekchay, Ph.D.)

.....Dissertation Co-advisor
(Associate Professor Montri Maleewong, Ph.D.)

.....Examiner
(Assistant Professor Petarpa Boonserm, Ph.D.)

.....Examiner
(Assistant Professor Ratinan Boonklurb, Ph.D.)

.....External Examiner
(Sekson Sirisubtawee, Ph.D.)

ธิดา พงศ์สงวนสิน : วิธีเชิงตัวเลขบนพื้นฐานของวิธีกาลเออร์กินไม่ต่อเนื่องและปริมาตร
 อันตะสำหรับแบบจำลองการไหลน้ำตื้นและการประยุกต์ (NUMERICAL METHODS
 BASED ON DISCONTINUOUS GALERKIN AND FINITE VOLUME METHODS FOR
 SHALLOW WATER MODEL AND APPLICATIONS) อ.ที่ปรึกษาวิทยานิพนธ์หลัก : ผศ.
 ดร. คำรณ เมฆฉาย อ.ที่ปรึกษาวิทยานิพนธ์ร่วม : รศ.ดร. มนตรี มาลีวงศ์, 109 หน้า.

สมการน้ำตื้นสามารถนำมาใช้ในการจำลองการไหลต่างๆในปัญหาจริงได้มากมาย เช่น
 ปัญหาเขื่อนแตก สึนามิ หรือน้ำท่วม ในวิทยานิพนธ์เล่มนี้เราทำการพัฒนาวิธีเชิงตัวเลขสามวิธีเพื่อใช้
 ในการหาผลเฉลยของสมการดังกล่าว วิธีแรกคือวิธีเวลบาลานซ์กาลเออร์กินไม่ต่อเนื่องโดยใช้ฟังก์ซ์
 เฉลี่ยแบบถ่วงน้ำหนักสำหรับสมการน้ำตื้นในหนึ่งมิติ วิธีที่สองพัฒนาขึ้นเพื่อให้ได้ผลที่สมจริงยิ่งขึ้น
 สำหรับการไหลในหนึ่งมิติ เมื่อพิจารณาสมการน้ำตื้นในหนึ่งมิติสำหรับพื้นที่หน้าตัดใดๆ บนพื้นฐาน
 ของวิธีปริมาตรอันตะ และวิธีที่สามพัฒนาสำหรับการไหลในโลกจริง โดยพิจารณาสมการน้ำตื้นสอง
 มิติ บนพื้นฐานของวิธีเวลบาลานซ์ปริมาตรอันตะโดยใช้ฟังก์ซ์เฉลี่ยแบบถ่วงน้ำหนัก

ภาควิชาคณิตศาสตร์และ.....	ลายมือชื่อนิติศ.....
	..วิทยาการคอมพิวเตอร์..	
สาขาวิชา	..คณิตศาสตร์ประยุกต์..	ลายมือชื่อ อ.ที่ปรึกษาหลัก.....
	...และวิทยาการคณนา...	ลายมือชื่อ อ.ที่ปรึกษาร่วม.....
ปีการศึกษา2559.....	

5572818823 : MAJOR APPLIED MATHEMATICS AND COMPUTATIONAL SCIENCE

KEYWORDS : DISCONTINUOUS GALERKIN METHOD / FINITE VOLUME METHOD / SHALLOW WATER EQUATIONS

THIDA PONGSANGUANSIN : NUMERICAL METHODS BASED ON DISCONTINUOUS GALERKIN AND FINITE VOLUME METHODS FOR SHALLOW WATER MODEL AND APPLICATIONS. ADVISOR : ASST. PROF. KHAMRON MEKCHAY, PH.D. COADVISOR : ASSOC. PROF. MONTRI MALEEWONG, PH.D., 109 pp.

Shallow water equations (SWE) can be used to model many real flow problems such as dam break, tsunami and flood. In this dissertation, we have developed three numerical schemes for solving these equations. The first scheme is the well-balanced discontinuous Galerkin (DG) method with weighted average flux (WAF) for one-dimensional SWE. The second scheme is developed to obtain more realistic results for the one-dimensional flow, where the one-dimensional SWE is considered for arbitrary cross-sectional areas, based on the finite volume method (FVM). And the third scheme is developed to solve real world flows by considering the two-dimensional SWE based on the well-balanced FVM with WAF.

Department :Mathematics..... Student's Signature :
and Computer Science....
 Field of Study :Applied Mathematics..... Advisor's Signature :
 ..and Computational Science.. Co-advisor's Signature :
 Academic Year :2016.....

ACKNOWLEDGEMENTS

First and foremost, I am greatly indebted to my advisor, Assistant Professor Khamron Mekchay, Ph.D., and co-advisor, Associate Professor Montri Maleewong, Ph.D. They kindly offered many useful suggestion and advice in this thesis. Moreover, they always willingly to support, encourage and teach me not only the technical knowledge, but also other life lessons.

I would like to express sincere thanks to my thesis committee, Associate Professor Pornchai Satravaha, Ph.D., Assistant Professor Petarpa Boonserm, Ph.D., Assistant Professor Ratinan Boonklurb, Ph.D., and Sekson Sirisubtawee, Ph.D. for reading the dissertation and offering helpful comments on the suitability of the dissertation content.

I sincerely thank all of my teachers at Department of Mathematics and Computer Science, Chulalongkorn University and Department of Mathematics, Kasetsart University, who have taught me knowledge and skills, and special thank to Associate Professor Anand Pardhanani, Ph.D. from Department of Mathematics, Earlham college, Indiana, USA. for his advices. I also thank all of my friends who always encouraged me.

Moreover, I am thankful to the Science Achivement Scholarship Thailand (SAST) for their financial support since I was an undergraduate student.

Finally, I would like to express my deep gratitude to my family, who have always loved, encouraged, supported everything, and stood by me. I am especially indebted to my parents who gave many helpful suggestions which made it possible for me to get through the difficult times. This dissertation is dedicated to my family.

CONTENTS

	page
ABSTRACT IN THAI	iv
ABSTRACT IN ENGLISH	v
ACKNOWLEDGEMENTS	vi
CONTENTS	vii
LIST OF TABLES	ix
LIST OF FIGURES	xi
CHAPTER	
I INTRODUCTION	1
II SHALLOW WATER EQUATIONS	4
2.1 The one-dimensional SWE	4
2.2 The one-dimensional SWE in arbitrary cross-sectional area	9
2.3 The two-dimensional SWE	15
III WELL-BALANCED DISCONTINUOUS GALERKIN METHOD WITH WEIGHTED AVERAGE FLUX FOR ONE-DIMENSIONAL SHALLOW WATER EQUATIONS	17
3.1 Discontinuous Galerkin method (DG) for one-dimensional shallow water equations	17
3.1.1 Numerical flux	19
3.1.2 Total Variation Diminishing Runge-Kutta (TVD-RK)	24
3.1.3 Monotonic Upstream-Centered Scheme for Conservation Laws (MUSCL) slope limiter	25
3.2 Consistency of WAF with TVD-RK DG method	27
3.3 Well-balanced TVD-RK DG with WAF scheme	29
3.4 Numerical results	35
3.4.1 Dam break flow	35
3.4.2 Flow over irregular bed	37
3.4.3 Steady flow over a bump	38

	page
3.4.4 Small perturbation of steady state water	40
3.4.5 Flow over non-horizontal bed	42
3.5 Conclusions	43
IV FINITE VOLUME METHOD FOR ONE-DIMENSIONAL SHALLOW WATER EQUATIONS IN ARBITRARY CROSS-SECTIONAL AREA ...	44
4.1 Finite volume method for one-dimensional shallow water equations in arbitrary cross-sectional area	44
4.1.1 Harten-Lax-van Leer flux (HLL flux)	46
4.1.2 An approximation of source term	47
4.2 Reconstruction and bottom modification techniques for wet/dry problems	48
4.3 Numerical Results	51
4.3.1 Dam break in various channels	51
4.3.2 Still water in parabolic channel	55
4.3.3 Riemann problem in non-prismatic channel	57
4.3.4 Oscillatory flow in a parabolic bowl without friction effects	59
4.3.5 Dam break flow over a discontinuous bottom	60
4.3.6 Vacuum occurrence by a double rarefaction wave over a step	63
4.3.7 Unsteady dam break flow in adverse slope channel	65
4.3.8 Simulation of the flow in the Yom river	66
4.4 Conclusions	70
V WELL-BALANCED FINITE VOLUME METHOD WITH WEIGHTED AVERAGE FLUX FOR TWO-DIMENSIONAL SHALLOW WATER EQUATIONS	72
5.1 Finite volume method (FVM) for two-dimensional shallow water equations	72
5.1.1 Weighted average flux (WAF) for two-dimensional shallow water equations	74
5.1.2 Linear reconstruction	77

	page
5.2 Well-balanced scheme	78
5.3 Friction term approximations.....	80
5.4 Wet/dry tracking technique	81
5.5 Numerical results	82
5.5.1 Rectangular dam break without friction	82
5.5.2 2D circular dam break.....	85
5.5.3 Partial dam break.....	87
5.5.4 Rectangular dam break with friction.....	88
5.5.5 Well-balanced test in two-dimensions.....	89
5.5.6 Subcritical flows over a bump	90
5.5.7 Dam break flows over a trapezoidal bump	92
5.5.8 Dam break flows over three humps	93
5.5.9 Flood simulation in Thailand, 2011.....	95
5.6 Conclusions	101
VI CONCLUSIONS	103
REFERENCES	104
VITA	109

LIST OF TABLES

TABLE	page
3.1 RMS errors when $N = 0$, $N = 1$ and $N = 2$ for $K = 50, 100$ and 200 for WAF and HLL	36
3.2 RMS errors when $N = 1$ for subcritical flow over a bump for $K = 50,$ $100, 200$ and 400	38
5.1 The MAE and the RMSE for wet bed case.....	83
5.2 The MAE and the RMSE for dry bed case.....	84
5.3 The RMSE errors for subcritical flows over a bump	91
5.4 The MAE errors for subcritical flows over a bump	91
5.5 The measurement data of water heights and discharges average per day at c13 station on October 13-17, 2011	97

LIST OF FIGURES

FIGURE	page
2.1 One-dimensional control volume	4
2.2 Cross-section of channel	9
2.3 One-dimensional control volume for arbitrary cross-sectional area in channel	9
2.4 Control volume for two-dimensional problem, side view (left) top view (right)	16
3.1 The diagram for HLL flux corresponding to the Riemann problem at interface $i+1/2$	21
3.2 The diagram for WAF corresponding to the Riemann problem at interface $i+1/2$	21
3.3 Exact solution and water depth profile obtained by the TVD-RK DG with HLL flux	36
3.4 Exact solution and water depth profile obtained by the TVD-RK DG with WAF flux	37
3.5 Stationary flows over irregular bottom produced by well-balanced and non well-balanced TVD-RK DG with WAF	37
3.6 Water depth and bump profiles for subcritical flow	39
3.7 Transcritical flow with shock over a bump	39
3.8 Transcritical flow without shock over a bump	40
3.9 Quasi-stationary flow for $\epsilon = 0.01$	41
3.10 Quasi-stationary flow for $\epsilon = 0.2$	41
3.11 Flows over non-horizontal bed at time 1s	42
3.12 Flows over non-horizontal bed at time 4s	43
4.1 Cross-section of a channel	45
4.2 The wave structure diagram for HLL corresponding to the Riemann problem	47
4.3 The limits from the left and the right of the variable h for cell i at	

FIGURE	page
interface $i - 1/2$ and $i + 1/2$	49
4.4 The cross-sectional areas of parabolic, triangular, and trapezoidal channel	52
4.5 Comparisons of the water depth (a) and the discharge (b) between the exact solutions and the approximate solutions at 20s for dam break in parabolic channel (wet bed problem)	52
4.6 Comparisons of the water depth (a) and the discharge (b) between the exact solutions and the approximate solutions at 20s for dam break in parabolic channel (dry bed problem)	53
4.7 Comparisons of the water depth (a) and the discharge (b) between the approximate solutions and the exact solutions at 80s for dam break flow in triangular channel (wet bed problem)	54
4.8 Comparisons of the water depth (a) and the discharge (b) between the exact solutions and the approximate solutions for dam break flow in trapezoidal channel	55
4.9 The still water with irregular bed in parabolic channel	55
4.10 The wet/dry still water with irregular bed in parabolic channel	56
4.11 The initial water surfaces for still water stationary solution problems	56
4.12 The simulated water surfaces for still water stationary solution problems	57
4.13 The comparisons of the water depth, the wetted area and the discharge between the exact solutions and the approximate solutions for Riemann problem in non-prismatic channel	58
4.14 The comparison of the water surface between the approximate solution and the exact solution for oscillatory flow in a parabolic bowl without friction effects	59
4.15 The comparison of the water surface between the approximate solution from scheme I with CFL=0.3962 and the exact solution	60
4.16 The steady state water surface of the dam break flow over a discontinuous bottom simulated by scheme II with $\Delta t = 0.001s$	61

FIGURE	page
4.17 The simulated water surface produced by scheme I with $\Delta t = 0.001s$	62
4.18 The simulated water surface produced by scheme I with smaller $\Delta t = 0.0005s$ at steady state	62
4.19 The comparison of the results from scheme I and II using $K = 500$ in area where the water depth from scheme I is negative	62
4.20 The approximate solution of the vacuum occurrence by a double rarefaction wave over a step at various times	64
4.21 The result of the vacuum occurrence by a double rarefaction wave over a step at various times from [12]	64
4.22 The comparisons between the simulated water depths and the laboratory results from [4] at various locations	66
4.23 The studied area of the Yom river from gauging stations Y20 to Y1C (blue line)	67
4.24 The bottom elevation of the Yom river from Y20 to Y1C	67
4.25 The cross-sectional areas of the gauging stations obtained from [53]	68
4.26 Examples of the cross-sectional areas at locations 1, 2, 3, and 4 in Figure 4.24 obtained from [16]	68
4.27 The numerical results for water depth and the discharge on August 27, 2014	69
4.28 The real measured data for the water surface and the discharge from August 27 to September 10, 2014 at Y20 station	70
4.29 The comparison of the simulated discharge and the real measured data from August 27 to September 10, 2014 at Y1C station	70
5.1 The grid discretization in two-dimension	73
5.2 The diagram for WAF corresponding to the Riemann problem	75
5.3 Flowchart of the wet/dry tracking algorithm	81
5.4 The change of the wet cells (cross) and the added neighboring cells (black) from first time step (left) to the second time step (right)	82
5.5 The domain of 2D circular dam break flow	85
5.6 Water surface in 3D plot (left) and its contour plot (right) for wet bed	

FIGURE	page
at $t = 3s$	86
5.7 Water surface in 3D plot (left) and its contour plot (right) for dry bed at $t = 3s$	87
5.8 Domain of the partial dam break problem	87
5.9 Water surface plot (left) and contour plot (right) of the partial dam break problem	88
5.10 The comparison of our numerical results with the results from [34]	88
5.11 Water surface profile for very large time	89
5.12 Subcritical flows over a bump from WAF with the linear reconstruction scheme when $K = 100$	90
5.13 Initial setup of dam break flows over a trapezoidal bump	92
5.14 The comparisons between numerical results and experimental data from [32] for dam break flows over a trapezoidal bump for various $T = 11.9,$ $17.54, 20.67, 23.05, 29.69,$ and 41.84	93
5.15 The water surface profile (left) and contour plot (right) of a dam break flows over three humps at $t = 12s$	94
5.16 Water surface profile of a dam break flows over three humps at $t = 100s$...	95
5.17 The studied area, the Chao Phraya river at Chai Nat to Sing Buri provinces, Thailand	96
5.18 The results on October 17, 2011 for the case of initially dry on the whole domain. (a) The real data from satellite image on October 17, 2011. (b) The simulation result on October 17, 2011. Initially assumed dry for the whole domain. (c) The difference (pink-shed area) between the real data and the simulation result on October 17, 2011. The comparison is only made on the lower part of the river (inside yellow box)	98
5.19 The results on October 17, 2011 for the case of initially dry on the whole domain and specify water flow on the top boundary. (a) The real data from satellite image on October 17. (b) The simulation result on October 17, initially assumed dry for the whole domain, and specify source of water along the top boundary. (c) The difference (pink-shed area) between	

FIGURE	page
real data from the satellite image and the simulation result	99
5.20 The initial water distribution on October 15, 2011. (a) The real data from satellite image on October 15, 2011. (b) The assumed initial water distribution on October 15, 2011. (c) The difference (pink) between real data from satellite image and the assumed initial water distribution	100
5.21 The results on October 17, 2011. (a) The real data from satellite image on October 17, 2011. (b) The simulation result on October 17, 2011. (c) The difference (pink) between real data from satellite image and the simulation result	101

CHAPTER I

INTRODUCTION

Shallow water equations (SWE) are considered as system of hyperbolic conservation equations which can be used to model many real flow problems such as dam break flows, tsunami waves, open channel flows, flood simulations, etc, where details are given in Chapter II.

There are numerous numerical methods for solving SWE, such as, finite difference methods (FDM) [14], finite element methods (FEM) [43, 49], the finite volume methods (FVM) [23, 25, 29, 31], and the discontinuous Galerkin methods (DG) [15, 37]. The FDM and the FEM can be used to solve these equations but the schemes require to use very large number of nodes in order to obtain high accuracy, especially, for discontinuous solutions, which usually take massive computational time. In addition, these methods usually do not preserve conservation property. Thus, in this work, we use numerical schemes that satisfy the conservation property and are more efficient to deal with discontinuous solution, the DG method and the FVM. The DG method has several advantages, namely, it can be used to handle complex geometries, and in the same time, adaptive strategies are easily applied. The accuracy of numerical solutions can be improved by increasing the polynomial degree of approximating polynomial. The FVM is a special case of the DG method that the approximate solution is averaged in any cell.

By the concept of DG method and FVM, numerical solutions need not to be continuous at cell interfaces, where an efficient flux approximation is required, known as a numerical flux. Generally, there are several types of approximations. The Harten-Lax-van Leer (HLL) flux [37, 40, 41], proposed by Harten, Lax and van Leer, is the one extensively used for the SWE. The modified version of this numerical flux for two-dimensional problems is Harten-Lax-van Leer contact (HLLC) [2]. To obtain more accurate approximations, the weighted average flux (WAF)

has been introduced, see [2, 6, 29, 38, 39, 41, 42].

Hyperbolic conservation equations have steady state solutions in which the flux gradient is required to be balanced with the bottom slope source term. The numerical schemes without balancing these quantities usually exhibit spurious oscillations in the numerical solutions. A numerical scheme that is able to balance these quantities at the steady state is considered to be a well-balanced scheme. The property of a well-balanced scheme was first introduced by Bermudez and Vazquez [5], where the solution from the numerical scheme is exact when applied to the still water stationary solution. Many well-balanced schemes for the SWE have been developed in literature, see [2, 3, 11, 17, 18, 31, 47].

In this dissertation, a well-balanced scheme with total variation diminishing Runge-Kutta discontinuous Galerkin (TVD-RK-DG) method for solving one-dimensional SWE is developed. From previous literature, the WAF has been successfully applied to solve various kinds of problems, especially, in the FVM [2, 6, 11, 29, 38, 39]. However, it is rarely applied in the DG method. Thus, we develop the TVD-RK-DG using the WAF approximation and show that the presented scheme is consistent with the WAF approximation. Various kinds of flows have been simulated to check the accuracy of the modified scheme, where detail is described in Chapter III.

The previous developed scheme assume that every cross-sectional area is equal in the entire domain. If we consider the one-dimensional flow in realistic problem, such as flows in a natural river, where the cross-sectional areas are not equal in the entire domain, we should use SWE in the other form for more realistic results. Thus, we consider the one-dimensional SWE for arbitrary cross-sectional areas instead of the previous equations. In order to reduce complexity of calculation in DG method, the finite volume method is applied. A difficult part of the approximation is even occur when the numerical scheme deal with the dry area. Thus, we also improve the efficiency and stability of the numerical scheme to deal with the wet/dry problem by applied the reconstruction and bottom modification techniques. Various numerical experiments have been performed to check the efficiency and accuracy of the developed numerical scheme. The detail of this work

is presented in Chapter IV.

In addition, in order to consider the flow in two-dimension when applying the SWE to real world applications and to reduce complexity of calculation in DG method for higher dimensional problem, a well-balanced FVM for solving two-dimensional SWE with WAF approximation is developed to simulate real world problems such as dam break or flood, especially, the great flood in Thailand, 2011. A wet/dry cell tracking technique is also presented to reduce computational time. The accuracy of the developed scheme is investigated by applying to some well-studied cases. For practical purposes, it is also applied to simulate the flooding of the Chao Phraya river from Chai Nat to Sing Buri provinces in Thailand during October 13-17, 2011. The detail of this work is given in Chapter V, and the conclusion is given in Chapter VI.

CHAPTER II

SHALLOW WATER EQUATIONS

The shallow water equations (SWE) are considered as a system of hyperbolic partial differential equations which simplified from the Navier–Stokes equations, in the case that the horizontal length scale is much greater than the vertical length scale. These equations can be used to model many real flow problems such as dam break flows, tsunami waves, open channel flows, flood simulations, etc.

2.1 The one-dimensional SWE

For flow in one-dimension in the x -direction, we consider the control volume with uniform cross-sectional area from x to $x + \Delta x$ as shown in Figure 2.1,

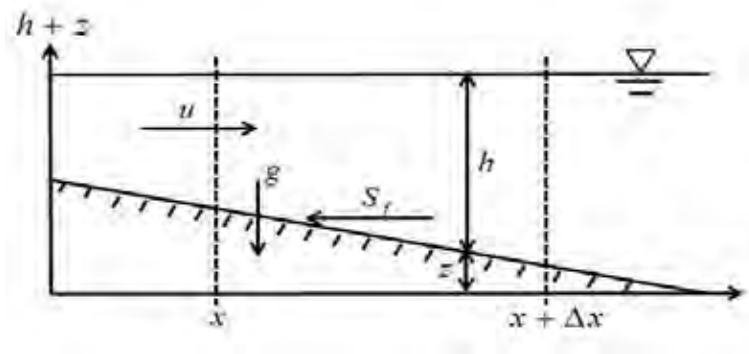


Figure 2.1: One-dimensional control volume.

where h is the water depth, u is the flow velocity in the x -direction, g is the acceleration due to gravity, z is the bottom elevation, and S_f is the friction term.

We will derive SWE in one-dimension by considering the net flow rate in this control volume using principles of conservation of mass and momentum with the assumptions that the fluid is assumed to be incompressible and inviscid, and the

pressure distribution is assumed to be hydrostatic.

Conservation of mass

The conservation of mass states that

$$\boxed{\begin{array}{c} \text{The rate of mass} \\ \text{increase within the} \\ \text{control volume} \end{array}} = \boxed{\begin{array}{c} \text{Mass flux entering} \\ \text{the control volume} \end{array}} - \boxed{\begin{array}{c} \text{Mass flux leaving} \\ \text{the control volume} \end{array}}$$

First, we consider the mass flux entering the control volume at the left boundary of control volume (x, t) , which is

$$\rho hu, \tag{2.1}$$

where ρ is the density of the fluid, $h(x, t)$ and $u(x, t)$ are the fluid depth and flow velocity in the x -direction, respectively.

Next, the mass flux leaving the control volume at the right boundary of control volume $(x + \Delta x, t)$ is

$$\rho hu + \Delta x \frac{\partial}{\partial x} (\rho hu). \tag{2.2}$$

Thus, the net rate of mass flux entering the control volume is

$$\rho hu - \left[\rho hu + \Delta x \frac{\partial}{\partial x} (\rho hu) \right] = -\Delta x \frac{\partial}{\partial x} (\rho hu). \tag{2.3}$$

The rate of mass increase within the control volume is

$$\Delta x \frac{\partial}{\partial t} (\rho h). \tag{2.4}$$

Hence, from (2.3) and (2.4) with the law of conservation of mass, we have

$$\Delta x \frac{\partial}{\partial t} (\rho h) = -\Delta x \frac{\partial}{\partial x} (\rho hu). \tag{2.5}$$

Since, Δx is a constant and the assumption of SWE states that the fluid is incompressible, thus, the density of fluid ρ is a constant. Then, we obtain

$$\frac{\partial h}{\partial t} = -\frac{\partial}{\partial x}(hu) \quad (2.6)$$

or

$$\frac{\partial h}{\partial t} + \frac{\partial}{\partial x}(hu) = 0. \quad (2.7)$$

Equation (2.7) is the conservation of mass for the one-dimensional shallow water equations.

Conservation of momentum

The principle of conservation of momentum states that

The rate of change of momentum in the control volume	=	The net rate of momentum flux entering the control volume	+	Sum of force acting on the control volume
--	---	---	---	---

First, we consider the rate of change of the momentum in the control volume, which is

$$\Delta x \frac{\partial}{\partial t} (\rho u h). \quad (2.8)$$

Next, the rate of momentum entering the control volume at the left boundary of control volume (x, t) is the product of the mass flux and the velocity

$$\rho u^2 h, \quad (2.9)$$

and the momentum leaving the control volume at the right boundary of control volume $(x + \Delta x, t)$ is

$$\rho u^2 h + \Delta x \frac{\partial}{\partial x} (\rho u^2 h). \quad (2.10)$$

Thus, the net rate of the momentum entering the control volume is

$$\rho u^2 h - \left[\rho u^2 h + \Delta x \frac{\partial}{\partial x} (\rho u^2 h) \right] = -\Delta x \frac{\partial}{\partial x} (\rho u^2 h). \quad (2.11)$$

In addition, there are three forces acting on the control volume, which are the gravity force, the pressure force, and the frictional force described as following

(1) **The gravity force** F_g is the weight of the fluid within the control volume acting in the x -direction,

$$F_g = -\rho g h \Delta x \frac{\partial z}{\partial x}, \quad (2.12)$$

where g is a gravity and $\frac{\partial z}{\partial x}$ is the bottom slope.

(2) **The pressure force** F_p is assumed to be the hydrostatic pressure on the vertical section of control volume and water depth h at the boundary (x, t) , that is

$$F_p|_x = \int_0^h \rho g (h - y) dy = \frac{1}{2} \rho g h^2 \quad (2.13)$$

and the pressure force at the boundary $(x + \Delta x, t)$ is

$$F_p|_{x+\Delta x} = \frac{1}{2} \rho g h^2 + \Delta x \frac{\partial}{\partial x} \left(\frac{1}{2} \rho g h^2 \right). \quad (2.14)$$

Thus, net of pressure force on two vertical sides is

$$\frac{1}{2} \rho g h^2 - \left[\frac{1}{2} \rho g h^2 + \Delta x \frac{\partial}{\partial x} \left(\frac{1}{2} \rho g h^2 \right) \right] = -\frac{\Delta x}{2} \frac{\partial}{\partial x} (\rho g h^2). \quad (2.15)$$

(3) **The frictional force** F_f acting on the bottom assumed to be

$$F_f = \rho g h \Delta x S_f, \quad (2.16)$$

where S_f is the friction term define by $S_f = -\frac{n^2 u |u|}{h^{4/3}}$ and n denoting the Manning's roughness coefficient.

From the conservation of momentum, combining (2.8), (2.11), (2.12), (2.15), and (2.16), we obtain

$$\Delta x \frac{\partial}{\partial t} (\rho u h) = -\Delta x \frac{\partial}{\partial x} (\rho u^2 h) + gh\rho\Delta x \left(-\frac{\partial z}{\partial x} + S_f \right) - \frac{g}{2}\Delta x \frac{\partial (\rho h^2)}{\partial x}. \quad (2.17)$$

Since ρ and Δx are non-zero constants,

$$\frac{\partial}{\partial t} (uh) = -\frac{\partial}{\partial x} (u^2h) + gh \left(-\frac{\partial z}{\partial x} + S_f \right) - \frac{g}{2} \frac{\partial h^2}{\partial x}. \quad (2.18)$$

It can be rewritten as

$$\frac{\partial}{\partial t} (uh) + \frac{\partial}{\partial x} \left(u^2h + \frac{gh^2}{2} \right) = -gh \frac{\partial z}{\partial x} + ghS_f. \quad (2.19)$$

If quantity uh is expressed by the discharge Q , then (2.7) and (2.19) can be rewritten as

$$h_t + Q_x = 0, \quad (2.20)$$

$$Q_t + \left(\frac{Q^2}{h} + \frac{gh^2}{2} \right)_x = -ghz_x + ghS_f, \quad (2.21)$$

known as the SWE.

The SWE can be expressed in the one-dimension hyperbolic conservation form as

$$U_t + F(U)_x = S(U), \quad (2.22)$$

where

$$U = \begin{pmatrix} h \\ Q \end{pmatrix}, \quad F(U) = \begin{pmatrix} Q \\ \frac{Q^2}{h} + \frac{gh^2}{2} \end{pmatrix}, \quad \text{and} \quad S(U) = \begin{pmatrix} 0 \\ -ghz_x + ghS_f \end{pmatrix}. \quad (2.23)$$

The vectors U , F , and S represent the vector of primitive variables, the flux function, and the source term, respectively.

2.2 The one-dimensional SWE in arbitrary cross-sectional area

In the previous section, SWE in (2.20)-(2.21) are obtained under the assumption that the cross-sectional area is uniform. In order to obtain SWE for more realistic case such as flows in a natural river, where the cross-sectional area is not uniform in the entire domain. We have to consider the one-dimensional SWE in arbitrary cross-sectional area. The resulting equations are called the Saint Venant equations. These equations are also derived from the conservation of mass and the conservation of momentum, but the cross section is arbitrary as shown in Figures 2.2 and 2.3,

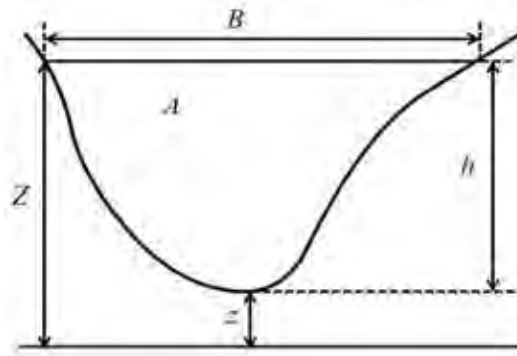


Figure 2.2: Cross-section of channel.

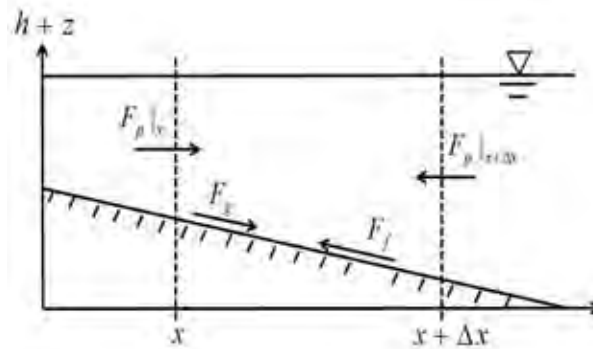


Figure 2.3: One-dimensional control volume for arbitrary cross-sectional area in channel.

where A is the wetted cross-sectional area, $Z = h + z$ is the water surface level, h is the water height, z is the bottom function, B is the width of the cross-section at the water surface, F_p is the pressure force, F_g is the gravity force, and F_f is the friction force.

Derivation of the one-dimensional SWE in arbitrary cross-sectional area

Conservation of mass

The mass flux entering the control volume for an arbitrary cross-sectional area at the left boundary (x, t) of control volume x to $x + \Delta x$ showing in Figure 2.3 is

$$\rho Au, \quad (2.24)$$

where ρ is the density of fluid, $A(x, t)$ and $u(x, t)$ are the wetted cross-sectional area and flow velocity in the x -direction, respectively.

Next, the mass flux leaving the control volume at the right boundary $(x + \Delta x, t)$ is

$$\rho Au + \Delta x \frac{\partial}{\partial x} (\rho Au). \quad (2.25)$$

Thus, the net rate of mass flux entering the control volume is

$$\rho Au - \left[\rho Au + \Delta x \frac{\partial}{\partial x} (\rho Au) \right] = -\Delta x \frac{\partial}{\partial x} (\rho Au). \quad (2.26)$$

The rate of mass increases within the control volume is

$$\Delta x \frac{\partial}{\partial t} (\rho A). \quad (2.27)$$

Hence, from (2.26) and (2.27) with the conservation of mass, we have

$$\Delta x \frac{\partial}{\partial t} (\rho A) = -\Delta x \frac{\partial}{\partial x} (\rho Au). \quad (2.28)$$

Since Δx is non-zero constant and the assumption of SWE states that the fluid is incompressible, thus, ρ is a constant, then we obtain

$$\frac{\partial A}{\partial t} = -\frac{\partial}{\partial x}(Au) \quad (2.29)$$

or

$$\frac{\partial A}{\partial t} + \frac{\partial}{\partial x}(Au) = 0. \quad (2.30)$$

Equation (2.30) is the conservation of mass for the one-dimensional shallow water equations for arbitrary cross-sectional area.

Conservation of momentum

First, we consider the rate of change of the momentum in the control volume, which is

$$\Delta x \frac{\partial}{\partial t}(\rho u A). \quad (2.31)$$

Next, the rate of momentum entering the control volume at the left boundary (x, t) is the product of mass flux and velocity

$$\rho u^2 A \quad (2.32)$$

and the momentum leaving the control volume at the right boundary $(x + \Delta x, t)$ is

$$\rho u^2 A + \Delta x \frac{\partial}{\partial x}(\rho u^2 A). \quad (2.33)$$

Thus, the net rate of the momentum enters in the control volume is

$$\rho u^2 A - \left[\rho u^2 A + \Delta x \frac{\partial}{\partial x}(\rho u^2 A) \right] = -\Delta x \frac{\partial}{\partial x}(\rho u^2 A). \quad (2.34)$$

In the case of arbitrary cross-sectional area, there are four forces acting on the control volume, which are the hydrostatic pressure force, the pressure force due to a change in width, the gravity force, and the frictional force described as follows:

(1) **The hydrostatic pressure force** F_p that acts at the boundary (x, t) is

$$F_p|_x = g\rho I_1, \quad (2.35)$$

where

$$I_1 = \int_0^h (h(x) - \eta) \mu(x, \eta) d\eta, \quad (2.36)$$

g is a gravity, η is a depth integration variable, and $\mu(x, \eta)$ is the width of the cross-section at η such that $\mu(x, \eta) = B(x)$ at the water surface level ($\eta = h$).

The pressure force at the boundary $(x + \Delta x, t)$ is

$$F_p|_{x+\Delta x} = g\rho I_1 + g\rho\Delta x \frac{\partial I_1}{\partial x}. \quad (2.37)$$

Thus, the net of pressure force on two vertical sides in the x -direction is

$$F_p|_x - F_p|_{x+\Delta x} = g\rho I_1 - g\rho I_1 - g\rho\Delta x \frac{\partial I_1}{\partial x} = -g\rho\Delta x \frac{\partial I_1}{\partial x}. \quad (2.38)$$

(2) **The pressure force due to a change in width** F_w for a given cross-section is expressed by

$$F_w = g\rho\Delta x I_2, \quad (2.39)$$

where

$$I_2 = \int_0^h (h(x) - \eta) \frac{\partial \mu(x, \eta)}{\partial x} d\eta. \quad (2.40)$$

(3) **The gravity force** F_g the weight of fluid within the control volume acting in the x -direction,

$$F_g = -\rho g A \Delta x \frac{\partial z}{\partial x}, \quad (2.41)$$

where $\frac{\partial z}{\partial x}$ is the bottom slope.

(4) **The frictional force** F_f acting on the bottom and the sides of the channel is

$$F_f = \rho g A \Delta x S_f, \quad (2.42)$$

where S_f is the friction term expressed by

$$S_f = -\frac{n^2 Q |Q|}{R^{4/3} A^2},$$

n is a Manning's roughness coefficient, Q is a discharge, $R = A/P$ is the hydraulic radius, and P is the wetted perimeter of the channel.

From the conservation of momentum, combining (2.31), (2.34), (2.38), (2.39), (2.41), and (2.42), we obtain

$$\begin{aligned} \Delta x \frac{\partial}{\partial t} (\rho u A) = & -\Delta x \frac{\partial}{\partial x} (\rho u^2 A) - g \rho \Delta x \frac{\partial I_1}{\partial x} + g \rho \Delta x I_2 \\ & - \rho g A \Delta x \frac{\partial z}{\partial x} + \rho g A \Delta x S_f. \end{aligned} \quad (2.43)$$

Since ρ and Δx are non-zero constants, we have

$$\frac{\partial}{\partial t} (u A) = -\frac{\partial}{\partial x} (u^2 A) - g \frac{\partial I_1}{\partial x} + g I_2 - g A \frac{\partial z}{\partial x} + g A S_f. \quad (2.44)$$

It can be rewritten as

$$\frac{\partial}{\partial t} (u A) + \frac{\partial}{\partial x} (u^2 A + g I_1) = g I_2 - g A \frac{\partial z}{\partial x} + g A S_f. \quad (2.45)$$

Equation (2.45) is the conservation of momentum for the one-dimensional shallow water equations for arbitrary cross-sectional area.

For discharge $Q = Au$, (2.30) and (2.45) can be rewritten as

$$\frac{\partial A}{\partial t} + \frac{\partial Q}{\partial x} = 0, \quad (2.46)$$

$$\frac{\partial Q}{\partial t} + \frac{\partial}{\partial x} \left(\frac{Q^2}{A} + g I_1 \right) = g I_2 + g A \left(-\frac{\partial z}{\partial x} + S_f \right). \quad (2.47)$$

Applying the Leibnitz's rule for $\frac{\partial I_1}{\partial x}$ we obtain

$$\begin{aligned}
\frac{\partial I_1}{\partial x} &= \frac{\partial}{\partial x} \int_0^{h(x)} (h(x) - \eta) \mu(x, \eta) d\eta \\
&= [(h(x) - h(x))\mu(x, h(x))] \frac{dh(x)}{dx} + \int_0^{h(x)} \frac{\partial}{\partial x} (h(x) - \eta) \mu(x, \eta) d\eta \\
&= \int_0^{h(x)} \left[(h(x) - \eta) \frac{\partial \mu(x, \eta)}{\partial x} + \mu(x, \eta) \frac{\partial h(x)}{\partial x} \right] d\eta \\
&= \int_0^{h(x)} (h(x) - \eta) \frac{\partial \mu(x, \eta)}{\partial x} d\eta + \int_0^{h(x)} \mu(x, \eta) \frac{\partial h(x)}{\partial x} d\eta \\
&= I_2 + \frac{\partial h(x)}{\partial x} \int_0^{h(x)} \mu(x, \eta) d\eta \\
&= I_2 + A \frac{\partial h(x)}{\partial x}.
\end{aligned}$$

Thus, the equation (2.47) becomes

$$\frac{\partial Q}{\partial t} + \frac{\partial}{\partial x} \left(\frac{Q^2}{A} \right) = -gA \frac{\partial Z}{\partial x} + gAS_f, \quad (2.48)$$

where $Z = h + z$. The hydrostatic pressure term and the pressure force due to a change in width are combined.

Hence, the SWE in arbitrary cross-sectional area are written by

$$A_t + Q_x = 0, \quad (2.49)$$

$$Q_t + \left(\frac{Q^2}{A} \right)_x = -gAZ_x + gAS_f. \quad (2.50)$$

These equations can be written in hyperbolic conservation form (2.22) with vectors

$$U = \begin{pmatrix} A \\ Q \end{pmatrix}, \quad F(U) = \begin{pmatrix} Q \\ \frac{Q^2}{A} \end{pmatrix}, \quad \text{and} \quad S(U) = \begin{pmatrix} 0 \\ -gAZ_x + gAS_f \end{pmatrix}. \quad (2.51)$$

In the particular case when the channel is rectangular with constant width, (2.49) and (2.50) reduce to (2.20) and (2.21), respectively.

2.3 The two-dimensional SWE

In order to consider the flow in two-dimension, the control volume must be considered in two-dimensions as shown in Figure 2.4. Derivation of the two-dimensional SWE is similar to the one-dimensional SWE, but the flow in the y -direction is also considered. The conservation of mass and the conservation of momentum equations in the x - and the y -directions are written as

$$h_t + (hu)_x + (hv)_y = 0, \quad (2.52)$$

$$(hu)_t + \left(hu^2 + \frac{1}{2}gh^2 \right)_x + (huv)_y = -ghz_x + S_{fx}, \quad (2.53)$$

$$(hv)_t + (huv)_x + \left(hv^2 + \frac{1}{2}gh^2 \right)_y = -ghz_y + S_{fy}, \quad (2.54)$$

where u and v are the flow velocities in the x - and y -directions, respectively, $S_{fx} = -Cu\sqrt{u^2 + v^2}$ and $S_{fy} = -Cv\sqrt{u^2 + v^2}$ are the friction terms in the x - and y -directions, respectively, with $C = gn^2/h^{1/3}$ and n is a Manning's roughness coefficient. These equations can be written in two-dimensional hyperbolic conservation form as

$$U_t + F(U)_x + G(U)_y = S(U), \quad (2.55)$$

where F and G represent the flux functions in the x - and y -directions, respectively. Thus, (2.52)-(2.54) can be written in the form of (2.55) with

$$U = \begin{pmatrix} h \\ hu \\ hv \end{pmatrix}, \quad F(U) = \begin{pmatrix} hu \\ hu^2 + \frac{1}{2}gh^2 \\ huv \end{pmatrix}, \quad G(U) = \begin{pmatrix} hv \\ huv \\ hv^2 + \frac{1}{2}gh^2 \end{pmatrix} \quad (2.56)$$

and

$$S(U) = \begin{pmatrix} 0 \\ -ghz_x + S_{fx} \\ -ghz_y + S_{fy} \end{pmatrix}. \quad (2.57)$$

Equation (2.52)-(2.54) are called the two-dimensional shallow water equations. We will develop a finite volume method to solve these equations in Chapter V. The applications of simulating these equations to the great flood in Thailand, 2011 are shown in the same Chapter.

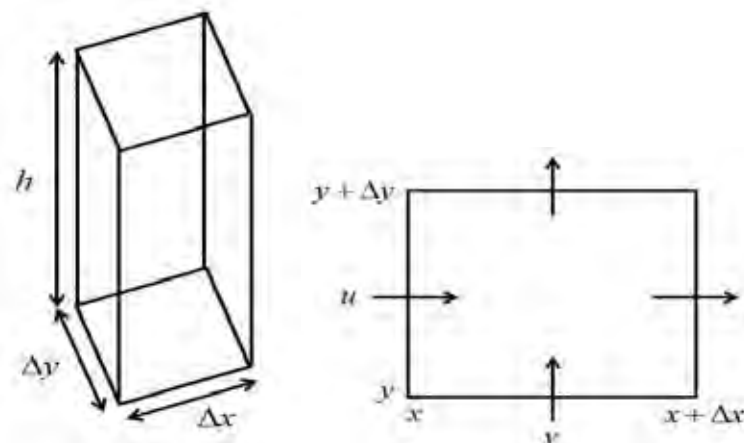


Figure 2.4: Control volume for two-dimensional problem, side view (left) and top view (right).

CHAPTER III

WELL-BALANCED DISCONTINUOUS GALERKIN METHOD WITH WEIGHTED AVERAGE FLUX FOR ONE-DIMENSIONAL SHALLOW WATER EQUATIONS

A well-balanced scheme with total variation diminishing Runge-Kutta discontinuous Galerkin (TVD-RK DG) method with weighted average flux (WAF) for solving SWE is presented in this Chapter. Generally, the flux function at cell interface in the TVD-RK DG scheme for SWE is approximated by using the Harten-Lax-van Leer (HLL) method. Here, we apply WAF, a higher order approximation, instead of using the HLL in the TVD-RK DG method. Moreover, the consistency property is shown and the modified well-balanced technique for flux gradient and source terms under the WAF approximations is developed.

3.1 Discontinuous Galerkin method (DG) for one-dimensional shallow water equations

Consider the one-dimensional SWE

$$U_t + F(U)_x = S(U), \quad (3.1)$$

where

$$U = \begin{pmatrix} h \\ Q \end{pmatrix}, F(U) = \begin{pmatrix} Q \\ \frac{Q^2}{h} + \frac{gh^2}{2} \end{pmatrix} \text{ and } S(U) = \begin{pmatrix} 0 \\ -ghz_x + ghS_f \end{pmatrix} \quad (3.2)$$

in which h is the water depth, $Q = uh$ is the discharge, u is the flow velocity in the x -direction, g is the acceleration due to gravity, z is the bottom elevation, and S_f is the friction term define by $S_f = -(n^2 u |u|)/h^{4/3}$ with n denoting the Manning's roughness coefficient.

The DG method for one-dimensional conservation equation is started by dividing the computational domain $(0, L)$ into K cells. We denote the i -th cell by $I_i = [x_{i-\frac{1}{2}}, x_{i+\frac{1}{2}}]$, for $i = 1, 2, 3, \dots, K$, with uniform cell size $\Delta x = x_{i+\frac{1}{2}} - x_{i-\frac{1}{2}}$. The cell center is $x_i = (x_{i+\frac{1}{2}} + x_{i-\frac{1}{2}})/2$, where $x_{i-\frac{1}{2}}$ and $x_{i+\frac{1}{2}}$ are the left and the right boundaries, respectively. Approximate solution is denoted by $U_h = (h_h, Q_h)^T$.

Multiplying (3.1) by a test function $v_h(x) \in P^N(I_i)$, where $P^N(I_i)$ is the polynomial space of degree N on the interval I_i , replacing U by U_h and taking the integration by parts over I_i , we obtain the weak form of the numerical scheme,

$$\begin{aligned} \int_{I_i} \frac{\partial(U_h)}{\partial t} v_h(x) dx - \int_{I_i} F(U_h) v_h'(x) dx + \widehat{F}_{i+\frac{1}{2}} v_h(x_{i+\frac{1}{2}}^-) - \widehat{F}_{i-\frac{1}{2}} v_h(x_{i-\frac{1}{2}}^+) \\ = \int_{I_i} S(U_h) v_h(x) dx, \end{aligned} \quad (3.3)$$

where the flux function F at the cell interfaces is approximated by $\widehat{F}_{i\pm\frac{1}{2}}$ as a function of U_h^+ and U_h^- at $x_{i\pm\frac{1}{2}}$, defined by

$$\widehat{F}_{i\pm\frac{1}{2}} = \widehat{F}\left((U_h)_{i\pm\frac{1}{2}}^-, (U_h)_{i\pm\frac{1}{2}}^+\right). \quad (3.4)$$

Here, $(U_h)_{i\pm\frac{1}{2}}^-$ and $(U_h)_{i\pm\frac{1}{2}}^+$ denote the approximate solutions at the left and the right of cell boundaries, respectively. If we apply the Legendre polynomials as local basis functions, the approximate solution U_h can be written by

$$U_h(x, t) = \sum_{m=0}^N U_i^m(t) \varphi_m(x), \quad (3.5)$$

where $U_i^m(t)$ is called the temporal coefficient and the basis function $\varphi_m(x)$ is the Legendre polynomial $P_m([-1, 1])$.

The test function $v_h(x)$ is typically chosen to be the basis function, $v_h(x) \in \{\varphi_l(x)\}_{l=0}^N$. After applying the Legendre's properties, the equation (3.3) is simplified to

$$\begin{aligned} \frac{dU_i^l(t)}{dt} = & \frac{2l+1}{\Delta x} \int_{I_i} F(U_h) \varphi'_l(x) dx + \frac{2l+1}{\Delta x} \left\{ (-1)^l \widehat{F}_{i-\frac{1}{2}} - \widehat{F}_{i+\frac{1}{2}} \right\} \\ & + \int_{I_i} S(U_h) v_h(x) dx, \end{aligned} \quad (3.6)$$

for $i = 1, 2, 3, \dots, K$, and $l = 0, 1, 2, \dots, N$.

The conservation form (3.1) is reduced to a system of ordinary differential equations in time for unknown U_i^l . The time derivative term in (3.6) can be approximated by applying the high-order total variation diminishing Runge-Kutta (TVD-RK) method [7, 15, 36].

3.1.1 Numerical flux

In this dissertation, we use two types of numerical flux functions, the Harten-Lax-van Leer flux and the weighted average flux, to approximate flux at interfaces, $\widehat{F}_{i\pm\frac{1}{2}}$.

Harten-Lax-van Leer flux (HLL)

Harten, Lax and van Leer [14] presented approximate Riemann Solver for the numerical flux which is called HLL flux [35, 37, 40, 41]. The HLL flux, $\widehat{F}_{i+\frac{1}{2}}^{HLL}$, at the interface $x_{i+\frac{1}{2}}$ is defined by

$$\widehat{F}_{i+\frac{1}{2}}^{HLL} \left(U_{i+\frac{1}{2}}^-, U_{i+\frac{1}{2}}^+ \right) = \begin{cases} F \left(U_{i+\frac{1}{2}}^- \right) & \text{if } 0 \leq S_L; \\ F_{i+\frac{1}{2}}^* & \text{if } S_L < 0 < S_R; \\ F \left(U_{i+\frac{1}{2}}^+ \right) & \text{if } 0 \geq S_R, \end{cases} \quad (3.7)$$

where $F_{i+\frac{1}{2}}^*$ is defined by

$$F_{i+\frac{1}{2}}^* = \frac{S_R F \left(U_{i+\frac{1}{2}}^- \right) - S_L F \left(U_{i+\frac{1}{2}}^+ \right) + S_L S_R \left(U_{i+\frac{1}{2}}^+ - U_{i+\frac{1}{2}}^- \right)}{S_R - S_L}. \quad (3.8)$$

The wave speeds S_L and S_R at the cell interface are chosen under the assumption of two-rarefaction waves in the star region,

$$S_L = \min \left(u_{i+\frac{1}{2}}^- - \sqrt{gh_{i+\frac{1}{2}}^-}, u^* - \sqrt{gh^*} \right), \quad (3.9)$$

$$S_R = \min \left(u_{i+\frac{1}{2}}^+ + \sqrt{gh_{i+\frac{1}{2}}^+}, u^* + \sqrt{gh^*} \right), \quad (3.10)$$

with

$$\sqrt{gh^*} = \frac{1}{2} \left(\sqrt{gh_{i+\frac{1}{2}}^-} + \sqrt{gh_{i+\frac{1}{2}}^+} \right) - \frac{1}{4} \left(u_{i+\frac{1}{2}}^+ - u_{i+\frac{1}{2}}^- \right), \quad (3.11)$$

$$u^* = \frac{1}{2} \left(u_{i+\frac{1}{2}}^- + u_{i+\frac{1}{2}}^+ \right) + \sqrt{gh_{i+\frac{1}{2}}^-} - \sqrt{gh_{i+\frac{1}{2}}^+}. \quad (3.12)$$

The expressions for the wave speeds are obtained by assuming the wet bed condition, i.e., $h_{i+\frac{1}{2}}^\pm > 0$. For the dry bed on the right side of the cell interface, i.e., $h_{i+\frac{1}{2}}^+ = 0$ and $h_{i+\frac{1}{2}}^- > 0$, the wave speeds are approximated by

$$S_L = u_{i+\frac{1}{2}}^- - \sqrt{gh_{i+\frac{1}{2}}^-}, \quad S_R = u_{i+\frac{1}{2}}^- + 2\sqrt{gh_{i+\frac{1}{2}}^-}, \quad (3.13)$$

and for the dry bed on the left side of the cell interface, i.e., $h_{i+\frac{1}{2}}^- = 0$ and $h_{i+\frac{1}{2}}^+ > 0$,

$$S_L = u_{i+\frac{1}{2}}^+ - 2\sqrt{gh_{i+\frac{1}{2}}^+}, \quad S_R = u_{i+\frac{1}{2}}^+ + \sqrt{gh_{i+\frac{1}{2}}^+}. \quad (3.14)$$

The diagram for the HLL flux corresponding to the Riemann problem is shown in Figure 3.1.

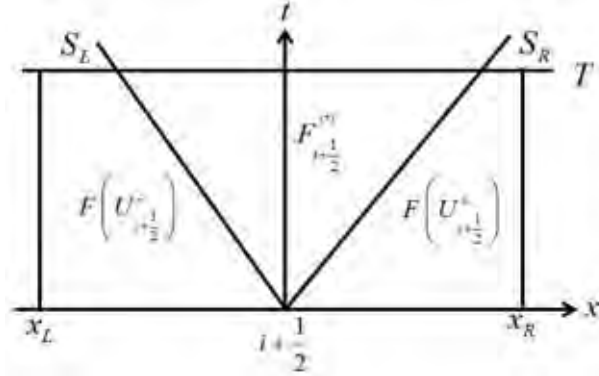


Figure 3.1: The diagram for HLL flux corresponding to the Riemann problem at interface $i+1/2$.

Weighted average flux (WAF)

The WAF was first introduced by Toro, see [40, 41]. The WAF approximation is second-order accurate in both space and time in statistical sense, [40].

The weighted average flux, $\widehat{F}_{i+1/2}^{WAF}$, at the interface $x_{i+1/2}$ is defined by the integral average of a flux function $F(U)$ at the half-time step,

$$\widehat{F}_{i+1/2}^{WAF} = \frac{1}{\Delta x} \int_{-\frac{\Delta x}{2}}^{\frac{\Delta x}{2}} F \left(U_{i+1/2} \left(x, \frac{\Delta t}{2} \right) \right) dx. \quad (3.15)$$

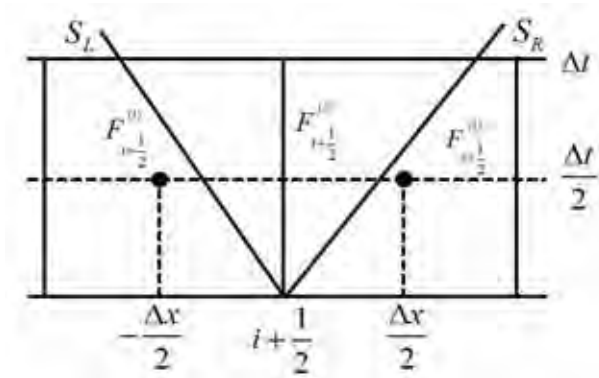


Figure 3.2: The diagram for WAF corresponding to the Riemann problem at interface $i+1/2$.

It can be written in the summation of wave structure form as,

$$\widehat{F}_{i+\frac{1}{2}}^{WAF} = \sum_{k=1}^{N_c+1} \omega_k F_{i+\frac{1}{2}}^{(k)}, \quad (3.16)$$

where N_c is the number of wave solutions in the Riemann problem and $F_{i+\frac{1}{2}}^{(k)}$ is the k^{th} flux of the Riemann problem. For one-dimensional shallow water flows, one has $N_c = 2$, with $F_{i+\frac{1}{2}}^{(1)} = F(U_{i+\frac{1}{2}}^-)$, $F_{i+\frac{1}{2}}^{(3)} = F(U_{i+\frac{1}{2}}^+)$, and the flux component $F_{i+\frac{1}{2}}^{(2)}$ is obtained from the HLL approach [40]. The weighted ω_k are defined by $\omega_k = \frac{1}{2}(c_k - c_{k-1})$, where $c_k = S_k \Delta t / \Delta x$ is the Courant number of wave k , $c_0 = -1$, $c_{N_c+1} = 1$, and S_k is the speed of wave k with $S_1 = S_L$ and $S_2 = S_R$ which defined in the same manner as the HLL flux. The diagram for WAF corresponding to the Riemann problem is shown in Figure 3.2.

To avoid spurious oscillations near a shock front, the WAF method is modified by enforcing a total variation diminishing (TVD) scheme [6, 11, 29, 40, 41]. The TVD-WAF version becomes

$$\widehat{F}_{i+\frac{1}{2}}^{WAF-TVD} = \frac{1}{2} \left(F(U_{i+\frac{1}{2}}^-) + F(U_{i+\frac{1}{2}}^+) \right) - \frac{1}{2} \sum_{k=1}^{N_c} \text{sgn}(c_k) \phi_{i+\frac{1}{2}}^{(k)} \Delta F_{i+\frac{1}{2}}^{(k)}, \quad (3.17)$$

where

$$\Delta F_{i+\frac{1}{2}}^{(k)} = F_{i+\frac{1}{2}}^{(k+1)} - F_{i+\frac{1}{2}}^{(k)}. \quad (3.18)$$

Here, $\phi_{i+\frac{1}{2}}^{(k)}$ is a WAF limiter function. There are various choices for $\phi_{i+\frac{1}{2}}^{(k)}$, see more details in [6, 11, 29, 40, 41]. In this work, we employ the minmod slope limiter

$$\phi_{i+\frac{1}{2}}^{(k)}(r^{(k)}) = \begin{cases} 1, & r^{(k)} \leq 0, \\ 1 - (1 - |c_k|) r^{(k)}, & 0 < r^{(k)} < 1, \\ |c_k|, & r^{(k)} \geq 1, \end{cases} \quad (3.19)$$

where $r^{(k)}$ is defined by

$$r^{(k)} = \begin{cases} \frac{\Delta h_{i-\frac{1}{2}}^{(k)}}{\Delta h_{i+\frac{1}{2}}^{(k)}} = \frac{h_{i-\frac{1}{2}}^{(k),+} - h_{i-\frac{1}{2}}^{(k),-}}{h_{i+\frac{1}{2}}^{(k),+} - h_{i+\frac{1}{2}}^{(k),-}}, & \text{if } c_k \geq 0, \\ \frac{\Delta h_{i+\frac{3}{2}}^{(k)}}{\Delta h_{i+\frac{1}{2}}^{(k)}} = \frac{h_{i+\frac{3}{2}}^{(k),+} - h_{i+\frac{3}{2}}^{(k),-}}{h_{i+\frac{1}{2}}^{(k),+} - h_{i+\frac{1}{2}}^{(k),-}}, & \text{if } c_k < 0 \end{cases} \quad (3.20)$$

with $\Delta h_{i-\frac{1}{2}}^{(k)}$, $\Delta h_{i+\frac{1}{2}}^{(k)}$ and $\Delta h_{i+\frac{3}{2}}^{(k)}$ are the jumps of h across the wave k in the solutions $U_{i-\frac{1}{2}}$, $U_{i+\frac{1}{2}}$ and $U_{i+\frac{3}{2}}$ of the Riemann problem, respectively.

Actually, WAF has a consistency property which can be shown by the following Lemma.

Lemma 1 TVD-WAF is a consistent numerical flux for smooth flow problem.

Proof Consider a smooth solution at interface $i+1/2$, it is sufficient to show that TVD-WAF is a consistent numerical flux if $\widehat{F}_{i+\frac{1}{2}}^{\text{TVD-WAF}}(U_{i+\frac{1}{2}}^-, U_{i+\frac{1}{2}}^+) = F(U_{i+\frac{1}{2}})$.

The TVD-WAF is defined by

$$\begin{aligned} \widehat{F}_{i+\frac{1}{2}}^{\text{TVD-WAF}}(U_{i+\frac{1}{2}}^-, U_{i+\frac{1}{2}}^+) &= \frac{1}{2} \left(F(U_{i+\frac{1}{2}}^-) + F(U_{i+\frac{1}{2}}^+) \right) \\ &\quad - \frac{1}{2} \sum_{k=1}^2 \text{sgn}(c_k) \phi_{i+\frac{1}{2}}^k \Delta F_{i+\frac{1}{2}}^{(k)}, \end{aligned} \quad (3.21)$$

for smooth flow problem, $U_{i+\frac{1}{2}}^- = U_{i+\frac{1}{2}}^+ = U_{i+\frac{1}{2}}$, then $F^{(1)} = F(U_{i+\frac{1}{2}}^-) = F(U_{i+\frac{1}{2}})$, $F^{(3)} = F(U_{i+\frac{1}{2}}^+) = F(U_{i+\frac{1}{2}})$, $F^{(2)} = F(U_{i+\frac{1}{2}})$, and $\Delta F_{i+\frac{1}{2}}^{(k)} = 0$. Thus,

$$\begin{aligned} \widehat{F}_{i+\frac{1}{2}}^{\text{TVD-WAF}}(U_{i+\frac{1}{2}}^-, U_{i+\frac{1}{2}}^+) &= \widehat{F}_{i+\frac{1}{2}}(U_{i+\frac{1}{2}}, U_{i+\frac{1}{2}}) \\ &= \frac{1}{2} \left(F(U_{i+\frac{1}{2}}) + F(U_{i+\frac{1}{2}}) \right) - \frac{1}{2} \sum_{k=1}^2 \text{sgn}(c_k) \phi_{i+\frac{1}{2}}^k \Delta F_{i+\frac{1}{2}}^{(k)} \\ &= F(U_{i+\frac{1}{2}}). \end{aligned} \quad (3.22)$$

This shows that the TVD-WAF is consistent for smooth flow. \square

3.1.2 Total Variation Diminishing Runge Kutta (TVD-RK)

After discretizing conservation equations in spatial space by the DG method, we obtain a system of ODEs with respect to the time derivative as in (3.6), which can be approximated by applying the high-order TVD-RK method [7, 15, 36], introduced by Chi-Wang Shu [36].

The system (3.6) can be written in the form

$$\frac{dU_h(t)}{dt} = L_h(U_h, t), \quad (3.23)$$

where $t \in (0, T)$ with initial condition

$$U_h(x, 0) = U_{0h} \quad (3.24)$$

and $L_h(U_h, t)$ represents the right hand side of equation (3.6).

Let $\{t^n\}_{n=0}^M$ be a partition of $[0, T]$ into M intervals with $\Delta t^n = t^{n+1} - t^n$, for $n = 0, \dots, M - 1$. The time marching algorithm can be summarized as follows.

1. Set $U_h^0 = U_{0h}$.
2. For $n = 0, \dots, M - 1$ compute U_h^{n+1} from U_h^n as following steps 2.1-2.3;
 - 2.1 set $d^{(0)} = U_h^n$,
 - 2.2 for $m = 1, \dots, k + 1$ compute the intermediate functions:

$$d^{(m)} = \left\{ \sum_{s=0}^{m-1} (\alpha_{ms} d^{(s)} + \beta_{ms} \Delta t^n L_h(d^{(s)}, t)) \right\},$$

where α_{ms} and β_{ms} are parameters of the TVD-RK.

- 2.3 set $U_h^{n+1} = d^{(k+1)}$.

For example, the TVD-RK of orders 2 and 3 are as follows

TVD-RK order 2

$$d^{(1)} = U_h^n + \Delta t L_h(U_h^n, t^n), \quad (3.25)$$

$$U_h^{n+1} = d^{(2)} = \frac{1}{2} (U_h^n + d^{(1)} + \Delta t L_h (d^{(1)}, t^n + \Delta t)). \quad (3.26)$$

TVD-RK order 3

$$d^{(1)} = U_h^n + \Delta t L_h (U_h^n, t^n), \quad (3.27)$$

$$d^{(2)} = \frac{1}{4} (3U_h^n + d^{(1)} + \Delta t L_h (d^{(1)}, t^n + \Delta t)), \quad (3.28)$$

$$U_h^{n+1} = d^{(3)} = \frac{1}{3} \left(U_h^n + 2d^{(2)} + 2\Delta t L_h \left(d^{(2)}, t^n + \frac{1}{2}\Delta t \right) \right). \quad (3.29)$$

By these setting, the TVD-RK has some useful stability properties, where details are given in [7, 15].

Note that when the polynomial of degree N is applied for DG, the TVD-RK method of order at least $N+1$ is required to obtain the accuracy of order $O(\Delta x^{N+1})$ for smooth flows problem.

3.1.3 Monotonic Upstream-Centered Scheme for Conservation Laws (MUSCL) slope limiter

The TVD-RK DG method can be used to simulate shallow water flows with moving shocks. Unphysically oscillate behaviours are usually produced near the shock fronts. The slope limiter techniques can be applied to remove the oscillations. In this work, we apply the Monotonic Upstream-Centered Scheme for Conservation Laws (MUSCL) limiter [7, 15, 25, 40] in the TVD-RK DG method. This approach limits the present solution slope by comparing with neighbor cells.

In the case of piecewise linear approximation, $U_h|_{I_i} = U_i^0 + U_i^1 x$, the slope limiter function of $U_h|_{I_i}$ is

$$\Lambda\Pi_h^1(U_h|_{I_i}) = \bar{U}_i + (x - x_i) \min\text{mod} \left(U_{x,i}, \frac{\bar{U}_{i+1} - \bar{U}_i}{\Delta x}, \frac{\bar{U}_i - \bar{U}_{i-1}}{\Delta x} \right), \quad (3.30)$$

for $i = 1, \dots, K$.

In (3.30), \bar{U}_i is the mean value in the i -th cell, $U_{x,i} = U_i^1$ and the minmod function is defined by

$$\min\text{mod}(a_1, a_2, \dots, a_n) = \begin{cases} \text{sgn}(a_1) \min_{1 \leq i \leq n} |a_i|, & \text{if } \text{sgn}(a_1) = \dots = \text{sgn}(a_n), \\ 0, & \text{otherwise.} \end{cases}$$

This is the well-known slope limiter of the MUSCL schemes introduced by van Leer [44, 45].

In the case that the approximate solution is a polynomial of degree $N \geq 2$,

$$U_h|_{I_i}(x, t) = \sum_{l=0}^N U_i^l(t) \varphi_l(x).$$

We defined the degree one of U_h denoted by U_h^1 as

$$U_h^1|_{I_i}(x, t) = \sum_{l=0}^1 U_i^l(t) \varphi_l(x).$$

The slope limiter procedure in this case, denoted by $\Lambda\Pi_h^N$, is obtained as follows

(1) Compute $\tilde{U}_{i+\frac{1}{2}}^-$ and $\tilde{U}_{i-\frac{1}{2}}^+$ from

$$\tilde{U}_{i+\frac{1}{2}}^- = \bar{U}_i + \min\text{mod} \left(U_{i+\frac{1}{2}}^- - \bar{U}_i, \bar{U}_i - \bar{U}_{i-1}, \bar{U}_{i+1} - \bar{U}_i \right), \quad (3.31)$$

$$\tilde{U}_{i-\frac{1}{2}}^+ = \bar{U}_i - \min\text{mod} \left(\bar{U}_i - U_{i-\frac{1}{2}}^+, \bar{U}_i - \bar{U}_{i-1}, \bar{U}_{i+1} - \bar{U}_i \right). \quad (3.32)$$

(2) If $\tilde{U}_{i+\frac{1}{2}}^- = U_{i+\frac{1}{2}}^-$ and $\tilde{U}_{i-\frac{1}{2}}^+ = U_{i-\frac{1}{2}}^+$, then set $\Lambda\Pi_h^N(U_h|_{I_i}) = U_h|_{I_i}$.

(3) Otherwise, take $U_h|_{I_i}$ equals to $\Lambda\Pi_h^1(U_h^1|_{I_i})$.

3.2 Consistency of WAF with TVD-RK DG method

The HLL flux is usually used in the TVD-RK DG method. Another choice but higher order is the WAF. This approximation has been extensively applied in the FVM, but it is rarely used in the TVD-RK DG method. Thus, the main objective of this work is to modify the WAF in the TVD-RK DG method. The consistency of the WAF in the TVD-RK DG scheme without source term is described below.

Lemma 2 The TVD-RK DG method is consistent with the WAF for smooth flows problem.

Proof Considering the weak form of DG method for the conservation law

$$\int_{I_i} \left(\frac{\partial}{\partial t} U \right) v(x) dx - \int_{I_i} F(U) v'(x) dx + F \left(U_{i+\frac{1}{2}} \right) v \left(x_{i+\frac{1}{2}}^- \right) - F \left(U_{i-\frac{1}{2}} \right) v \left(x_{i-\frac{1}{2}}^+ \right) = 0. \quad (3.33)$$

Exact solution U is approximated by U_h^* , the test function v is estimated by v_h , and flux function, F , at cell interfaces are approximated in terms of numerical flux, $\widehat{F}_{i\pm\frac{1}{2}}$, the DG method becomes

$$\int_{I_i} \left(\frac{\partial}{\partial t} U_h^* \right) v_h(x) dx - \int_{I_i} F(U_h^*) v_h'(x) dx + \widehat{F}_{i+\frac{1}{2}} \left((U_h^*)_{i+\frac{1}{2}}^-, (U_h^*)_{i+\frac{1}{2}}^+ \right) v_h \left(x_{i+\frac{1}{2}}^- \right) - \widehat{F}_{i-\frac{1}{2}} \left((U_h^*)_{i-\frac{1}{2}}^-, (U_h^*)_{i-\frac{1}{2}}^+ \right) v_h \left(x_{i-\frac{1}{2}}^+ \right) = T, \quad (3.34)$$

where T is a total truncation error of the scheme.

By using Gauss-Lobatto quadrature $N + 1$ points, the integrals terms in (3.34) give the exact value for polynomials degree N . Then, the truncation error, T , is composed of the numerical flux error, the approximate solution in space, and the approximate solution in time which are denoted by T_1 , T_2 , and T_3 , respectively.

Consider interface $i+1/2$, when the solution is smooth, it is continuous at $x_{i+1/2}$, thus, $(U_h^*)_{i+1/2}^+ = (U_h^*)_{i+1/2}^- = (U_h^*)_{i+1/2}$. From Lemma 1, the TVD-WAF is consistent, thus, the numerical flux, $\widehat{F}_{i+1/2}$, becomes an exact flux, $F((U_h^*)_{i+1/2})$. It can be considered similarly for interface $i-1/2$. This makes $T_1 = 0$ for smooth flow problem.

For the TVD-RK DG method, the approximate solution U_h^* in (3.34) is defined by

$$U_h^*(x, t) = \sum_{k=0}^N U_k(t) \varphi_k(x),$$

where $\varphi_k(x)$ is the Legendre polynomial degree k . Since the considering solution is smooth, Theorem 3.1 in [7] gives that the truncation error term T_2 due to approximating polynomial is in the form

$$T_2 := \|U - U_h^*\|_{L^2(0,1)} \leq O\left(\Delta x^{N+\frac{1}{2}}\right), \text{ for } N \geq 0. \quad (3.35)$$

After substituting the approximate solution into the numerical scheme (3.34), we obtain an ODE system

$$\frac{d}{dt} U_h^* = L(U_h^*).$$

The TVD-RK scheme is applied for integrating in time. The order of accuracy for time integration depends on the TVD-RK order, [7, 15, 36], since the TVD-RK order $N+1$ is applied, thus, a truncation error term T_3 is $O(\Delta t^{N+1})$.

Combining all of the truncation error terms, the total truncation error term of the TVD-RK DG with WAF is

$$T = T_1 + T_2 + T_3 \leq O\left(\Delta x^{N+\frac{1}{2}}, \Delta t^{N+1}\right). \quad (3.36)$$

This shows that the total truncation error term approaches zero as $\Delta x \rightarrow 0$ and $\Delta t \rightarrow 0$. Hence, the TVD-RK DG with the WAF method is consistent. \square

Remark If we apply consistent numerical scheme to approximate source terms, the TVD-RK DG with the WAF method is consistent in the case of the scheme with source term.

3.3 Well-balanced TVD-RK DG with WAF scheme

For the SWE with the source term, the steady solutions of (3.1) is obtained by setting

$$hu = \text{constant} \quad \text{and} \quad \frac{1}{2}u^2 + g(h + z) = \text{constant}. \quad (3.37)$$

Since the flux gradient is nonzero, it must be balanced with the bottom gradient. Usually, numerical schemes without balancing these two quantities produce oscillate steady solution, hence, balancing numerical scheme is needed. In this case the scheme is called the well-balanced scheme. As suggested by Bermudez and Vazquez [5], a numerical scheme is said to be well-balanced if it satisfies the exact C-property, i.e., the numerical solution must satisfy still water condition at steady state

$$u = 0 \quad \text{and} \quad h + z = \text{constant}. \quad (3.38)$$

Therefore, one can obtain a well-balanced scheme by designing the method that its steady solutions satisfy (3.38). Note that we consider only the bottom slope in the source terms at steady state because the friction term does not affect still water solutions.

In this section, we develop a well-balanced scheme for the TVD-RK DG based on the WAF method. The main purpose is to present a modified scheme for solving the SWE with source term that also preserves exactly stationary solution when bottom slope exists. Consider the standard TVD-RK DG method

$$\begin{aligned} \int_{I_i} \left(\frac{\partial}{\partial t} U_h \right) v_h(x) dx - \int_{I_i} F(U_h) v'_h(x) dx + \widehat{F}_{i+\frac{1}{2}} v_h(x_{i+\frac{1}{2}}^-) \\ - \widehat{F}_{i-\frac{1}{2}} v_h(x_{i-\frac{1}{2}}^+) = \int_{I_i} G(U_h) v_h(x) dx \end{aligned} \quad (3.39)$$

with initial condition

$$\int_{I_i} U_h(x, 0) v_h(x) dx = \int_{I_i} U_0(x) v_h(x) dx, \quad (3.40)$$

where $\widehat{F}_{i\pm\frac{1}{2}}$ are the WAFs defined in (3.17), and the source term

$$G(U) = \begin{pmatrix} G_1(U, x) \\ G_2(U, x) \end{pmatrix} = \begin{pmatrix} 0 \\ -ghz_x \end{pmatrix}.$$

We derive a well-balanced scheme based on [47] by using the WAF in the TVD-RK DG instead of the Lax-Friedrichs (LF) flux. The main modification is the treatment of the source terms in the WAF method by writing the source terms as a summation

$$G_p(U, x) = \sum_{m=1}^2 s_m(a(U, x)) t'_m(x), \quad p = 1, 2, \quad (3.41)$$

where s_m and t_m are functions to be determined later and prime, ', denote the derivative with respect to x .

If the solution at steady state is stationary, then $a(U, x)$ in (3.41) can be decomposed into $a_1(U, x)$ and $a_2(U, x)$, such that

$$a_1 \equiv h + z = \text{constant} \quad \text{and} \quad a_2 \equiv u = 0.$$

Since G_1 is zero, we consider only G_2 ,

$$G_2(U, x) = -ghz_x = -g(h+z)z_x + \frac{1}{2}g(z^2)_x \quad (3.42)$$

which is the same as having

$$s_1 = s_1(a_1) = -g(h+z), \quad s_2 = \frac{1}{2}g, \quad t_1(x) = z, \quad \text{and} \quad t_2(x) = z^2$$

for $p = 2$ in (3.42). To balance the flux gradient and the source term approximation at steady state, it is required that

$$\frac{d}{dx} \left(F(U(x)) - \sum_{m=1}^2 s_m(a(U, x))t_m(x) \right) = 0 \quad (3.43)$$

or

$$F(U(x)) - \sum_{m=1}^2 s_m(a(U, x))t_m(x) = \alpha, \quad (3.44)$$

where α and $a(U, x)$ are constants.

The integration of source term in (3.39) can be approximated by

$$\begin{aligned} \int_{I_i} G_2(U_h, x) v_h(x) dx &= \int_{I_i} \sum_m s_m(a(U, x)) t'_m(x) v_h(x) dx \\ &= \sum_m \left[\frac{1}{2} \left(s_m \left(a(U_h, x)_{i-\frac{1}{2}}^+ \right) + s_m \left(a(U_h, x)_{i+\frac{1}{2}}^- \right) \right) \right] \\ &\quad \left[\int_{I_i} t'_m(x) v_h(x) dx \right] \\ &\quad + \sum_m \left[\int_{I_i} \left\{ s_m(a(U_h, x)) - \frac{1}{2} \left(s_m \left(a(U_h, x)_{i-\frac{1}{2}}^+ \right) \right. \right. \right. \\ &\quad \left. \left. \left. + s_m \left(a(U_h, x)_{i+\frac{1}{2}}^- \right) \right) \right\} t'_m(x) v_h(x) dx \right] \\ &= \sum_m \left[\frac{1}{2} \left(s_m \left(a(U_h, x)_{i-\frac{1}{2}}^+ \right) + s_m \left(a(U_h, x)_{i+\frac{1}{2}}^- \right) \right) \right] \\ &\quad \left[t_m \left(x_{i+\frac{1}{2}} \right) v_h \left(x_{i+\frac{1}{2}}^- \right) - t_m \left(x_{i-\frac{1}{2}} \right) v_h \left(x_{i-\frac{1}{2}}^+ \right) \right. \\ &\quad \left. - \int_{I_i} t_m(x) v'_h(x) dx \right] \\ &\quad + \sum_m \left[\int_{I_i} \left\{ s_m(a(U_h, x)) - \frac{1}{2} \left(s_m \left(a(U_h, x)_{i-\frac{1}{2}}^+ \right) \right. \right. \right. \\ &\quad \left. \left. \left. + s_m \left(a(U_h, x)_{i+\frac{1}{2}}^- \right) \right) \right\} t'_m(x) v_h(x) dx \right], \quad m = 1, 2. \quad (3.45) \end{aligned}$$

Functions $a(U_h, x)$ and $t_m(x)$ on the RHS of (3.45) can be approximated by $a_h(U_h, x)$ and $(t_m)_h(x)$, where $a_h(U_h, x), (t_m)_h(x) \in P^N(I_i)$. Then, we obtain $(t_1)_h(x) = z_h$ and $(t_2)_h(x) = z_h^2$. Thus,

$$F(U_h(x)) - \sum_m s_m(a(U_h, x)) (t_m)_h(x) = \alpha \quad (3.46)$$

and

$$\begin{aligned} \int_{I_i} G_2(U_h, x) v_h(x) dx &= \sum_m \left[\frac{1}{2} \left(s_m \left(a_h(U_h, x)_{i-\frac{1}{2}}^+ \right) + s_m \left(a_h(U_h, x)_{i+\frac{1}{2}}^- \right) \right) \right] \\ &\quad \left[(\hat{t}_m)_{h, i+\frac{1}{2}} v_h \left(x_{i+\frac{1}{2}}^- \right) - (\hat{t}_m)_{h, i-\frac{1}{2}} v_h \left(x_{i-\frac{1}{2}}^+ \right) \right. \\ &\quad \left. - \int_{I_i} (t_m)_h(x) v_h'(x) dx \right] + \sum_m \left[\int_{I_i} \left\{ s_m \left(a_h(U_h, x) \right) \right. \right. \\ &\quad \left. \left. - \frac{1}{2} \left(s_m \left(a_h(U_h, x)_{i-\frac{1}{2}}^+ \right) + s_m \left(a_h(U_h, x)_{i+\frac{1}{2}}^- \right) \right) \right\} \right. \\ &\quad \left. (t_m)_h'(x) v_h(x) dx \right], \end{aligned} \quad (3.47)$$

where $(\hat{t}_m)_{h, i-\frac{1}{2}}$ and $(\hat{t}_m)_{h, i+\frac{1}{2}}$ are approximations of $t_m \left(x_{i-\frac{1}{2}} \right)$ and $t_m \left(x_{i+\frac{1}{2}} \right)$, respectively. To satisfy the WAF in (3.16), $(\hat{t}_m)_{h, i+\frac{1}{2}}$ is modified as

$$(\hat{t}_m)_{h, i+\frac{1}{2}} = \sum_{k=1}^{N_c+1} \omega_k t_{h, i+\frac{1}{2}}^{(k)}, \quad (3.48)$$

and if the TVD version in (3.17) is applied, then we use

$$(\hat{t}_m)_{h, i+\frac{1}{2}} = \sum_{k=1}^{N_c+1} \text{sgn}(c_k) \phi_{i+\frac{1}{2}}^{(k)} t_{h, i+\frac{1}{2}}^{(k)}. \quad (3.49)$$

Note that ω_k are weights in the WAF approximations and $\phi_{i+\frac{1}{2}}^{(k)}$ is the WAF limiter function, it can be seen that $t_{h, i+\frac{1}{2}}^{(k)}$ is defined similar to $F_{i+1/2}^{(k)}$.

For one-dimensional problem, we have $N_c = 2$, $t_{h, i+\frac{1}{2}}^{(1)} = t_h \left(x_{i+\frac{1}{2}}^- \right)$, $t_{h, i+\frac{1}{2}}^{(3)} = t_h \left(x_{i+\frac{1}{2}}^+ \right)$, and $t_{h, i+\frac{1}{2}}^{(2)}$ in the intermediate region is obtained via the HLL approach,

$$t_{h,i+\frac{1}{2}}^{(2)} = \begin{cases} t_h \left(x_{i+\frac{1}{2}}^- \right), & \text{if } S_L \geq 0, \\ \frac{S_R t_h \left(x_{i+\frac{1}{2}}^- \right) - S_L t_h \left(x_{i+\frac{1}{2}}^+ \right) + S_R S_L \left(t_h \left(x_{i+\frac{1}{2}}^+ \right) - t_h \left(x_{i+\frac{1}{2}}^- \right) \right)}{S_R - S_L}, & \text{if } S_L < 0 < S_R, \\ t_h \left(x_{i+\frac{1}{2}}^+ \right), & \text{if } S_R \leq 0, \end{cases}$$

where S_L and S_R are the wave speed in the Riemann problem.

At steady state, the solution is assumed to be stationary, i.e., $h + z = c$, where c is a constant and $u = 0$. From (3.46), we have

$$\begin{aligned} F(U_h) - \sum_m s_m(a_h(U, x))t_m(x) &= \frac{1}{2}g(h_h)^2 - \left[\frac{1}{2}gz_h^2 - g(h_h + z_h)z_h \right] \\ &= \frac{1}{2}g(h_h + z_h)^2 \\ &= \frac{1}{2}gc^2 = \alpha. \end{aligned}$$

This shows that the choices of $a(U_h, x)$ and t_m are suitable in the TVD-RK DG with the WAF.

The following result shows that the TVD-RK DG with the WAF method preserves the well-balanced property.

Proposition The TVD-RK DG with the WAF scheme preserves exactly stationary solutions at steady state.

Proof To show that the TVD-RK DG with the WAF scheme preserves exactly stationary solutions at steady state, it is sufficient to show that $T = 0$ where T is a total truncation error of the scheme at steady state.

Since $a_h(U_h, x)$ and $a_h(U_h, x)_{i \mp \frac{1}{2}}^\pm$ are equal to the same constant c at each point over cell I_i at steady state, thus,

$$\sum_m \left[\int_{I_i} \left\{ s_m(a_h(U_h, x)) - \frac{1}{2} \left(s_m(a_h(U_h, x)_{i-\frac{1}{2}}^+) + s_m(a_h(U_h, x)_{i+\frac{1}{2}}^-) \right) \right\} (t_m)'_h(x) v_h(x) dx \right] = 0.$$

From (3.34), the total truncation error when considering the source term is

$$\begin{aligned} T &= \int_{I_i} F(U_h(x, t)) v'_h(x) dx - \widehat{F}_{i+\frac{1}{2}}^{WAF} v_h(x_{i+\frac{1}{2}}^-) + \widehat{F}_{i-\frac{1}{2}}^{WAF} v_h(x_{i-\frac{1}{2}}^+) + \sum_m \left[\frac{1}{2} \left(s_m(a_h(U_h, x)_{i-\frac{1}{2}}^+) \right. \right. \\ &\quad \left. \left. + s_m(a_h(U_h, x)_{i+\frac{1}{2}}^-) \right) \right] \left[(\hat{t}_m)_{h, i+\frac{1}{2}} v_h(x_{i+\frac{1}{2}}^-) - (\hat{t}_m)_{h, i-\frac{1}{2}} v_h(x_{i-\frac{1}{2}}^+) \right. \\ &\quad \left. - \int_{I_i} (t_m)_h(x) v'_h(x) dx \right]. \end{aligned}$$

Using $\widehat{F}_{i\pm\frac{1}{2}}^{WAF}$ in (3.16), $(\hat{t}_m)_{h, i\pm\frac{1}{2}}$ in (3.48), and $a_h(U_h, x)_{i\mp\frac{1}{2}}^\pm = c$, we have

$$\begin{aligned} T &= \int_{I_i} \left[F(U_h(x, t)) - \sum_m s_m(c) (t_m)_h(x) \right] v'_h(x) dx - \left[\sum_{k=1}^3 \omega_k F_{i+\frac{1}{2}}^{(k)} - \sum_m s_m(c) \left(\sum_{k=1}^3 \omega_k t_{h, i+\frac{1}{2}}^{(k)} \right) \right] \\ &\quad v_h(x_{i+\frac{1}{2}}^-) + \left[\sum_{k=1}^3 \omega_k F_{i-\frac{1}{2}}^{(k)} - \sum_m s_m(c) \left(\sum_{k=1}^3 \omega_k t_{h, i-\frac{1}{2}}^{(k)} \right) \right] v_h(x_{i-\frac{1}{2}}^+) \\ &= \int_{I_i} \left[F(U_h(x, t)) - \sum_m s_m(c) (t_m)_h(x) \right] v'_h(x) dx - \left[\sum_{k=1}^3 \omega_k \left(F_{i+\frac{1}{2}}^{(k)} - \sum_m s_m(c) t_{h, i+\frac{1}{2}}^{(k)} \right) \right] \\ &\quad v_h(x_{i+\frac{1}{2}}^-) + \left[\sum_{k=1}^3 \omega_k \left(F_{i-\frac{1}{2}}^{(k)} - \sum_m s_m(c) t_{h, i-\frac{1}{2}}^{(k)} \right) \right] v_h(x_{i-\frac{1}{2}}^+). \end{aligned}$$

After applying condition (3.46) and rearranging terms, yields

$$T = \alpha \left[v_h(x_{i+\frac{1}{2}}^-) - v_h(x_{i-\frac{1}{2}}^+) \right] - \alpha v_h(x_{i+\frac{1}{2}}^-) + \alpha v_h(x_{i-\frac{1}{2}}^+) = 0.$$

Thus, the TVD-RK DG with the WAF scheme preserves exactly the stationary solution at steady state, this satisfies the exact C-property, hence, it is a well-balanced scheme. Since the weights in the TVD-WAF are not affect to the total truncation error, thus, the TVD-RK DG with the TVD-WAF scheme is also a well-balanced scheme. \square

Remark One can show that the developed well-balanced TVD-RK DG with WAF scheme in the case of existing source term is consistent by showing that the approximation of the source term is also consistent.

3.4 Numerical results

In this section, various experiments have been investigated to demonstrate the accuracy of the modified scheme for both steady and unsteady flows.

3.4.1 Dam break flow

It has been shown in the previous section that the WAF is consistent with the TVD-RK DG method. In this section, we apply this modified scheme for solving the SWE without source terms. The accuracy of numerical solutions is presented and compared with results from the standard TVD-RK DG with the HLL flux. The experiment is set up as follow.

The computational domain is $-5 \leq x \leq 5$ with the initial water depth

$$h(x, 0) = \begin{cases} 1, & \text{if } x \leq 0, \\ 0.6, & \text{if } x > 0. \end{cases} \quad (3.50)$$

The initial velocity is assumed to be zero and the boundary conditions are considered as transmissive boundaries. We perform 50, 100, and 200 cells in the numerical experiments. Polynomials of degree zero, one, and two are applied for local basis in the TVD-RK DG method. The root mean squared errors (RMS) of simulated results using WAF compared with those using HLL flux at $t = 2s$ and $\Delta t = 0.005s$ for various N and K are shown in Table 3.1.

N	Numerical Flux	$K = 50$	$K = 100$	$K = 200$
$N = 0$	HLL	0.0280	0.0215	0.0165
	WAF	0.0182	0.0127	0.0094
$N = 1$	HLL	0.0130	0.0102	0.0072
	WAF	0.0107	0.0093	0.0067
$N = 2$	HLL	0.0103	0.0079	0.0053
	WAF	0.0100	0.0076	0.0052

Table 3.1: RMS errors when $N = 0$, $N = 1$ and $N = 2$ for $K = 50$, 100 and 200 for WAF and HLL.

The results show that the accuracy of numerical solution obtained from the WAF is higher than those obtained from the HLL method, the RMS error decreases as K increases and the RMS error decreases as the polynomial of degree N increases.

The water depth profiles comparing between HLL and WAF at $t = 2s$ for $N = 1$ and $K = 100$ are shown in Figure 3.3 and Figure 3.4, respectively. The moving shock fronts are well captured for both HLL and WAF, however, WAF is slightly better for rarefaction wave. This experiment shows the accuracy of the TVD-RK DG with WAF, as an extension of the FVM [15].

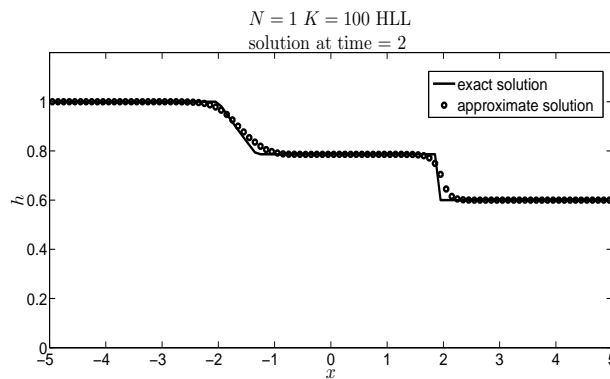


Figure 3.3: Exact solution and water depth profile obtained by the TVD-RK DG with HLL flux.

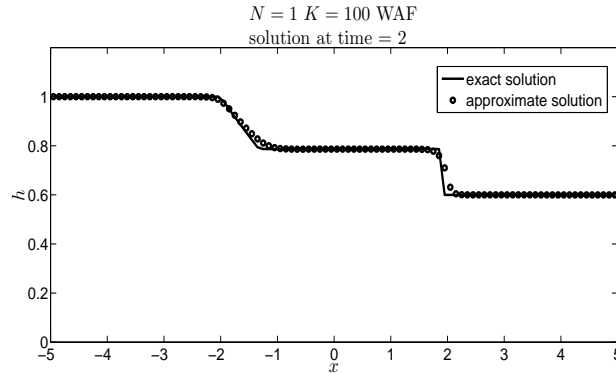


Figure 3.4: Exact solution and water depth profile obtained by the TVD-RK DG with WAF flux.

3.4.2 Flow over irregular bed

This experiment is set up on the uniform channel of length 1500 m with irregular bottom as shown in Figure 3.5. The problem is proposed by Lai and Bouchut [20] for testing the accuracy of numerical schemes at stationary state. The boundary conditions are transmissive with the initial water depth $h + z = 16$ m and zero initial velocity. The simulation runs until $t = 100$ s with $\Delta t = 0.01$ s.

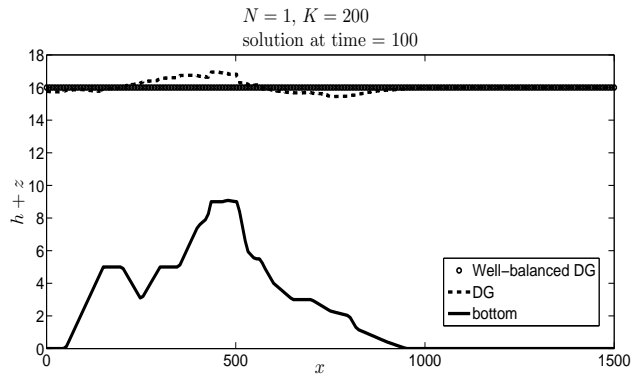


Figure 3.5: Stationary flows over irregular bottom produced by well-balanced and non well-balanced TVD-RK DG with WAF.

Figure 3.5 shows that the well-balanced scheme (dot) gives exactly the stationary solution, while the non well-balanced scheme (dash line) gives solution with high error, especially in the area where the bottom has high gradient.

3.4.3 Steady flow over a bump

In this experiment, we consider the shallow water flows over a bump in a rectangular channel of length 25 m. The bump elevation is

$$z(x) = \begin{cases} 0.2 - 0.05(x - 10)^2, & \text{if } 8 < x < 12, \\ 0, & \text{otherwise.} \end{cases} \quad (3.51)$$

At steady state, classical flows are characterized by subcritical flow, transcritical flow with shock, or transcritical flow without shock. The TVD-RK DG with WAF is performed for this problem. The accuracy of numerical result is investigated by comparing with the existing analytical solutions, see [10].

Subcritical flow over a bump

The upstream boundary is imposed by $Q = 4.42 \text{ m}^2/\text{s}$ and the downstream boundary $h = 2 \text{ m}$ with initial water depth $h + z = 2 \text{ m}$ and zero initial velocity. The simulation of the TVD-RK DG with $N=1$ is obtained using $\Delta t = 0.01\text{s}$. The comparison of RMS errors from HLL and WAF for various K is shown in Table 3.2, showing that WAF is slightly better than HLL.

	$K = 50$	$K = 100$	$K = 200$	$K = 400$
HLL	1.6954e-03	4.5563e-04	1.2546e-04	3.5900e-05
WAF	1.5816e-03	4.1648e-04	1.1474e-04	3.3019e-05

Table 3.2: RMS errors when $N = 1$ for subcritical flow over a bump for $K=50$, 100, 200 and 400.

The water depth and bump profiles are shown in Figure 3.6, displaying the agreement between the simulated result and the analytical solution.

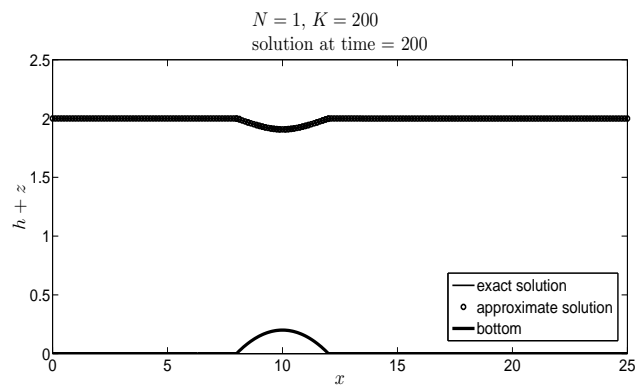


Figure 3.6: Water depth and bump profiles for subcritical flow.

Transcritical flow with shock over a bump

The upstream boundary is imposed by $Q = 0.18 \text{ m}^2/\text{s}$ and the downstream boundary $h = 0.33 \text{ m}$ with the initial water depth $h + z = 0.33 \text{ m}$. The comparison of water surfaces is shown in Figure 3.7, showing the agreement between the numerical result and the analytical result. This shows the accuracy of the well-balanced scheme by capturing the shock front without any oscillations.

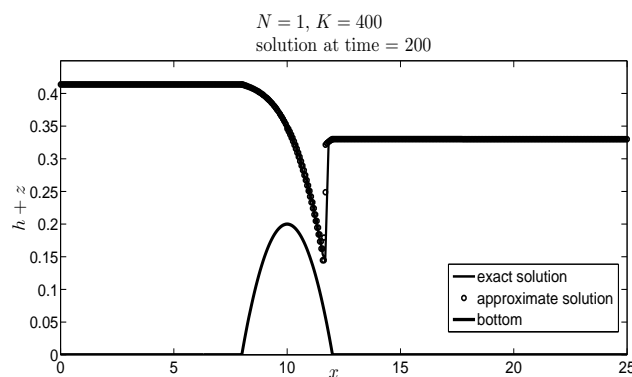


Figure 3.7: Transcritical flow with shock over a bump.

Transcritical flow without shock over a bump

The upstream boundary is imposed by $Q = 1.53 \text{ m}^2/\text{s}$ and the downstream boundary is not specified, with initial water depth $h + z = 0.4 \text{ m}$ and zero initial

velocity.

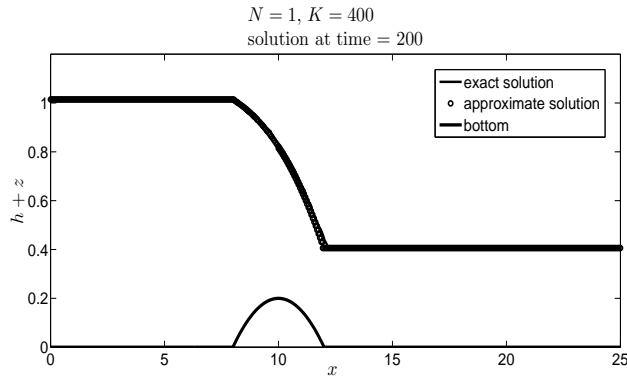


Figure 3.8: Transcritical flow without shock over a bump.

The comparison of the water depth profiles are shown in Figure 3.8, showing the agreement between the numerical result and the analytical solution. Therefore, the well-balanced scheme is accurate for transcritical flow problem.

3.4.4 Small perturbation of steady state water

This experiment was first proposed by [23, 24, 25] to study the capability of numerical schemes for small perturbation in shallow water flows. In this experiment, the bottom topography is

$$z(x) = \begin{cases} 0.25 (\cos(10\pi(x - 1.5)) + 1), & \text{if } 1.4 < x < 1.6, \\ 0. & \text{otherwise.} \end{cases} \quad (3.52)$$

The initial conditions are specified by

$$q(x, 0) = 0 \quad \text{and} \quad h(x, 0) = \begin{cases} 1 - z(x) + \epsilon, & \text{if } 1.1 < x < 1.2, \\ 1 - z(x), & \text{otherwise,} \end{cases} \quad (3.53)$$

where ϵ is a non-zero perturbation constant. The boundary conditions are transmissive boundaries. In this work, we consider the cases of $\epsilon = 0.2$ and 0.01 . The disturbance of initial water depth from small ϵ splits the initial wave into two

waves, the left and the right waves with characteristic speed $\pm\sqrt{gh}$ at the early stage. A standard non well-balanced scheme usually has difficulty to capture the wave speed correctly.

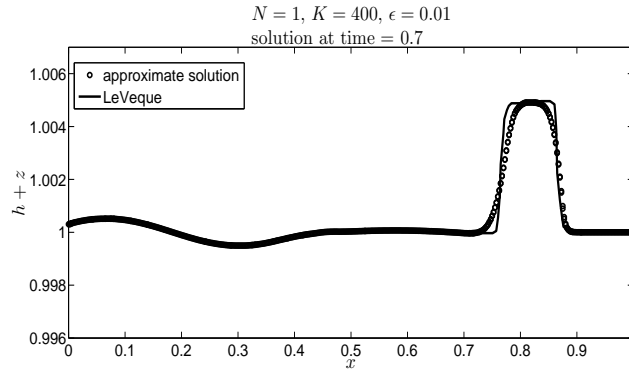


Figure 3.9: Quasi-stationary flow for $\epsilon = 0.01$.

The simulation result is produced using 400 uniform grid cells for the TVD-RK DG degree one with WAF and run for $t = 0.7s$.

The comparison of water depths between the simulated results and the LeVeque's solutions [24] is shown in Figures 3.9 and 3.10 for $\epsilon = 0.01$ and 0.2 , respectively, which are in good agreement in terms of the amplitude and wave speed.

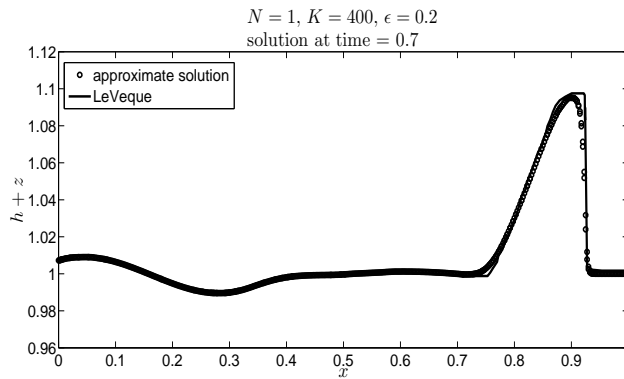


Figure 3.10: Quasi-stationary flow for $\epsilon = 0.2$.

3.4.5 Flow over non-horizontal bed

This experiment is carried out based on result in [39], to study the ability of numerical schemes for unsteady flows over topography. The experiment is set on the uniform channel of length 30 m with bottom elevation

$$z(x) = \begin{cases} 0, & \text{if } 0 \leq x < 10, \\ 0.1(x - 10), & \text{if } 10 \leq x < 20, \\ 1, & \text{if } 20 \leq x \leq 30, \end{cases} \quad (3.54)$$

and initial water depth

$$h(x) + z(x) = \begin{cases} 4, & \text{if } 0 \leq x < 5, \\ 2, & \text{if } 5 \leq x \leq 30. \end{cases} \quad (3.55)$$

The simulation is obtained by using $\Delta t = 0.01s$ on 200 uniform grid cells for polynomial degree one with transmissive boundaries.

The comparison of simulated results with the Toro's solutions [39] at $t = 1s$ and $4s$ are shown in Figure 3.11 and 3.12, respectively, showing the agreement of both results in term of the wave speed and shock profiles.

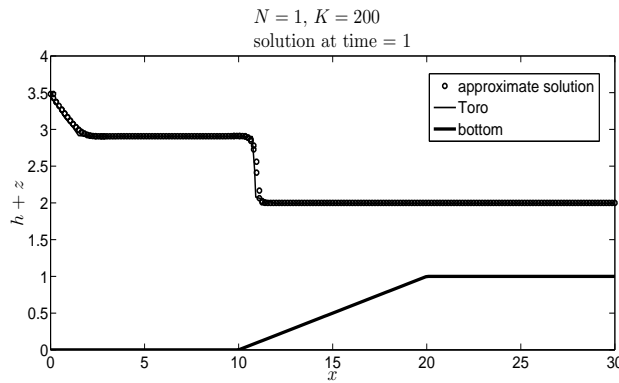


Figure 3.11: Flows over non-horizontal bed at time 1s.

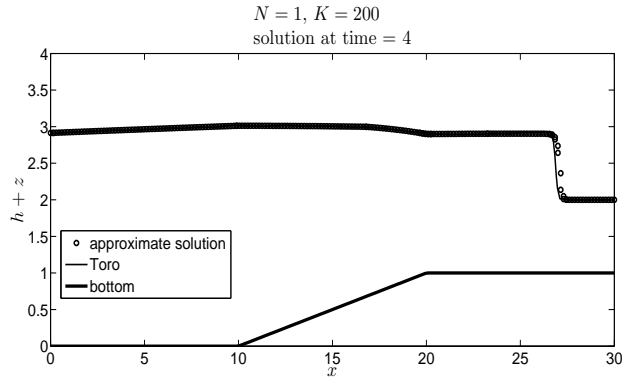


Figure 3.12: Flows over non-horizontal bed at time $4s$.

3.5 Conclusions

In this Chapter, we present the TVD-RK DG method for solving nonlinear SWE. Most of the TVD-RK DG methods in the literature usually approximate flux at cell interfaces by applying the HLL method, here, another approach called the WAF is applied. The consistent property of the TVD-RK DG with the WAF approximation is shown in Section 3.2, then the well-balanced TVD-RK DG scheme with the WAF approximation is developed. It is used to simulate various experiments for steady and unsteady flows. The high accuracy of developed numerical scheme is demonstrated by various test cases such as flow over irregular bed, steady flow over a bump, quasi-stationary, and flow over non-horizontal bed. The well-balanced TVD-RK DG with the WAF method can be used to solve all the kinds of these problems. Due to its advantages of numerical accuracy, simplicity and well-balanced property, the presented scheme can be modified and extended to simulate two-dimensional problems. However, depending on the types of elements, e.g., triangles or rectangles, it is not trivial to extend for two-dimensional problems due to the polynomial basis functions and the WAF fluxes at cell interfaces, and is not considered in this work.

CHAPTER IV

FINITE VOLUME METHOD FOR ONE-DIMENSIONAL SHALLOW WATER EQUATIONS IN ARBITRARY CROSS-SECTIONAL AREA

In this Chapter, the reconstruction and bottom modification techniques for open channel flow in arbitrary cross-sectional area is presented. We applied finite volume method (FVM) with HLL flux to approximate SWE in arbitrary cross-sectional area, where the difficulty usually occurs when dealing with wet/dry areas. To improve the efficiency and stability of the numerical scheme when dealing with wet/dry problem, we apply the reconstruction and bottom modification techniques. Various numerical experiments are presented to show good agreement with results in literature, which confirm the accuracy of the proposed scheme. Moreover, it also preserves the still water stationary solution and the conservation of mass. In addition, the proposed scheme is applied to simulate water flow in Yom river, Phrae province, where the results agree very well with the measured data.

4.1 Finite volume method for one-dimensional shallow water equations in arbitrary cross-sectional area

Consider the one-dimensional SWE in arbitrary cross-sectional area

$$U_t + F(U)_x = S(U), \quad (4.1)$$

where

$$U = \begin{pmatrix} A \\ Q \end{pmatrix}, F(U) = \begin{pmatrix} Q \\ \frac{Q^2}{A} \end{pmatrix}, \text{ and } S(U) = \begin{pmatrix} 0 \\ -gAZ_x - g\frac{n^2Q|Q|}{R^{4/3}A} \end{pmatrix}. \quad (4.2)$$

This equation is sometimes called the Saint Venant equations. The first and the second component of the flux function in (4.2) are denoted by $f_1 = Q$ and $f_2 = \frac{Q^2}{A}$, respectively, where A is a wetted cross-sectional area, $Q = Au$ is a discharge, u is a velocity, g is a acceleration due to gravity, $Z = h + z$ is a water surface level, z is a bottom elevation, h is a water depth, n is the Manning's roughness coefficient, $R = A/P$ is the hydraulic radius, and P is the wetted perimeter of the channel. A prototype cross-section of a channel is shown in Figure 4.1, where B is the channel width measured at the water surface.

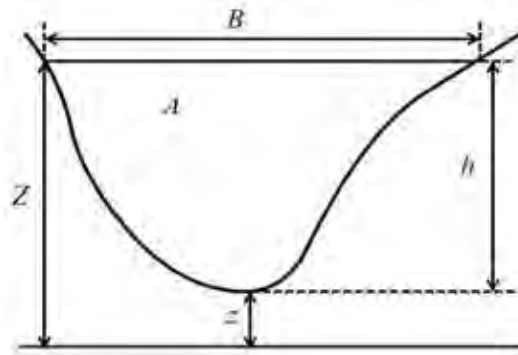


Figure 4.1: Cross-section of a channel.

The computational domain of length L is partitioned into K cells with uniform cell size $\Delta x = x_{i+\frac{1}{2}} - x_{i-\frac{1}{2}}$, where $x_{i-\frac{1}{2}}$ and $x_{i+\frac{1}{2}}$ are the left and the right interfaces of the cell, respectively, and cell i is denoted by $I_i = [x_{i-\frac{1}{2}}, x_{i+\frac{1}{2}}]$, for $i = 1, \dots, K$. In the FVM, the discretized form of (4.1) is

$$U_i^{n+1} = U_i^n - \frac{\Delta t}{\Delta x} \left[\widehat{F}_{i+\frac{1}{2}}^n - \widehat{F}_{i-\frac{1}{2}}^n \right] + \Delta t S_i^n, \quad (4.3)$$

where $\Delta t = t^{n+1} - t^n$, U_i^n is the cell average of U over cells I_i at time t^n defined by

$$U_i^n = \frac{1}{\Delta x} \int_{I_i} U(x, t^n) dx. \quad (4.4)$$

Here, $\widehat{F}_{i-\frac{1}{2}}^n$ and $\widehat{F}_{i+\frac{1}{2}}^n$ are the numerical fluxes at the left and the right interfaces of the cell at time t^n , respectively, the numerical fluxes for f_1 and f_2 components at $i +$

1/2 are denoted by $(\widehat{f}_1)_{i+\frac{1}{2}}^n$ and $(\widehat{f}_2)_{i+\frac{1}{2}}^n$, respectively, and S_i^n is the approximation of the source terms at time t^n .

4.1.1 Harten-Lax-van Leer flux (HLL flux)

We approximate fluxes $\widehat{F}_{i\pm\frac{1}{2}}$ at the left and the right interfaces in (4.3) by the HLL approximate Riemann solver [19, 21, 22, 40, 41, 50, 51] as first proposed by Harten, Lax and van Leer [13]. For instance, the HLL flux at interface $i + 1/2$ of the Saint Venant equations at arbitrary time is given by

$$\widehat{F}_{i+\frac{1}{2}}^{HLL}(U_L, U_R) = \begin{cases} F(U_L), & \text{if } S_L \geq 0, \\ F_{i+\frac{1}{2}}^*, & \text{if } S_L < 0 < S_R, \\ F(U_R), & \text{if } S_R \leq 0, \end{cases} \quad (4.5)$$

where $U_L = U_i$, $U_R = U_{i+1}$ which are the limits of the solution from the left and right of the interface, $F(U_L) = F(U_i)$, $F(U_R) = F(U_{i+1})$, and S_L and S_R are the left and the right wave speeds defined below. As proposed by Ying and Wang [50, 51], in the case of arbitrary cross-sectional area, $F_{i+\frac{1}{2}}^* = (f_1^*, f_2^*)^T$, where

$$f_1^* = \frac{S_R B_{i+1} (f_1)_i - S_L B_i (f_1)_{i+1} + S_L B_i S_R B_{i+1} (Z_{i+1} - Z_i)}{S_R B_{i+1} - S_L B_i}, \quad (4.6)$$

$$f_2^* = \frac{S_R (f_2)_i - S_L (f_2)_{i+1} + S_L S_R (Q_{i+1} - Q_i)}{S_R - S_L}. \quad (4.7)$$

For wet bed problem, the left and the right wave speeds can be estimated by

$$S_L = \min \left(u_i - \sqrt{g \bar{h}_i}, u^* - \sqrt{g \bar{h}^*} \right), \quad (4.8)$$

$$S_R = \max \left(u_{i+1} + \sqrt{g \bar{h}_{i+1}}, u^* + \sqrt{g \bar{h}^*} \right), \quad (4.9)$$

see [21, 22, 41, 50, 51], where $\bar{h}_i = A_i/B_i$ and $\bar{h}_{i+1} = A_{i+1}/B_{i+1}$ are the averages of water depths, the velocity in the intermediate region u^* is approximated by

$$u^* = \frac{1}{2}(u_i + u_{i+1}) + \sqrt{g \bar{h}_i} - \sqrt{g \bar{h}_{i+1}} \quad (4.10)$$

and

$$\sqrt{g\bar{h}^*} = \frac{1}{2} \left(\sqrt{g\bar{h}_i} + \sqrt{g\bar{h}_{i+1}} \right) + \frac{1}{4}(u_i - u_{i+1}). \quad (4.11)$$

For the wet/dry problem, when the right cell is dry, the wave speed can be estimated by

$$S_L = u_i - \sqrt{g\bar{h}_i} \quad \text{and} \quad S_R = u_i + 2\sqrt{g\bar{h}_i}. \quad (4.12)$$

For the left dry bed problem, they can be estimated by

$$S_L = u_{i+1} - 2\sqrt{g\bar{h}_{i+1}} \quad \text{and} \quad S_R = u_{i+1} + \sqrt{g\bar{h}_{i+1}}. \quad (4.13)$$

Thus, the HLL fluxes $\hat{F}_{i\pm\frac{1}{2}}^{HLL}$ can be calculated at each time step t^n and substituted into (4.3). The diagram for the HLL corresponding to the Riemann problem at interface $i + 1/2$ is shown in Figure 4.2.

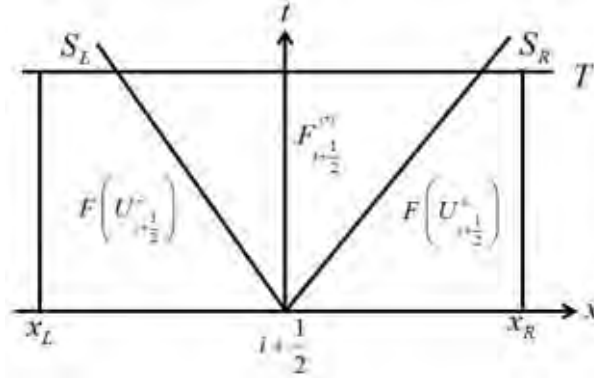


Figure 4.2: The wave structure diagram for HLL corresponding to the Riemann problem.

4.1.2 An approximation of the source term

We follow the idea proposed in [50, 51] to approximate the source terms S_i^n in (4.3), which includes of the water surface gradient and the friction term. First, the water surface gradient for cell i is approximated using the central difference scheme

$$(Z_x)_i^n = \frac{Z_{i+1}^n - Z_{i-1}^n}{x_{i+1} - x_{i-1}}. \quad (4.14)$$

The friction term is approximated using a splitting scheme in which we obtain the solution A and Q at the next time step as follows

$$A_i^{n+1} = A_i^n - \frac{\Delta t}{\Delta x} \left[\left(\widehat{f}_1 \right)_{i+\frac{1}{2}}^n - \left(\widehat{f}_1 \right)_{i-\frac{1}{2}}^n \right], \quad (4.15)$$

$$Q_i^{*,n} = Q_i^n - \frac{\Delta t}{\Delta x} \left[\left(\widehat{f}_2 \right)_{i+\frac{1}{2}}^n - \left(\widehat{f}_2 \right)_{i-\frac{1}{2}}^n \right] - \Delta t (g A_i^n (Z_x)_i^n), \quad (4.16)$$

$$Q_i^{n+1} = Q_i^{*,n} - \Delta t \left(g \frac{n^2 Q_i^{*,n} |Q_i^{*,n}|}{(R_i^n)^{4/3} A_i^n} \right). \quad (4.17)$$

where $Q_i^{*,n}$ is the intermediate value of Q obtained from (4.16).

4.2 Reconstruction and bottom modification techniques for wet/dry problems

In order to improve the stability and efficiency of handling the wet/dry problem, we extend the idea in [3] from uniform to arbitrary cross-sectional areas. There are 2 steps as follows

Step 1 *Reconstruction for non-negativity of the water depth*

We consider only the interface $i + 1/2$ of cell i for arbitrary time, thus, we omit superscript n . If the interface is detected as a wet/dry interface, we reconstruct the left and the right limits of water depths to be the following new values

$$h_{i+\frac{1}{2}}^- = \max \left(0, h_i + z_i - z_{i+\frac{1}{2}} \right), \quad (4.18)$$

$$h_{i+\frac{1}{2}}^+ = \max \left(0, h_{i+1} + z_{i+1} - z_{i+\frac{1}{2}} \right). \quad (4.19)$$

Here, we set $z_{i+\frac{1}{2}} = \max(z_i, z_{i+1})$. Then, the water surface at interface $i + 1/2$ can be computed directly as $Z_{i+\frac{1}{2}}^- = h_{i+\frac{1}{2}}^- + z_{i+\frac{1}{2}}$ and $Z_{i+\frac{1}{2}}^+ = h_{i+\frac{1}{2}}^+ + z_{i+\frac{1}{2}}$, Figure 4.3 is a conceptual sketch showing the reconstruction variables $h_{i+\frac{1}{2}}^\pm$. Similar reconstructions are applied at the interface $i - 1/2$ of cell i .

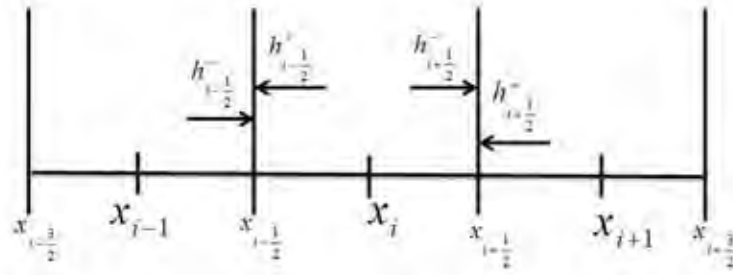


Figure 4.3: The limits from the left and the right of the variable h for cell i at interface $i - 1/2$ and $i + 1/2$.

Step 2 *Bottom modification*

To resolve the difference between the actual and modified water surface level that occurs in Step 1, we extend the idea developed in [26].

If the interface under consideration is dry on the left side, we modify the water surface and bottom again by

$$\tilde{Z}_{i+\frac{1}{2}}^- = Z_{i+\frac{1}{2}}^- - \Delta z \quad \text{and} \quad \tilde{Z}_{i+\frac{1}{2}}^+ = Z_{i+\frac{1}{2}}^+ - \Delta z, \quad (4.20)$$

where $\Delta z = \max(0, z_{i+\frac{1}{2}} - (h_{i+1} + z_{i+1}))$ and the water depths are kept at the same values, i.e., $\tilde{h}_{i+\frac{1}{2}}^- = h_{i+\frac{1}{2}}^-$ and $\tilde{h}_{i+\frac{1}{2}}^+ = h_{i+\frac{1}{2}}^+$.

The values of $\tilde{A}_{i+\frac{1}{2}}^-$ and $\tilde{A}_{i+\frac{1}{2}}^+$ are obtained directly by using $\tilde{h}_{i+\frac{1}{2}}^-$ and $\tilde{h}_{i+\frac{1}{2}}^+$, the discharges $\tilde{Q}_{i+\frac{1}{2}}^- = \tilde{A}_{i+\frac{1}{2}}^- u_i$ and $\tilde{Q}_{i+\frac{1}{2}}^+ = \tilde{A}_{i+\frac{1}{2}}^+ u_{i+1}$, and we define the vector of modified variables by $\tilde{U}_{i+\frac{1}{2}}^- = (\tilde{A}_{i+\frac{1}{2}}^-, \tilde{Q}_{i+\frac{1}{2}}^-)^T$ and $\tilde{U}_{i+\frac{1}{2}}^+ = (\tilde{A}_{i+\frac{1}{2}}^+, \tilde{Q}_{i+\frac{1}{2}}^+)^T$, respectively. For the case of dry bed on the right side of the interface, we calculate similarly, by using $\Delta z = \max(0, z_{i+\frac{1}{2}} - (h_i + z_i))$.

In order to approximate the water surface gradient source term, all of the modified variables are used as follows

$$-gA(Z_x)_i = -g \left(\frac{\bar{A}_{i+\frac{1}{2}} + \bar{A}_{i-\frac{1}{2}}}{2} \right) \left(\frac{\bar{Z}_{i+\frac{1}{2}} - \bar{Z}_{i-\frac{1}{2}}}{\Delta x} \right), \quad (4.21)$$

where $\bar{A}_{i+\frac{1}{2}} = \frac{(\tilde{A}_{i+\frac{1}{2}}^- + \tilde{A}_{i+\frac{1}{2}}^+)}{2}$, $\bar{A}_{i-\frac{1}{2}} = \frac{(\tilde{A}_{i-\frac{1}{2}}^- + \tilde{A}_{i-\frac{1}{2}}^+)}{2}$, $\bar{Z}_{i+\frac{1}{2}} = \frac{(\tilde{Z}_{i+\frac{1}{2}}^- + \tilde{Z}_{i+\frac{1}{2}}^+)}{2}$,
and $\bar{Z}_{i-\frac{1}{2}} = \frac{(\tilde{Z}_{i-\frac{1}{2}}^- + \tilde{Z}_{i-\frac{1}{2}}^+)}{2}$.

In our work, the numerical scheme with reconstruction (step 1-2) is referred to as scheme II and the scheme without reconstruction is referred to as scheme I. Similar work for scheme I can be seen in [50, 51].

Summary of algorithm for scheme I

1. Given the initial condition U_i^0 , $i = 1, 2, \dots, K$.
2. Compute the numerical flux $\hat{F}_{i\pm\frac{1}{2}}^{HLL}$ and the water surface gradient source term by using (4.5) and (4.14), respectively.
3. Update the solution for A_i^{n+1} and Q_i^{n+1} by using (4.15)-(4.17).

Summary of algorithm for scheme II

1. Given the initial solution U_i^0 , $i = 1, 2, \dots, K$.
2. Reconstruct and modify the variables h , z , Z , A , and Q using steps 1 and 2 in Section 4.2.
3. Use the reconstructed and modified variables to compute the numerical flux $\hat{F}_{i\pm\frac{1}{2}}^{HLL}$ and water surface gradient source term by using (4.5) and (4.21), respectively.
4. Update the solution for A_i^{n+1} and Q_i^{n+1} by using (4.15)-(4.17).

Note that when we obtain A_i^{n+1} , we can solve for h_i^{n+1} using the Newton's method.

4.3 Numerical Results

In this section, we validate the proposed scheme II by running numerical experiments using various open channel flow problems available in the literature [4, 12, 17, 20, 21, 22, 30, 48].

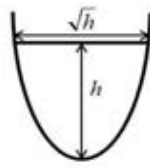
4.3.1 Dam break in various channels

In this experiment, we consider the dam break flows in open channel with frictionless, flat bottoms of different cross-sectional shapes, including parabolic, triangular, and trapezoidal. The numerical results are compared with the exact solutions [21, 22] to assess the accuracy of the our presented scheme.

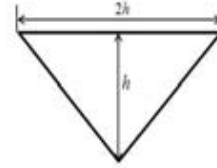
Dam break in parabolic channel

In this experiment, a 1000 m long parabolic channel with top width $B = \sqrt{h}$ and wetted area $A = \frac{2}{3}h^{3/2}$ is considered. The cross-section of the parabolic channel is shown in Figure 4.4(a). The wall of the dam is located at 500 m from upstream. The initial velocity is zero, with the initial water depth

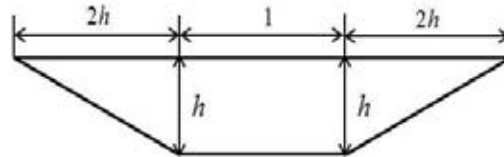
$$h(x, 0) = \begin{cases} 10, & \text{if } x \leq 500, \\ 1, & \text{if } x > 500. \end{cases} \quad (4.22)$$



(a) The parabolic channel.



(b) The triangular channel.



(c) The trapezoidal channel.

Figure 4.4: The cross-sectional areas of parabolic, triangular, and trapezoidal channel.

The simulation is run on uniform 400 grid cells for 20s with time step $\Delta t = 0.05s$. Figure 4.5 shows comparisons of the water depth and the discharge between the approximate solutions and the exact solutions. The numerical scheme can capture the shock and rarefaction well when compared with the exact solution given in [22].

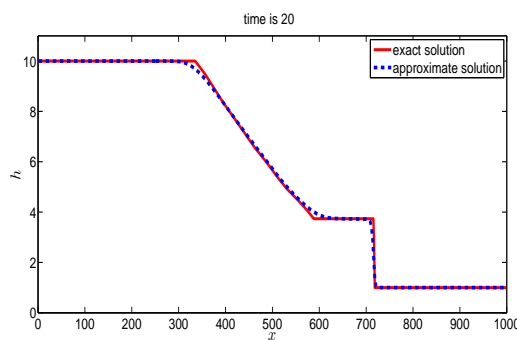
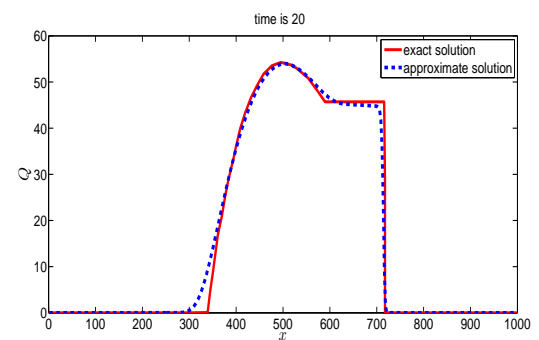
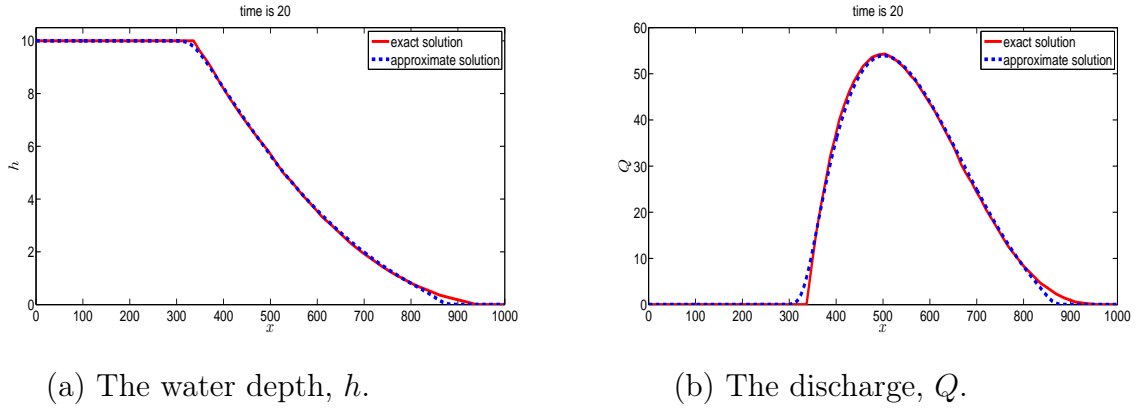
(a) The water depth, h .(b) The discharge, Q .

Figure 4.5: Comparisons of the water depth (a) and the discharge (b) between the exact solutions and the approximate solutions at 20s for dam break in a parabolic channel (wet bed problem).

The experiment for the dry bed case is performed similar to the wet bed case, except that the water depth $h = 0$ for $x > 500$ m. This case is simulated using 1000 uniform grid cells and $\Delta t = 0.0001s$. The approximate solutions of water depth and discharge at final time 20s are shown in Figures 4.6(a) and (b), which are in good agreement with the exact solutions shown in [22].



(a) The water depth, h .

(b) The discharge, Q .

Figure 4.6: Comparisons of the water depth (a) and the discharge (b) between the exact solutions and the approximate solutions at 20s for dam break in parabolic channel (dry bed problem).

Dam break in triangular channel

Here, we consider a 1000 m long triangular channel with width $B = 2h$ and wetted area $A = h^2$. The cross-sectional area of triangular channel is show in Figure 4.4(b). The initial water depth is set at

$$h(x, 0) = \begin{cases} 1, & \text{if } x \leq 500, \\ 0.1, & \text{if } x > 500, \end{cases} \quad (4.23)$$

with zero initial velocity. The simulation is performed using $K = 400$ and $\Delta t = 0.125s$. The simulation shows a rarefaction that moves to the left and a shock that moves to the right. Figure 4.7 shows the water depth and the discharge at 80s, which agree very well with the exact solution provided in [21].

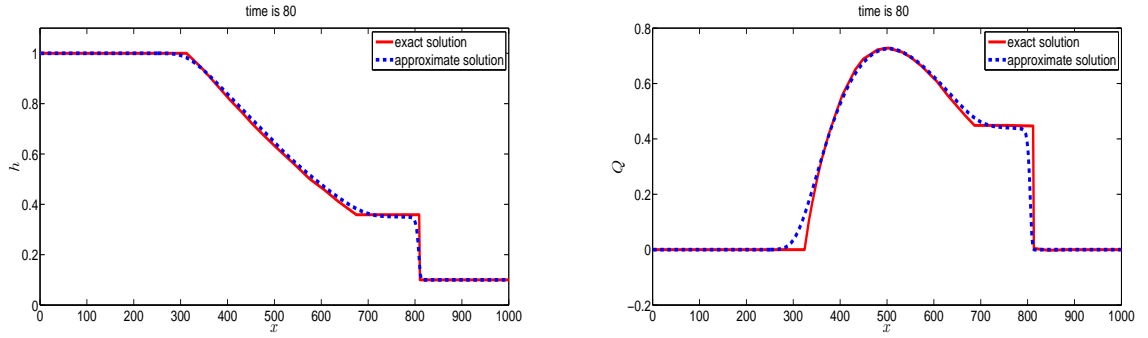
(a) The water depth, h .(b) The discharge, Q .

Figure 4.7: Comparisons of the water depth (a) and the discharge (b) between the approximate solutions and the exact solutions at 80s for dam break flow in triangular channel (wet bed problem).

Dam break in trapezoidal channel

This experiment consider a 1000 m long trapezoidal channel, with width $B = 1 + 4h$ and wetted area $A = h + 2h^2$. The cross-sectional area of the channel is shown in Figure 4.4(c). We set the initial water depth as

$$h(x, 0) = \begin{cases} 1, & \text{if } x \leq 500, \\ 0.1, & \text{if } x > 500. \end{cases} \quad (4.24)$$

The simulation is performed on 400 uniform grid cells with zero initial velocity and $\Delta t = 0.1s$. Figure 4.8 shows the comparisons of the water depth and the discharge between our approximate solutions and the exact solutions provided in [21] at 103.1s, which agree well.

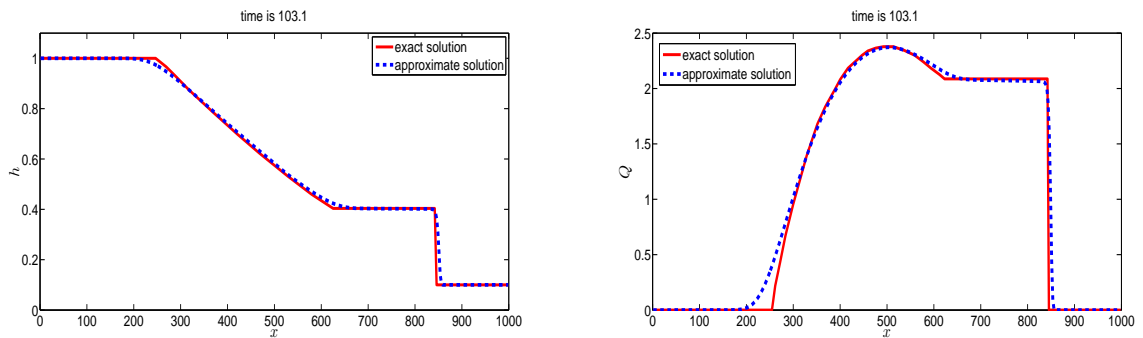
(a) The water depth, h .(b) The discharge, Q .

Figure 4.8: Comparisons of the water depth (a) and the discharge (b) between the exact solutions and the approximate solutions for dam break flow in trapezoidal channel.

4.3.2 Still water in parabolic channel

This experiment is designed to test the ability of the numerical scheme II to preserve the still water solution in the parabolic channel described in section 4.3.1. The computational domain is 1500 m with irregular bottom proposed in [20]. The simulation is performed on 100 uniform grid cells with initial water surface, $Z(x, 0) = 16$ and zero velocity. The numerical solution at $t = 100s$ is shown in Figure 4.9, illustrating that our numerical scheme preserves the still water solution exactly.

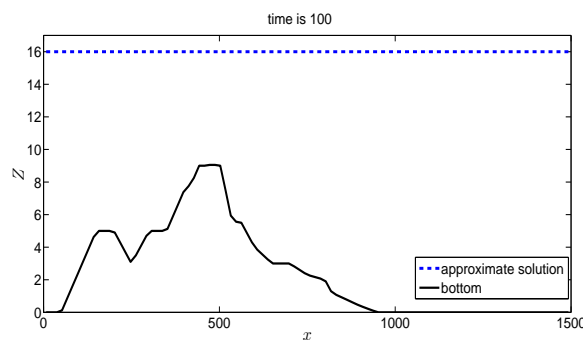


Figure 4.9: The still water with irregular bed in parabolic channel.

To test the ability of the scheme to handle wet/dry still water stationary state, an additional calculation is performed with initial conditions $Z = \max(z, 6)$ and

$u(x, 0) = 0$. The numerical result at $t = 100s$ is presented in Figure 4.10, showing that the scheme also preserves the still water stationary solution in the case of the wet/dry problem.

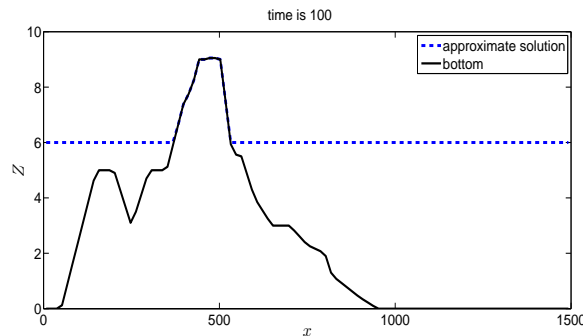
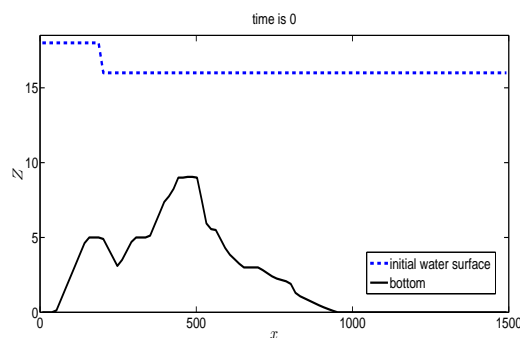
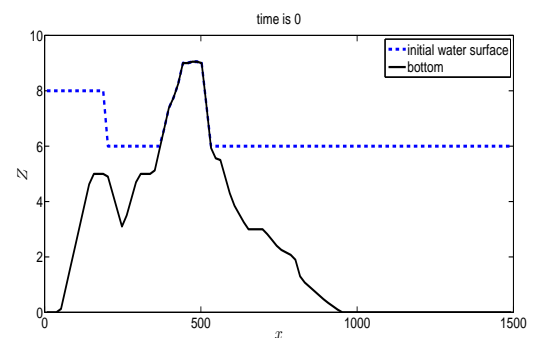


Figure 4.10: The wet/dry still water with irregular bed in parabolic channel.

To illustrate the capability of scheme II to converge to the steady state solution, additional calculation are performed in the parabolic channel with irregular bottom similar to still water experiments for both wet and wet/dry bed problems. The initial water surface are $Z = 18$ for $x \leq 200$ and $Z = 16$ otherwise, for wet bed problem, and $Z = 8$ for $x \leq 200$ and $Z = \max(z, 6)$ otherwise, for wet/dry problem with zero initial velocity for both cases. The initial water surfaces are shown in Figure 4.11.



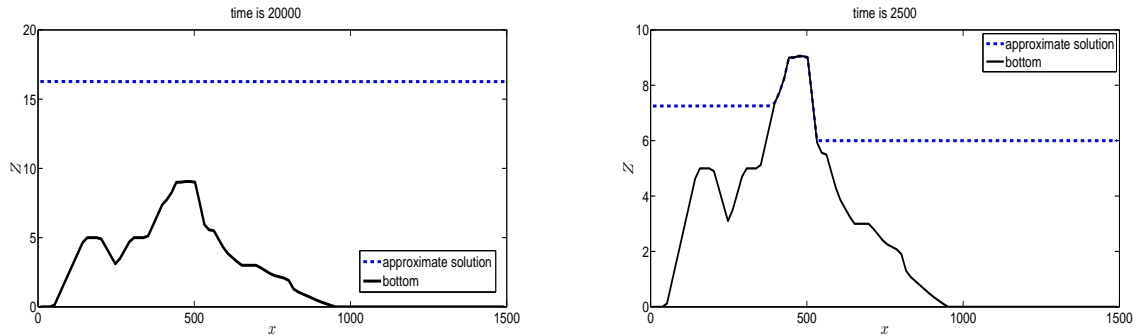
(a) The initial water surface for wet bed problem.



(b) The initial water surface for wet/dry bed problem.

Figure 4.11: The initial water surfaces for still water stationary solution problems.

The simulations are performed on 100 uniform grid cells with reflective boundary conditions on both sides, until the steady states are reached. The approximate solutions for both cases are shown in Figure 4.12. These solutions converge to the still water solution at steady state.



(a) The simulated water surface for wet bed problem.

(b) The simulated water surface for wet/dry bed problem.

Figure 4.12: The simulated water surfaces for still water stationary solutions.

4.3.3 Riemann problem in non-prismatic channel

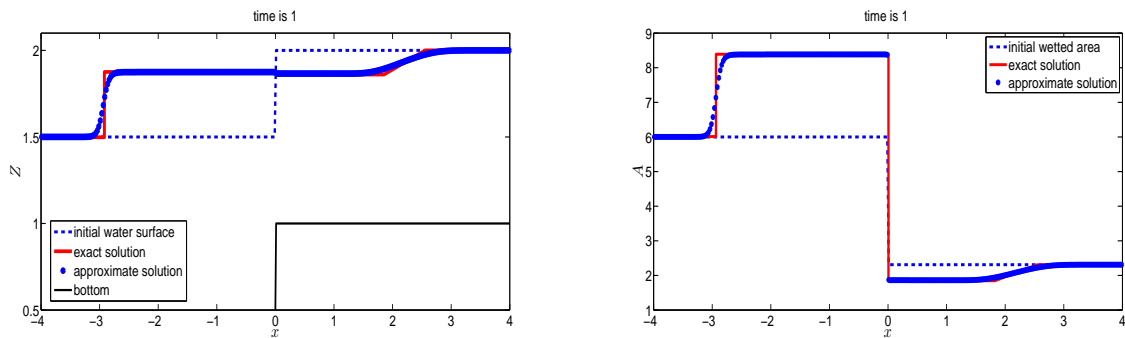
This experiment is similar to the one proposed by Murillo and Navarro [30]. We consider dam break problem in a non-prismatic channel with a non flat bottom to test the accuracy of numerical scheme II. The domain is defined as $-10 \leq x \leq 10$. The channel width is $B = \sqrt{B_0 h}$ with the wetted area $A = \frac{2}{3} h^{3/2}$. The simulation is performed on 800 uniform cells with $\Delta t = 0.001s$. The bottom, z , has a discontinuity at $x = 0$, where the initial conditions and bottom profile are given as follows

$$h(x, 0) = \begin{cases} 1.5, & \text{if } x < 0, \\ 1, & \text{if } x \geq 0, \end{cases} \quad u(x, 0) = \begin{cases} 1, & \text{if } x < 0, \\ 0, & \text{if } x \geq 0 \end{cases} \quad (4.25)$$

and

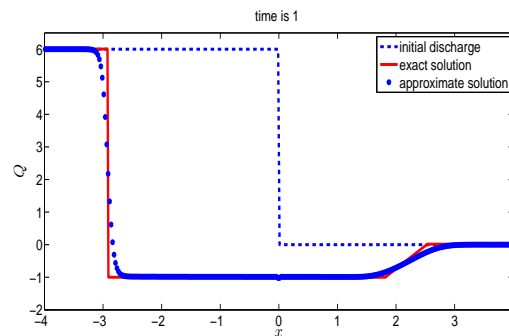
$$z(x) = \begin{cases} 0, & \text{if } x < 0, \\ 1, & \text{if } x \geq 0, \end{cases} \quad B_0(x) = \begin{cases} 24, & \text{if } x < 0, \\ 12, & \text{if } x \geq 0. \end{cases} \quad (4.26)$$

The simulation of water depth in this experiment consists of a shock wave moving to the left and a rarefaction wave moving to the right. The comparisons of water depth, wetted area and discharge between the approximate solutions and the exact solutions provided in [30] at 1s are shown in Figure 4.13. This shows the accuracy and capability of the numerical scheme II to handle flow in non-prismatic channel over a non flat bottom.



(a) The water surface Z .

(b) The wetted area A .



(c) The discharge Q .

Figure 4.13: The comparisons of the water depth, the wetted area and the discharge between the exact solutions and the approximate solutions for Riemann problem in a non-prismatic channel.

4.3.4 Oscillatory flow in a parabolic bowl without friction effects

This experiment is performed to check the capability of the numerical scheme for an oscillating flow in parabolic bowl with the bottom

$$z(x) = h_0 (x/a)^2, \quad (4.27)$$

where h_0 and a are constants. The simulation is performed with $h_0 = 10$ m and $a = 3000$ m on the computational domain $-5000 \leq x \leq 5000$ m in uniform rectangular channel, as described in [17]. In this experiment, the flow has wet/dry interfaces that are oscillating up and down in the parabolic bowl. This is a challenging test of the numerical scheme's capability to handle wet/dry problems. The simulation is performed on 400 uniform grid cells and simulated until $t = 2000$ s. The result from the numerical scheme II is shown in Figure 4.14, which agree very well with the exact solution given in [17].

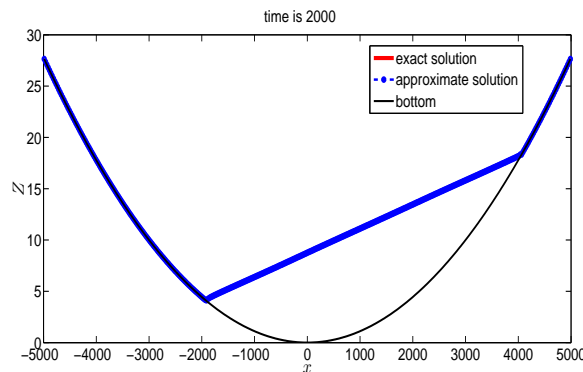


Figure 4.14: The comparison of the water surface between the approximate solution and the exact solution for oscillatory flow in a parabolic bowl without friction effects.

When comparing between scheme I and II based on the largest Courant-Friedrichs-Levy (CFL) number, the CFL numbers for schemes I and II are 0.0991 and 0.3962, respectively. This implies that scheme II is more efficient in term of stability than

scheme I. If scheme I is applied with CFL=0.3962, the approximate solution is oscillate as shown in Figure 4.15.

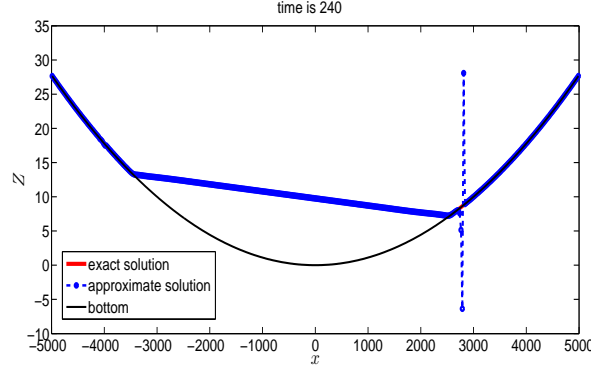


Figure 4.15: The comparison of the water surface between the approximate solution from scheme I with CFL=0.3962 and the exact solution.

4.3.5 Dam break flow over a discontinuous bottom

This experiment is performed to investigate the capability of the scheme to handle the wet/dry problem for steady flow with a discontinuous bottom. The flow is considered on a 25 m long trapezoidal channel similar to that described in section 4.3.1, with a frictionless discontinuous bottom defined by

$$z(x) = \begin{cases} 0.5, & \text{if } 8 \leq x \leq 12, \\ 0, & \text{otherwise.} \end{cases} \quad (4.28)$$

The initial water surface is

$$Z(x) = \begin{cases} 1, & \text{if } x \leq 3, \\ 0, & \text{otherwise} \end{cases} \quad (4.29)$$

with zero initial velocity and reflective boundary conditions on both boundaries. The simulation is performed using 500 uniform grid cells with $\Delta t = 0.001s$ until the steady state is reached. The result of the water surface at steady state is shown in Figure 4.16, illustrating that the approximate solution produced by scheme II

converges to the still water steady state. We have also checked the conservation of mass of the presented scheme by setting an initial mass in our simulation as 36, which remains the same as 36 for all running time $t = 0s$ to $t = 500s$. This demonstrates that our scheme preserves mass during time integration.

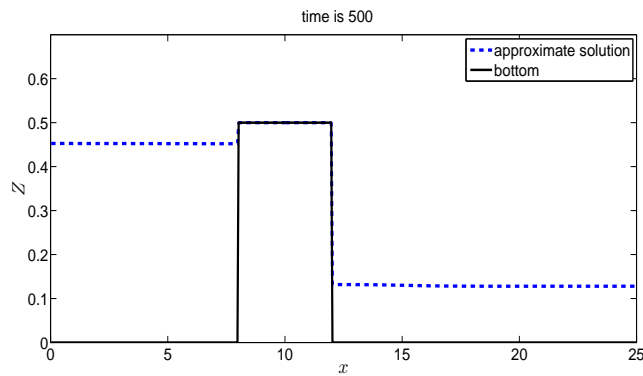


Figure 4.16: The steady state water surface of the dam break flow over a discontinuous bottom simulated by scheme II with $\Delta t = 0.001s$.

As illustrating in Figure 4.17, the result obtained from the Scheme I does not preserve the mass and the non-negativity of the water depth during the time integration, even with smaller Δt . Figure 4.18 shows that the result at steady state from scheme I with $\Delta t = 0.0005s$, displaying the negative water depth in some areas. The comparison of the simulated water surfaces from schemes I and II with $K = 500$ in the area that water depth from scheme I is negative is shown in Figure 4.19. These results show that scheme II is more robust than scheme I in the case of wet/dry problems with a discontinuous bottom.

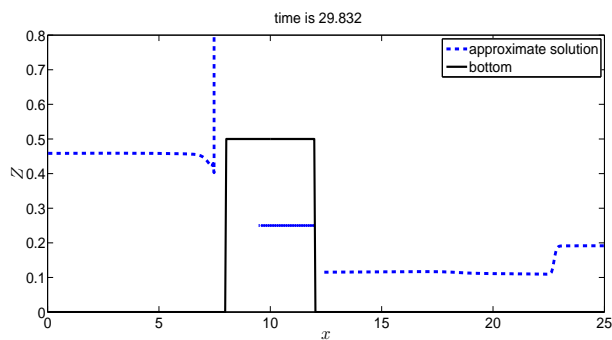
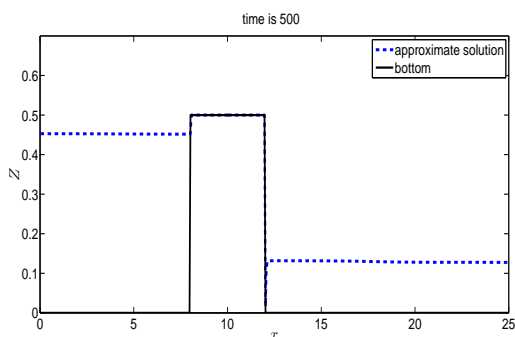
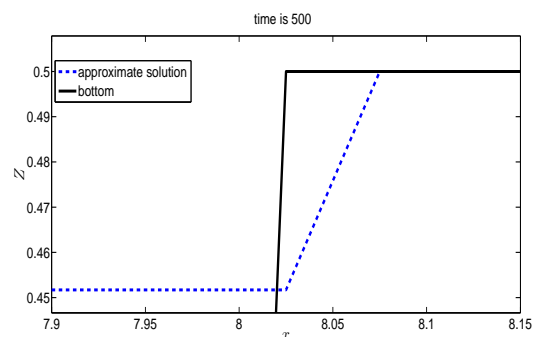


Figure 4.17: The simulated water surface produced by scheme I with $\Delta t = 0.001s$.



(a) The water surface, Z .



(b) The area where the water depth from scheme I is negative.

Figure 4.18: The simulated water surface produced by scheme I with smaller $\Delta t = 0.0005s$ at steady state.

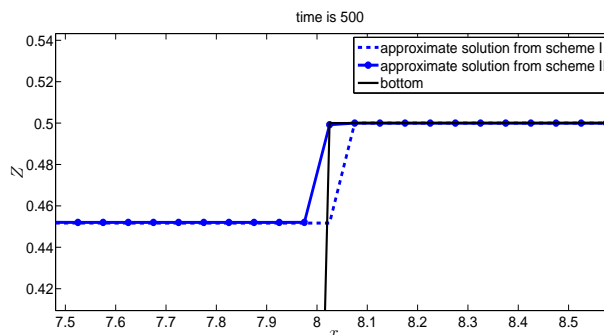


Figure 4.19: The comparison of the results from scheme I and II using $K = 500$ in area where the water depth from scheme I is negative.

4.3.6 Vacuum occurrence by a double rarefaction wave over a step

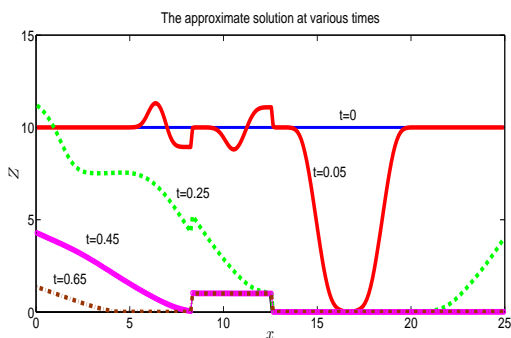
This experiment is motivated by the results from the FVM with VFRoe using a non-conservative variable (VFRoe-ncv) scheme given in [12] and from the FVM weighted essentially non-oscillatory (WENO) scheme given in [48], and to illustrate the ability of the scheme to handle wet/dry problems over a discontinuous bottom. The flow is considered on a 25 m long rectangular channel with discontinuous bottom defined by

$$z(x) = \begin{cases} 1, & \text{if } \frac{25}{3} \leq x \leq \frac{25}{2}, \\ 0, & \text{otherwise} \end{cases} \quad (4.30)$$

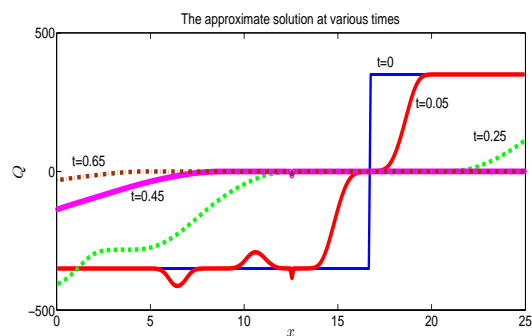
and frictionless. The initial water surface Z is 10 m and the initial discharge is

$$Q(x) = \begin{cases} -350, & \text{if } 0 \leq x < \frac{50}{3}, \\ 350, & \text{otherwise.} \end{cases} \quad (4.31)$$

The simulation is performed on 250 uniform grid cells with $\Delta t = 0.001s$ and the water surface and discharge are observed at $t = 0.05, 0.25, 0.45,$ and $0.65s$ (see Figure 4.20).



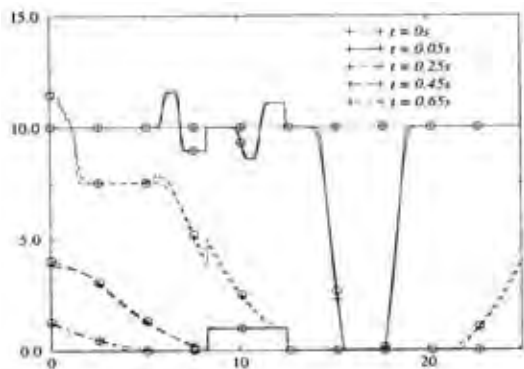
(a) The water surface, Z .



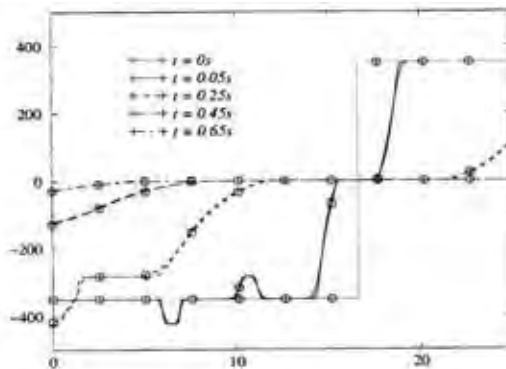
(b) The discharge, Q .

Figure 4.20: The approximate solution of the vacuum occurrence by a double rarefaction wave over a step at various times.

The simulation results show that dry areas develop after the water flows out of the domain as time passes. Figure 4.20 shows the numerical results for the water surface and the discharge at various times, which show good agreement with the results in [12, 48] (see Figure 4.21 for the result from [12]), illustrating that the numerical scheme works well for the wet/dry problem with a discontinuous bottom.



(a) The water surface, Z .



(b) The discharge, Q .

Figure 4.21: The result of the vacuum occurrence by a double rarefaction wave over a step at various times from [12].

4.3.7 Unsteady dam break flow in adverse slope channel

This numerical experiment is designed to compare results with the laboratory experiment by Aureli et al. [4]. The flow is considered on a 7 m long rectangular channel with the dam located at 2.25 m from the left boundary. The initial water depth is 0.292 m inside the dam and it is dry outside with zero initial velocity and Manning's roughness coefficient 0.025. The bottom elevation is

$$z(x) = \begin{cases} 0, & \text{if } 0 \leq x < 3.5, \\ 0.1(x - 3.5), & \text{if } 3.5 \leq x \leq 7 \end{cases} \quad (4.32)$$

and the simulation is performed for 30s by using $K = 700$ and $\Delta t = 0.001s$. The water depths are observed at four different locations in the channel at 1.4, 2.25, 3.4, and 4.5 m, as shown in Figure 4.22, which also shows the laboratory results from [4]. The numerical results are in good agreement with the laboratory measurements at various locations, showing the accuracy of the numerical scheme for flows with bottom slope and friction effects.

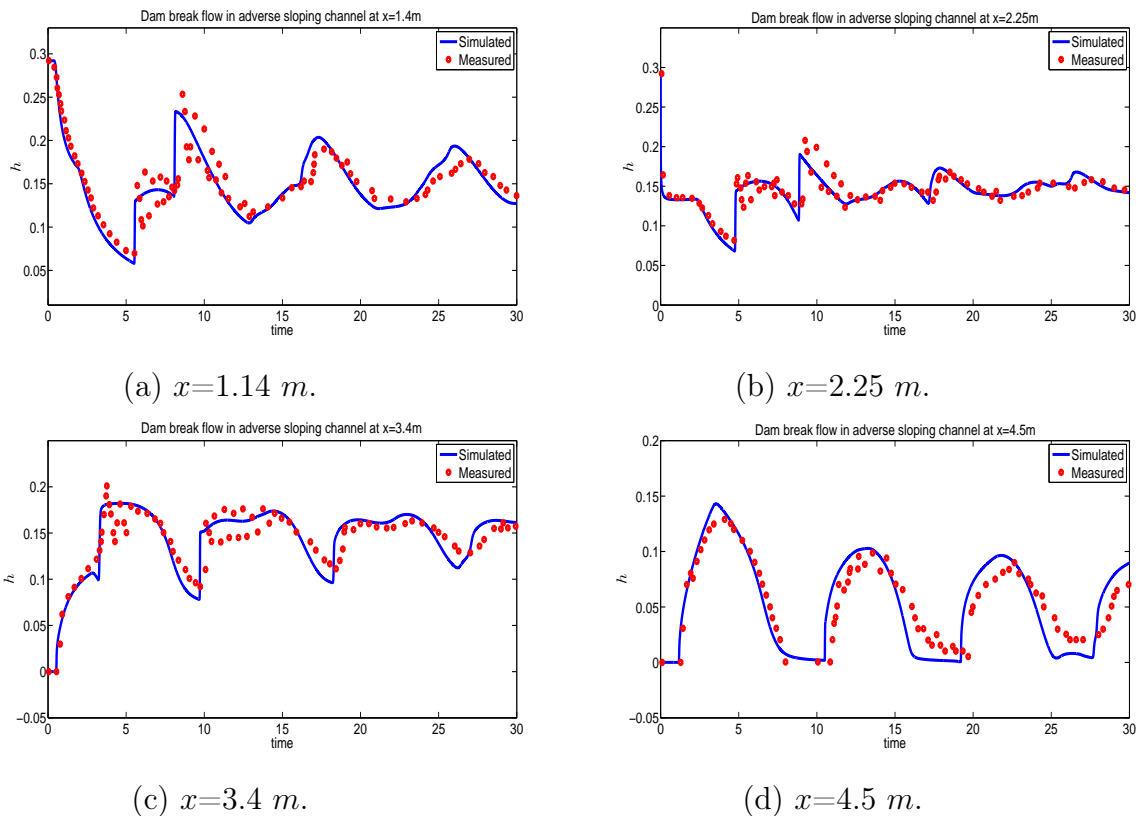


Figure 4.22: The comparisons between the simulated water depths and the laboratory results from [4] at various locations.

4.3.8 Simulation of the flow in the Yom river

In this experiment, the numerical scheme is applied to simulate water flow in the Yom river located at Phrae province in Northern of Thailand from the gauging stations Y20 to Y1C (see Figure 4.23). The data of the bottom elevation and the cross-sectional areas of the river are obtained from [16] and [53]. The simulation is performed using 45 different cross-sectional areas located along the river from Y20 to Y1C with $\Delta x = 2000\text{ m}$ approximately and with the bottom elevation data shown in Figure 4.24. The example of cross-sectional areas at Y20, Y1C and at point 1, 2, 3, and 4 in Figure 4.24 are shown in Figure 4.25 and 4.26.



Figure 4.23: The studied area of the Yom river from gauging stations Y20 to Y1C (blue line).

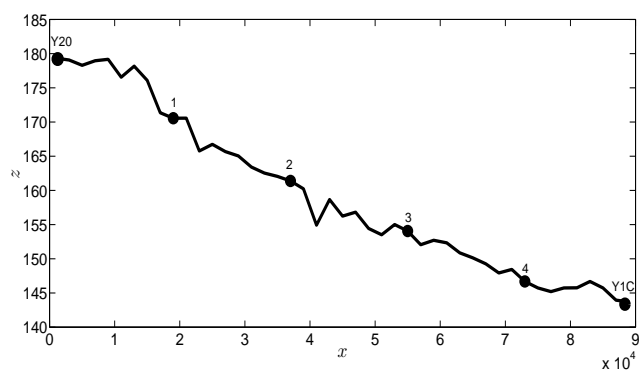
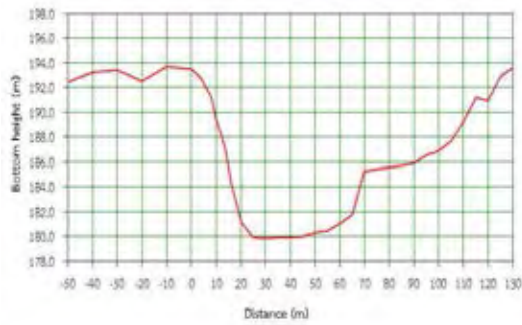
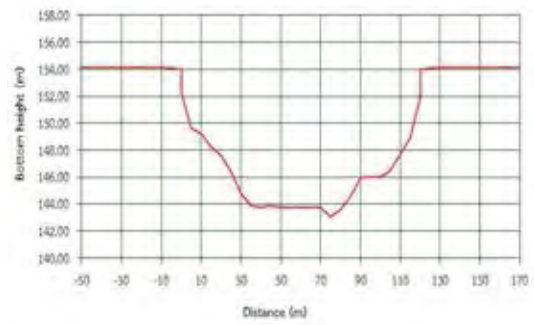


Figure 4.24: The bottom elevation of the Yom river from Y20 to Y1C.

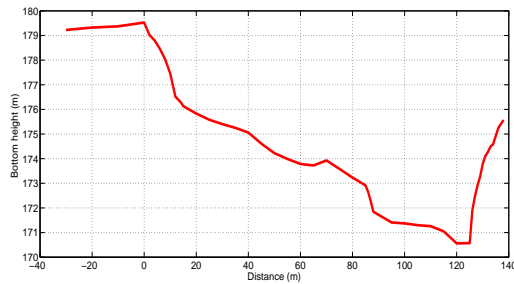


(a) Y20 gauging stations.

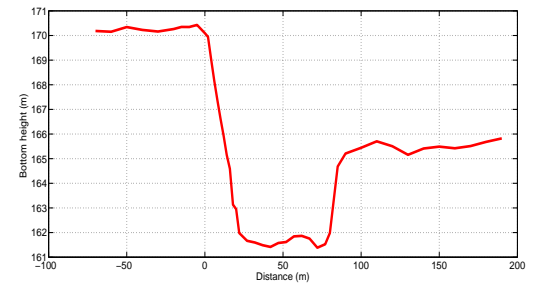


(b) Y1C gauging stations.

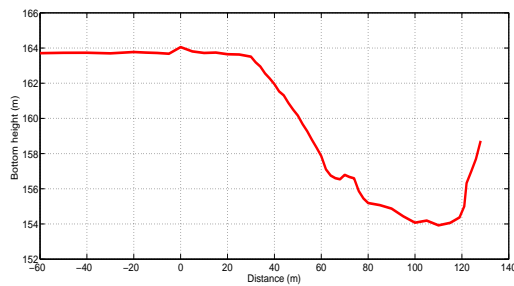
Figure 4.25: The cross-sectional areas of the gauging stations obtained from [53].



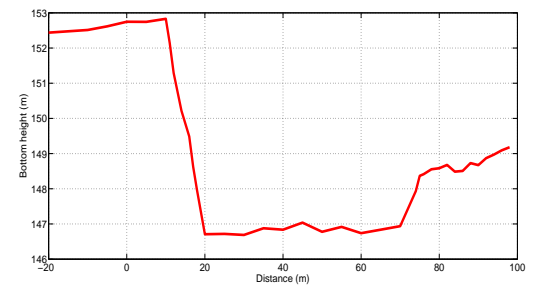
(a) Point 1 in Figure 4.24.



(b) Point 2 in Figure 4.24.



(c) Point 3 in Figure 4.24.

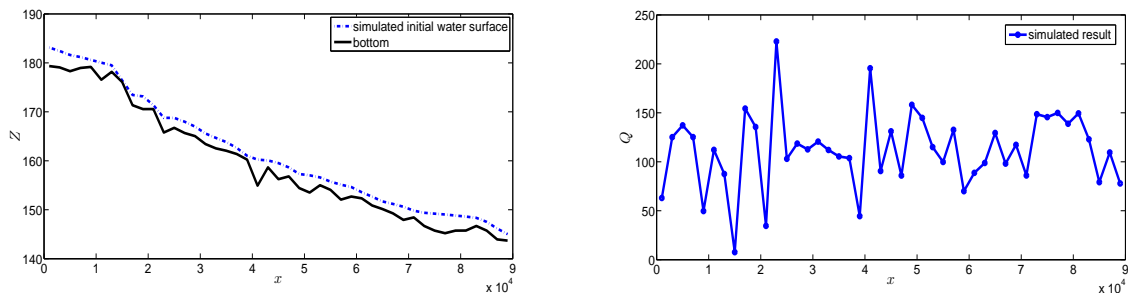


(d) Point 4 in Figure 4.24.

Figure 4.26: Examples of the cross-sectional areas at locations 1, 2, 3, and 4 in Figure 4.24 obtained from [16].

The simulation of water flow in Yom river from Y20 to Y1C is performed for two weeks, from August 27 to September 10, 2014. The initial data on August 27 is obtained by inputting the real data on August 26 for the water surface

$Z = 183.14$ and the discharge $Q = 63.68$, then calibrating until we obtain values of Z and Q that agree with the real data at Y1C on August 27. Figure 4.27 shows the obtained results. This calibration of initial data also gives the value of the Manning's roughness coefficient of $n=0.025$ for our simulation.

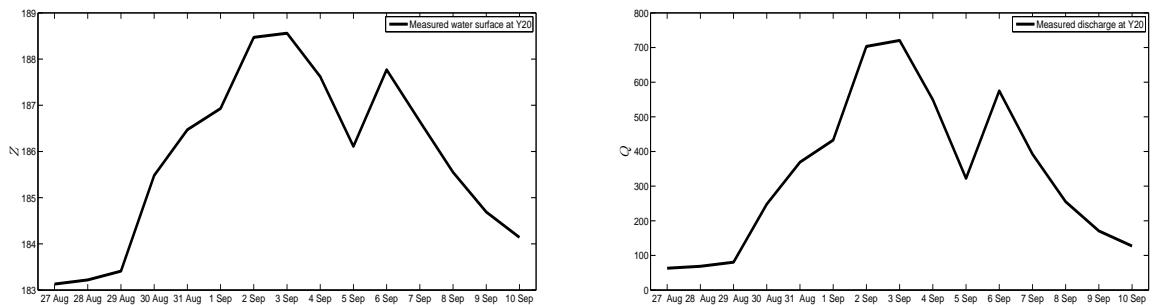


(a) The initial water depth from simulated result.

(b) The initial discharge from simulated result.

Figure 4.27: The numerical results for water depth and the discharge on August 27, 2014.

The water surface and discharge at Y20 from August 27 to September 10 used in the simulation are set to be the measured data from [53] (see Figure 4.28). The simulated discharge compared with the real data [53] from August 27 to September 10, 2014, at Y1C station is shown in Figure 4.29, showing that the simulated discharge has variations very similar to the real measured data. It has small variation from August 27 to 29, increasing rapidly from August 30 to September 4, decreasing rapidly from September 4 to 6, and oscillating similarly from September 6 to 10. The result from the simulation shows good agreement with the measured data in term of the discharge, which can capture the peaks of the discharge correctly. It also show the efficiency and accuracy of the developed scheme to handle the flow that cross-sectional and bottom have a lot of variation with friction effect. This illustrates that our numerical scheme is applicable for simulating real water flows in a river.



(a) The real measured water surface.

(b) The real measured discharge.

Figure 4.28: The real measured data for the water surface and the discharge from August 27 to September 10, 2014 at Y20 station.

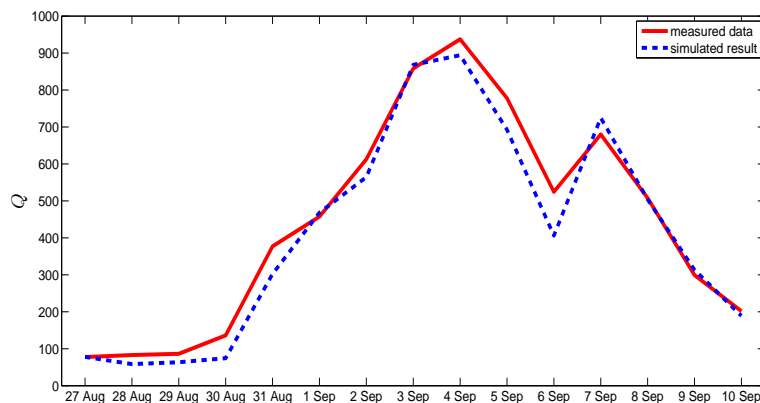


Figure 4.29: The comparison of the simulated discharge and the real measured data from August 27 to September 10, 2014 at Y1C station.

4.4 Conclusions

In this work, we have presented the reconstruction and bottom modification techniques to handle the shallow water equations for open channel flows in arbitrary cross-sectional areas for wet/dry problems. The scheme preserves the mass during time integration and it is also more efficient in term of stability when dealing with wet/dry problems. As seen in Section 4.3, the scheme is capable of handling many

flow situation and preserving the still water stationary state. In addition, the presented scheme is also applicable for simulating flows in the Yom river located at Phrae province as described in Section 4.3.8, where the simulated results capture the variation of the discharge very well when compared to the measured data of the real flow.

CHAPTER V

WELL-BALANCED FINITE VOLUME METHOD WITH WEIGHTED AVERAGE FLUX FOR TWO-DIMENSIONAL SHALLOW WATER EQUATIONS

A well-balanced FVM for solving two-dimensional SWE with WAF is developed in this work to simulate flooding. Friction source terms are estimated with a semi-implicit scheme resulting in an efficient numerical method for simulating shallow water flows over irregular domains, for both wet and dry beds. A wet/dry cell tracking technique is also presented for reducing computational time. The accuracy of these methods are investigated by applying to well-studied cases. For practical purposes, the developed scheme is applied to simulate the flooding of the Chao Phraya river from Chai Nat to Sing Buri provinces in Thailand during October 13-17, 2011. The numerical simulations yield results that agree with the existing data obtained from the satellite images.

5.1 Finite volume method (FVM) for two-dimensional shallow water equations

Consider the two-dimensional SWE

$$U_t + F(U)_x + G(U)_y = S(U), \quad (5.1)$$

where

$$U = \begin{pmatrix} h \\ hu \\ hv \end{pmatrix}, \quad F(U) = \begin{pmatrix} hu \\ hu^2 + \frac{1}{2}gh^2 \\ huv \end{pmatrix}, \quad G(U) = \begin{pmatrix} hv \\ huv \\ hv^2 + \frac{1}{2}gh^2 \end{pmatrix}, \quad (5.2)$$

and

$$S(U) = \begin{pmatrix} 0 \\ -ghz_x + S_{fx} \\ -ghz_y + S_{fy} \end{pmatrix}, \quad (5.3)$$

h is the water depth, g is a acceleration due to gravity, u and v are the flow velocities in the x - and y -directions, respectively, $S_{fx} = -Cu\sqrt{u^2 + v^2}$ and $S_{fy} = -Cv\sqrt{u^2 + v^2}$ are the friction terms in the x - and y -directions, respectively with $C = gn^2/h^{1/3}$ and n is a Manning's roughness coefficient.

The FVM in two-dimensions begin by dividing the computational domain in x - and y -direction into Kx and Ky cells, with uniform cell size $\Delta x = x_{i+1/2} - x_{i-1/2}$ and $\Delta y = y_{j+1/2} - y_{j-1/2}$ for $i = 1, 2, \dots, Kx$ and $j = 1, 2, \dots, Ky$. $x_{i-1/2}$ and $x_{i+1/2}$ are the left and the right interfaces of the cell in x -direction, and $y_{j-1/2}$ and $y_{j+1/2}$ are the left and the right interfaces of the cell in y -direction, respectively. We denote the ij^{th} cell by $I_{ij} = (x_{i-1/2}, x_{i+1/2}) \times (y_{j-1/2}, y_{j+1/2})$. The example of the grid discretization in two-dimensions is shown in Figure 5.1.

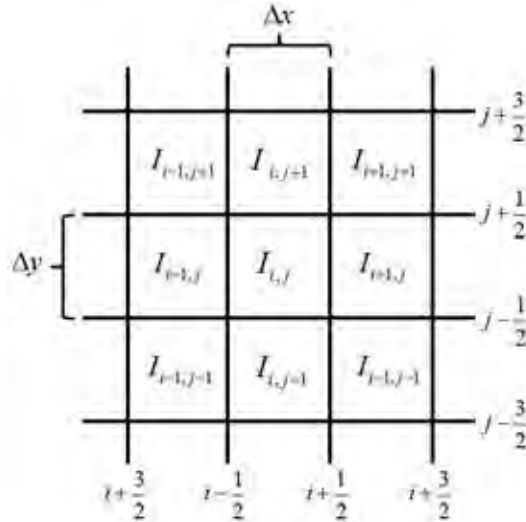


Figure 5.1: The grid discretization in two-dimensions.

A discretized form of (5.1) is

$$\frac{dU_{ij}(t)}{dt} + \frac{\widehat{F}_{i+1/2,j} - \widehat{F}_{i-1/2,j}}{\Delta x} + \frac{\widehat{G}_{i,j+1/2} - \widehat{G}_{i,j-1/2}}{\Delta y} = S_{ij}, \quad (5.4)$$

where U_{ij} is the approximation of U defined as the unknown average over cell I_{ij} , namely,

$$U_{ij} = \frac{1}{\Delta x \Delta y} \int_{I_{ij}} U(x, y, t) dx dy. \quad (5.5)$$

Here, S_{ij} is the approximation of the source term at cell I_{ij} , and \widehat{F} and \widehat{G} are numerical fluxes in the x - and y -directions, respectively.

To ensure second-order accuracy in time, the second-order Runge-Kutta (RK2) method is applied in our work. It is found in our simulations that this method allows us to use time step sizes larger than those when using the first-order method.

5.1.1 Weighted average flux (WAF) for two-dimensional shallow water equations

Let's first consider the approximation of numerical flux in the x -direction. The intercell flux with WAF at interface $(x_{i+1/2}, y_j)$ is denoted by $\widehat{F}_{i+1/2,j}^{WAF}$, which is defined as an integral average of $F(U)$ at the half-time step, namely,

$$\widehat{F}_{i+1/2,j}^{WAF} = \frac{1}{\Delta x} \frac{1}{\Delta y} \int_0^{\Delta y} \int_{-\frac{\Delta x}{2}}^{\frac{\Delta x}{2}} F \left(U_{i+1/2,j} \left(x, y, \frac{\Delta t}{2} \right) \right) dx dy, \quad (5.6)$$

where $U_{i+1/2,j}$ is the solution of the Riemann problem with piecewise constant data $U_{i+1/2,j}^-$, $U_{i+1/2,j}^+$, which are the solutions from the left and the right limits at the interface $i + 1/2$. The details of derivations of WAF can be found in [6, 40, 41, 42]. Moreover, the wave structure form of WAF can be written as

$$\widehat{F}_{i+1/2,j}^{WAF} = \sum_{k=1}^{N_c+1} \omega_k F_{i+1/2,j}^{(k)}, \quad (5.7)$$

where N_c is the number of waves in the solution of the Riemann problem and $F_{i+1/2,j}^{(k)}$ is the value of flux in the region k of the solution of the Riemann problem, see Figure 5.2.

The WAF with Harten-Lax-van Leer-Contact (HLLC) version in two-dimensions is proposed by [2, 28]. There are three flux components, where the first two components are estimated by the weighted average values from the HLLC Riemann solver,

$$\left(\widehat{F}_{i+\frac{1}{2},j}^{WAF}\right)_p = \sum_{k=1}^3 \omega_k \left(F_{i+\frac{1}{2},j}^{(k)}\right)_p, \quad (p = 1, 2), \quad (5.8)$$

while the third component is the weighted average value of WAF,

$$\left(\widehat{F}_{i+\frac{1}{2},j}^{WAF}\right)_3 = \left(\omega_{1*} v_{i+\frac{1}{2},j}^- + \omega_{2*} v_{i+\frac{1}{2},j}^+\right) \left(\widehat{F}_{i+\frac{1}{2},j}^{WAF}\right)_1, \quad (5.9)$$

where $\left(F_{i+\frac{1}{2},j}^{(1)}\right)_p = \left(F\left(U_{i+\frac{1}{2},j}^-\right)\right)_p$, $\left(F_{i+\frac{1}{2},j}^{(3)}\right)_p = \left(F\left(U_{i+\frac{1}{2},j}^+\right)\right)_p$. The flux in intermediate region $\left(F_{i+\frac{1}{2},j}^{(2)}\right)_p$ is approximated by the HLL, see [28]. The weighted values are $\omega_1 = \frac{1}{2}(1 + c_1)$, $\omega_2 = \frac{1}{2}(c_2 - c_1)$, $\omega_3 = \frac{1}{2}(1 - c_2)$, $\omega_{1*} = \frac{1}{2}(1 + c^*)$, and $\omega_{2*} = \frac{1}{2}(1 - c^*)$, where $c_1 = S_L \Delta t / \Delta x$, $c_2 = S_R \Delta t / \Delta x$, and $c^* = S^* \Delta t / \Delta x$. Here, S_L , S_R , and S^* are wave speeds in the left, the right, and the intermediate regions, respectively. Note that the flux for the first two components is calculated by using only the S_L and the S_R waves in the Riemann problem, while the flux for the third component is calculated by using only the S^* wave. The diagram for WAF corresponding to the Riemann problem is shown in Figure 5.2.

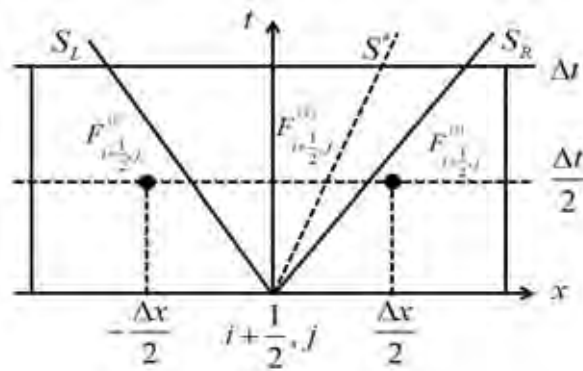


Figure 5.2: The diagram for WAF corresponding to the Riemann problem.

The wave speeds S_L and S_R for the wet bed case at the cell interface are approximated by

$$S_L = \min \left(u_{i+\frac{1}{2},j}^- - \sqrt{gh_{i+\frac{1}{2},j}^-}, u^* - \sqrt{gh^*} \right), \quad (5.10)$$

$$S_R = \min \left(u_{i+\frac{1}{2},j}^+ + \sqrt{gh_{i+\frac{1}{2},j}^+}, u^* + \sqrt{gh^*} \right), \quad (5.11)$$

with

$$\sqrt{gh^*} = \frac{1}{2} \left(\sqrt{gh_{i+\frac{1}{2},j}^-} + \sqrt{gh_{i+\frac{1}{2},j}^+} \right) - \frac{1}{4} \left(u_{i+\frac{1}{2},j}^+ - u_{i+\frac{1}{2},j}^- \right), \quad (5.12)$$

$$u^* = \frac{1}{2} \left(u_{i+\frac{1}{2},j}^- + u_{i+\frac{1}{2},j}^+ \right) + \sqrt{gh_{i+\frac{1}{2},j}^-} - \sqrt{gh_{i+\frac{1}{2},j}^+}. \quad (5.13)$$

For the dry bed on the right side of the cell interface, the wave speeds are approximated by

$$S_L = u_{i+\frac{1}{2},j}^- - \sqrt{gh_{i+\frac{1}{2},j}^-}, \quad S_R = u_{i+\frac{1}{2},j}^- + 2\sqrt{gh_{i+\frac{1}{2},j}^-} \quad (5.14)$$

and for the dry bed on the left side of the cell interface

$$S_L = u_{i+\frac{1}{2},j}^+ - 2\sqrt{gh_{i+\frac{1}{2},j}^+}, \quad S_R = u_{i+\frac{1}{2},j}^+ + \sqrt{gh_{i+\frac{1}{2},j}^+}. \quad (5.15)$$

The intermediate wave S^* was proposed by Toro in [41] which calculated by

$$S^* = \frac{S_L h_{i+\frac{1}{2},j}^+ \left(u_{i+\frac{1}{2},j}^+ - S_R \right) - S_R h_{i+\frac{1}{2},j}^- \left(u_{i+\frac{1}{2},j}^- - S_L \right)}{h_{i+\frac{1}{2},j}^+ \left(u_{i+\frac{1}{2},j}^+ - S_R \right) - h_{i+\frac{1}{2},j}^- \left(u_{i+\frac{1}{2},j}^- - S_L \right)}. \quad (5.16)$$

To avoid spurious oscillations near a shock front, the WAF method is modified by enforcing the TVD conditions [40, 41], which can be written as

$$\left(\widehat{F}_{i+\frac{1}{2},j}^{WAF-TVD} \right)_p = \sum_{k=1}^{N_c+1} \bar{\omega}_k \left(F_{i+\frac{1}{2},j}^{(k)} \right)_p, \quad (p = 1, 2) \quad (5.17)$$

and

$$\left(\widehat{F}_{i+\frac{1}{2},j}^{WAF-TVD} \right)_3 = \left(\bar{\omega}_{1*} v_{i+\frac{1}{2},j}^- + \bar{\omega}_{2*} v_{i+\frac{1}{2},j}^+ \right) \left(\widehat{F}_{i+\frac{1}{2},j}^{WAF-TVD} \right)_1, \quad (5.18)$$

where the new weights are

$$\begin{aligned}\bar{\omega}_1 &= \frac{1}{2} \left(1 + \operatorname{sgn}(c_1) \phi_{i+\frac{1}{2},j}^{(1)} \right), & \bar{\omega}_2 &= \frac{1}{2} \left(\operatorname{sgn}(c_2) \phi_{i+\frac{1}{2},j}^{(2)} - \operatorname{sgn}(c_1) \phi_{i+\frac{1}{2},j}^{(1)} \right), \\ \bar{\omega}_3 &= \frac{1}{2} \left(1 - \operatorname{sgn}(c_2) \phi_{i+\frac{1}{2},j}^{(2)} \right), & \bar{\omega}_{1*} &= \frac{1}{2} \left(1 + \operatorname{sgn}(c^*) \phi_{i+\frac{1}{2},j}^{(*)} \right), \text{ and} \\ \bar{\omega}_{2*} &= \frac{1}{2} \left(1 - \operatorname{sgn}(c^*) \phi_{i+\frac{1}{2},j}^{(*)} \right).\end{aligned}$$

Here, $\phi_{i+\frac{1}{2},j}^{(l)}$ are the WAF limiters, $l = 1, 2, *$, where the minmod function is employed in this work, namely,

$$\phi_{i+\frac{1}{2},j}^{(l)}(r^{(l)}) = \begin{cases} 1, & r^{(l)} \leq 0, \\ 1 - (1 - |c_l|) r^{(l)}, & 0 < r^{(l)} \leq 1, \\ |c_l|, & r^{(l)} > 1, \end{cases} \quad (5.19)$$

where $r^{(l)}$ is defined by

$$r^{(l)} = \begin{cases} \frac{\Delta h_{i-\frac{1}{2},j}^{(l)}}{\Delta h_{i+\frac{1}{2},j}^{(l)}}, = \frac{h_{i-\frac{1}{2},j}^{(l),+} - h_{i-\frac{1}{2},j}^{(l),-}}{h_{i+\frac{1}{2},j}^{(l),+} - h_{i+\frac{1}{2},j}^{(l),-}} & \text{if } c_l > 0, \\ \frac{\Delta h_{i+\frac{3}{2},j}^{(l)}}{\Delta h_{i+\frac{1}{2},j}^{(l)}} = \frac{h_{i+\frac{3}{2},j}^{(l),+} - h_{i+\frac{3}{2},j}^{(l),-}}{h_{i+\frac{1}{2},j}^{(l),+} - h_{i+\frac{1}{2},j}^{(l),-}}, & \text{if } c_l < 0 \end{cases} \quad (5.20)$$

with $\Delta h_{i-\frac{1}{2},j}^{(l)}$, $\Delta h_{i+\frac{1}{2},j}^{(l)}$, and $\Delta h_{i+\frac{3}{2},j}^{(l)}$ being the jumps of h across the wave l in the solutions $U_{i-\frac{1}{2},j}$, $U_{i+\frac{1}{2},j}$, and $U_{i+\frac{3}{2},j}$ of the Riemann problem, respectively. Similarly, the numerical flux in the y -direction, $\hat{G}_{i,j+\frac{1}{2}}$, is obtained via (5.17)-(5.18). This concept can be applied at the interfaces $i - 1/2, j$ and $i, j - 1/2$.

5.1.2 Linear reconstruction

Since approximating the solution by the cell average only gives first-order accuracy in space, second-order accuracy can be obtained by applying linear reconstruction [23, 25, 40]. For example, in the x -direction, the unknown variables are reconstructed as

$$U_{i-1/2,j}^+ = U_{ij} - \sigma_{ij}\Delta x, \quad (5.21)$$

$$U_{i+1/2,j}^- = U_{ij} + \sigma_{ij}\Delta x, \quad (5.22)$$

where σ_{ij} is a slope limiter. In this work, we applied the minmod slope limiter,

$$\sigma_{ij} = \text{minmod} \left(\frac{U_{i-1,j} - U_{i,j}}{\Delta x}, \frac{U_{i,j} - U_{i+1,j}}{\Delta x} \right), \quad (5.23)$$

where

$$\text{minmod}(a, b) = \begin{cases} a, & \text{if } |a| \leq |b| \text{ and } ab > 0, \\ b, & \text{if } |b| \leq |a| \text{ and } ab > 0, \\ 0, & \text{if } ab \leq 0. \end{cases} \quad (5.24)$$

Similarly, the linear reconstruction in the y -direction can be obtained as in (5.21)-(5.22).

5.2 Well-balanced scheme

A well-balanced scheme is designed for preserving the stationary solution at steady state. For the two-dimensional problem, the still water stationary solution is

$$v = 0, \quad u = 0, \quad \text{and} \quad h + z = \text{constant}. \quad (5.25)$$

In this work, the well-balanced scheme is obtained following the pioneering work by Audusse [3]. We reconstruct h at the interfaces in the x - and y -directions by

$$h_{i+1/2,j}^{\pm,*} = \max \left(0, h_{i+1/2,j}^{\pm} + z_{i+1/2,j}^{\pm} - z_{i+\frac{1}{2},j} \right), \quad (5.26)$$

$$h_{i,j+1/2}^{\pm,*} = \max \left(0, h_{i,j+1/2}^{\pm} + z_{i,j+1/2}^{\pm} - z_{i,j+\frac{1}{2}} \right), \quad (5.27)$$

where $z_{i+\frac{1}{2},j} = \max \left(z_{i+1/2,j}^-, z_{i+1/2,j}^+ \right)$ and $z_{i,j+\frac{1}{2}} = \max \left(z_{i,j+1/2}^-, z_{i,j+1/2}^+ \right)$.

These reconstructions ensure non-negativity of the water depth, [3].

In this work, we have modified the conservative variables [3], to be

$$U_{i\pm 1/2,j}^{+,*} = \left(h_{i\pm 1/2,j}^{+,*}, h_{i\pm 1/2,j}^{+,*} u_{i\pm 1/2,j}^+, h_{i\pm 1/2,j}^{+,*} v_{i\pm 1/2,j}^+ \right)^T$$

and

$$U_{i,j\pm 1/2}^{+,*} = \left(h_{i,j\pm 1/2}^{+,*}, h_{i,j\pm 1/2}^{+,*} u_{i,j\pm 1/2}^+, h_{i,j\pm 1/2}^{+,*} v_{i,j\pm 1/2}^+ \right)^T.$$

The finite volume scheme becomes a well-balanced scheme and is expressed by

$$\frac{dU_{ij}(t)}{dt} + \frac{\widehat{F}_{i+1/2,j}^l - \widehat{F}_{i-1/2,j}^r}{\Delta x} + \frac{\widehat{G}_{i,j+1/2}^l - \widehat{G}_{i,j-1/2}^r}{\Delta y} = Sc_{i,j}, \quad (5.28)$$

where the numerical flux in the x -direction and the bottom slope terms are modified as

$$\widehat{F}_{i-\frac{1}{2},j}^r = \widehat{F} \left(U_{i-\frac{1}{2},j}^{-,*}, U_{i-\frac{1}{2},j}^{+,*} \right) + \frac{g}{2} \begin{pmatrix} 0 \\ \left(h_{i-\frac{1}{2},j}^+ \right)^2 - \left(h_{i-\frac{1}{2},j}^{+,*} \right)^2 \\ 0 \end{pmatrix}, \quad (5.29)$$

$$\widehat{F}_{i+\frac{1}{2},j}^l = \widehat{F} \left(U_{i+\frac{1}{2},j}^{-,*}, U_{i+\frac{1}{2},j}^{+,*} \right) + \frac{g}{2} \begin{pmatrix} 0 \\ \left(h_{i+\frac{1}{2},j}^- \right)^2 - \left(h_{i+\frac{1}{2},j}^{-,*} \right)^2 \\ 0 \end{pmatrix}, \quad (5.30)$$

and

$$Sc_{i,j} = \begin{pmatrix} 0 \\ -\frac{g}{2\Delta x} \left(h_{i-\frac{1}{2},j}^+ + h_{i+\frac{1}{2},j}^- \right) \left(z_{i+\frac{1}{2},j}^- - z_{i-\frac{1}{2},j}^+ \right) \\ -\frac{g}{2\Delta y} \left(h_{i,j-\frac{1}{2}}^+ + h_{i,j+\frac{1}{2}}^- \right) \left(z_{i,j+\frac{1}{2}}^- - z_{i,j-\frac{1}{2}}^+ \right) \end{pmatrix}. \quad (5.31)$$

The linear reconstruction of the bottom elevation z in $Sc_{i,j}$ is obtained from the linear reconstruction of $h + z$ minus the linear reconstruction of h , as suggested in [3], for example, $z_{i,j+\frac{1}{2}}^- = (h + z)_{i,j+\frac{1}{2}}^- - h_{i,j+\frac{1}{2}}^-$. When the linear reconstruction is not applied, $Sc_{i,j}$ is zero, which is equivalent to the first-order method.

Similarly, the numerical flux in the y -direction, \widehat{G}^r and \widehat{G}^l can be obtained by the decomposition of the bottom slopes in the third component.

Note that the present scheme with WAF is second-order accurate in space for smooth flow solution when applying the linear reconstruction, which does not depend on the choices of the numerical fluxes, see proof in [3].

5.3 Friction term approximations

To obtain a stable FVM when dealing with a strong nonlinear friction term, we use an implicit scheme to approximate the friction. Following the splitting implicit technique presented in [17, 18], we solve the SWE by considering the ordinary differential equation

$$\frac{dU_{ij}}{dt} = (S_f)_{ij}^{n+1}. \quad (5.32)$$

In the x -direction, we have

$$\frac{d(hu)_{ij}}{dt} = (S_{fx})_{ij}^{n+1} \quad (5.33)$$

which can be approximated by

$$\frac{(hu)_{ij}^{n+1} - (hu)_{ij}^n}{\Delta t} = (S_{fx})_{ij}^n + \frac{\partial (S_{fx})_{ij}^n}{\partial (hu)} \left((hu)_{ij}^{n+1} - (hu)_{ij}^n \right). \quad (5.34)$$

This can be rewritten as

$$(hu)_{ij}^{n+1} = (hu)_{ij}^n + \Delta t \frac{(S_{fx})_{ij}^n}{(D_x)_{ij}^n}, \quad (5.35)$$

where D_x is an implicit coefficient defined by

$$(D_x)_{ij}^n = 1 + \Delta t C_{ij}^n \frac{2 \left((hu)_{ij}^n \right)^2 + \left((hv)_{ij}^n \right)^2}{(h_{ij}^n)^2 \sqrt{\left((hu)_{ij}^n \right)^2 + \left((hv)_{ij}^n \right)^2}} \quad (5.36)$$

with $C_{ij}^n = gn^2 / (h_{ij}^n)^{1/3}$. Note that although this scheme is called implicit, see (5.32), we can calculate it explicitly, see (5.35). The updated solutions are calculated twice for each step of the second-order Runge-Kutta method. The calculation in the y -direction are considered similarly. Since the well-balanced scheme that we

apply here has preserved the non-negativity of water depth, see [3], it implies that our numerical scheme with this friction term approximation also preserves the non-negativity of water depth, because the RHS in the conservation of mass equation is zero.

5.4 Wet/dry tracking technique

The wet/dry tracking technique is employed in order to reduce the computational time of the FVM. The key idea is to track only the updated cells, and then perform calculation only on these cells. To do this, we present the wet/dry tracking algorithm in Figure 5.3 as follows

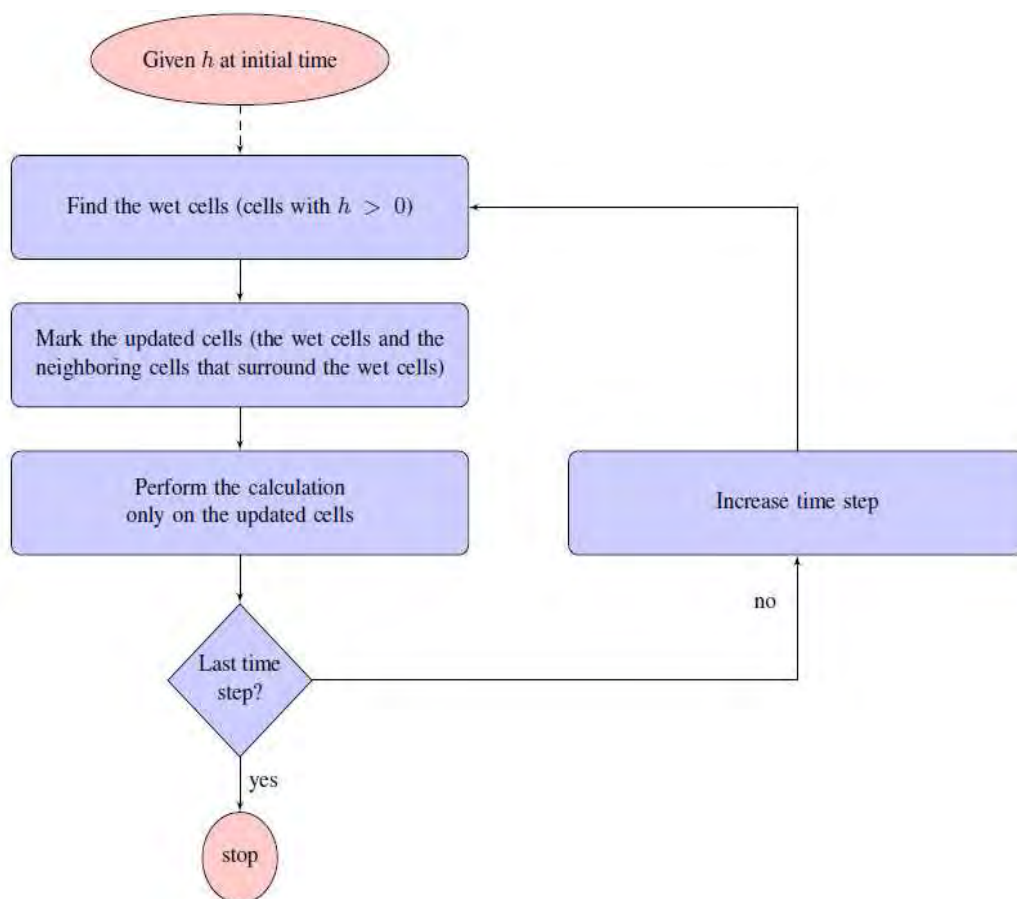


Figure 5.3: Flowchart of the wet/dry tracking algorithm.

The example of finding updated cells from the first to the second time step is illustrated in Figure 5.4, where the wet cells are marked as crossed cells and the neighboring cells are marked with black. The updated cells are the combination of the wet cells and their neighboring cells.

By applying the wet/dry tracking algorithm, we can greatly reduce the computational time for flow problems that have smaller wetted area, when compared with the whole domain. Note that this algorithm is easy to implement in general, since it will slightly enlarge the computational domain at each time step by adding a few new neighboring cells to the domain without deleting cells that change from wet to dry.

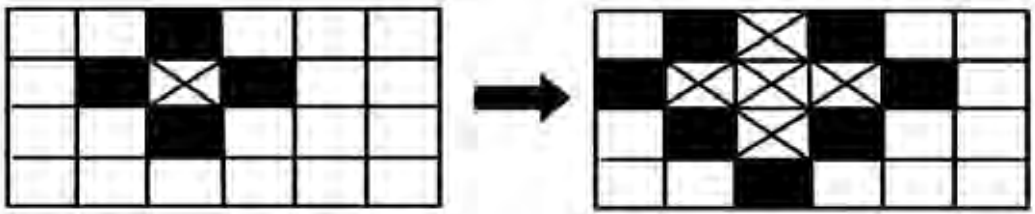


Figure 5.4: The change of the wet cells (cross) and the added neighboring cells (black) from first time step (left) to the second time step (right).

5.5 Numerical results

In this section, we describe the numerical experiments for various test cases used to check the accuracy of our scheme. For practical purposes, the developed numerical scheme is applied to simulate the great flood in Thailand, 2011. The numerical experiments in Sections 5.5.1-5.5.8 are performed by the developed scheme using linear reconstruction. To save computational time for flood problem simulation, we apply the numerical scheme without linear reconstruction in Section 5.5.9.

5.5.1 Rectangular dam break without friction

In this experiment, we consider the rectangular dam break flow without friction in one-dimension. The numerical results are compared with the analytical solutions

to check the accuracy of the scheme. The accuracy is checked for results of the two different numerical fluxes, HLL and WAF, and for both wet and dry beds. We compare the errors of the results for the schemes with and without the linear reconstruction to check the accuracy of the solutions.

Wet bed

We consider the dam break flow in the domain $-5 \leq x \leq 5$ with initial condition

$$h(x, t) = \begin{cases} 1, & \text{if } x \leq 0, \\ 0.6, & \text{if } x > 0, \end{cases} \quad (5.37)$$

and zero initial velocity, and with transmissive boundary conditions. We perform 50, 100, and 200 uniform grid cells to investigate the errors. The final time is set at $2s$ with time step $\Delta t = 0.005s$. The mean absolute errors (MAE) and the root mean squared errors (RMSE) of the water depth h obtained from the HLL and the WAF methods are shown in Table 5.1.

Scheme without the linear reconstruction						
	$K = 50$		$K = 100$		$K = 200$	
	MAE	RMSE	MAE	RMSE	MAE	RMSE
HLL	0.0163	0.0280	0.0108	0.0215	0.0069	0.0165
WAF	0.0083	0.0182	0.0047	0.0127	0.0027	0.0093
Scheme with the linear reconstruction						
	$K = 50$		$K = 100$		$K = 200$	
	MAE	RMSE	MAE	RMSE	MAE	RMSE
HLL	0.0078	0.0178	0.0043	0.0120	0.0023	0.0085
WAF	0.0053	0.0145	0.0028	0.0096	0.0015	0.0069

Table 5.1: The MAE and the RMSE for wet bed case.

The result from Table 5.1 shows that the MAE and the RMSE obtained from

the WAF are less than those from the HLL for the scheme with and without the linear reconstruction. In this case, the second-order accuracy of the approximate solution is not obtained even though the scheme is applied with the linear reconstruction because the solution is not smooth. However, we observe that the result from the WAF scheme without the linear reconstruction is comparable to the HLL with the linear reconstruction. This shows that the modified scheme with the WAF is more accurate than that with HLL.

Dry bed

The dry bed experiment is performed on the same model problem as for the wet bed, except with a different initial condition

$$h(x, 0) = \begin{cases} 1 & , \text{ if } x \leq 0, \\ 0 & , \text{ if } x > 0. \end{cases} \quad (5.38)$$

Scheme without the linear reconstruction						
	$K = 50$		$K = 100$		$K = 200$	
	MAE	RMSE	MAE	RMSE	MAE	RMSE
HLL	0.0164	0.0265	0.0113	0.0187	0.0077	0.0130
WAF	0.0081	0.0117	0.0048	0.0075	0.0029	0.0050
Scheme with the linear reconstruction						
	$K = 50$		$K = 100$		$K = 200$	
	MAE	RMSE	MAE	RMSE	MAE	RMSE
HLL	0.0100	0.0142	0.0052	0.0082	0.0026	0.0045
WAF	0.0061	0.0091	0.0030	0.0049	0.0015	0.0026

Table 5.2: The MAE and the RMSE for dry bed case.

Table 5.2 shows the errors of the water depth h for 50, 100, and 200 cells from the WAF and HLL. Again, we observe that the result does not have second-order

accuracy, but the result from WAF without the linear reconstruction is comparable to the HLL with the linear reconstruction. This shows that the modified well-balanced scheme with the WAF is more accurate than that with the HLL.

5.5.2 2D circular dam break

This numerical experiment is performed to check the accuracy of the developed scheme for a two-dimensional problem without source term. We consider a circular dam break flow in the domain $200 \text{ m} \times 200 \text{ m}$ with flat and frictionless bottom. The initial condition is a circular dam with 50 m radius, located at the center of the domain as shown in Figure 5.5. The experiments are performed on both wet and dry beds.

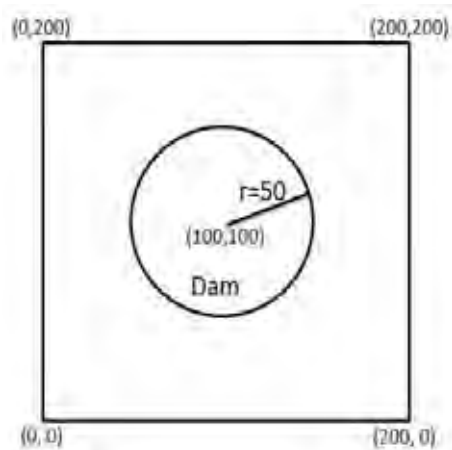


Figure 5.5: The domain of 2D circular dam break flow.

Circular dam break on wet bed

In this case, the initial water depths are set at 10 m inside the circular dam and 1 m outside the dam, and with zero initial velocity. The number of grid cells are 85×85 cells and the simulation time is $t = 3 \text{ s}$.

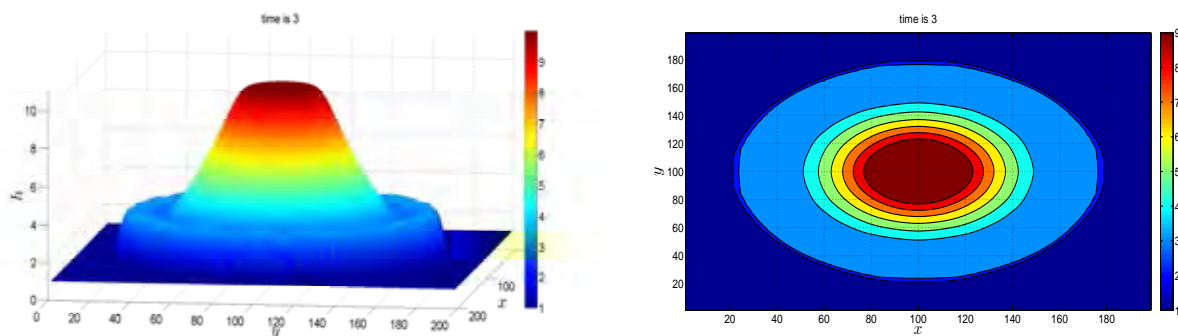


Figure 5.6: Water surface in 3D plot (left) and its contour plot (right) for wet bed at $t = 3s$.

The circular dam wall is assumed to be removed completely and instantly at the time of dam failure, thus, the wave front propagates outward from the center of the domain. The water surface profile and its contour plot are shown in Figure 5.6, on the left and the right of the figure, respectively, which agree very well with the results from [18].

Circular dam break on dry bed

In this case, the water depths are set at 10 m inside the circular dam and zero outside the dam. The surface profile and its contour plot at $t = 3s$ are shown in Figure 5.7. Again, the numerical results agree very well with the results reported in [18]. These numerical investigations for both wet and dry beds show the validity and accuracy of the developed scheme, as compared with [18].

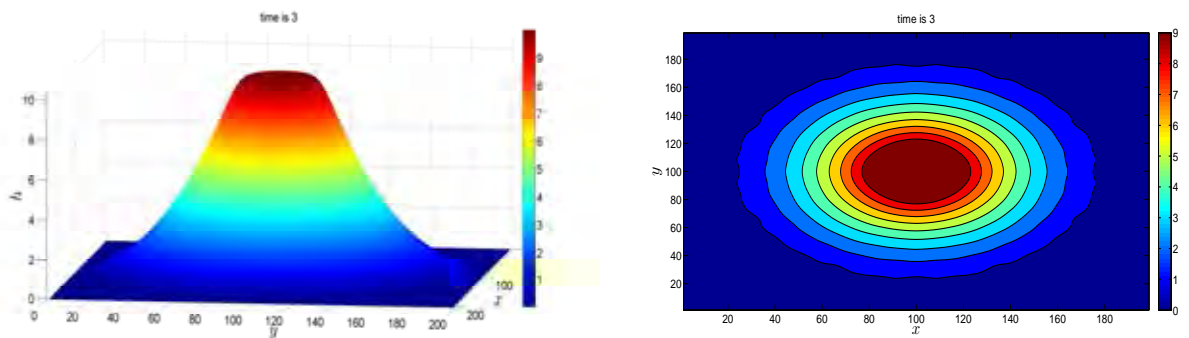


Figure 5.7: Water surface in 3D plot (left) and its contour plot (right) for dry bed at $t = 3s$.

In addition, the scheme with the wet/dry tracking technique reduces the computational time from $37.61s$ to $25.15s$, when compared with the scheme without this technique.

5.5.3 Partial dam break

This experiment is considered on a $200\text{ m} \times 200\text{ m}$ rectangular domain. The initial water level is set at 10 m on the upstream side and zero on the downstream side. The bottom is assumed to be flat and frictionless. The partial dam break is set at middle of the domain, as shown in Figure 5.8.

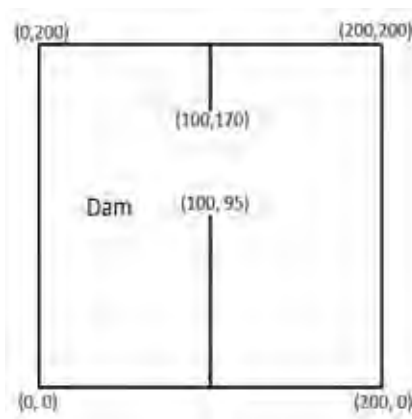


Figure 5.8: Domain of the partial dam break problem.

The simulation is performed on 85×85 uniform grid cells and with final time

7.2s. The surface profile and its contour plot at $t = 7.2s$ are shown in Figure 5.9. The obtained simulation results agree closely with results in [1, 46].

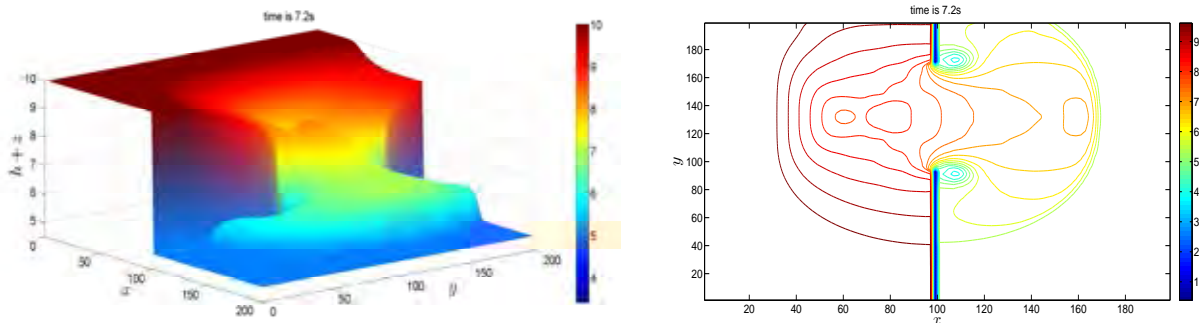


Figure 5.9: Water surface plot (left) and contour plot (right) of the partial dam break problem.

5.5.4 Rectangular dam break with friction

In this experiment, we consider a rectangular dam break on the domain with 1000 m long and 100 m wide, with friction on flat bottom. The wall of the dam is located at $x = 500$ m. The water height at initial time is 1 m inside the dam ($x \leq 500$ m) and zero outside the dam ($x > 500$ m), and with zero initial velocity. For the friction, the Manning's roughness coefficient is $n = 0.02 \text{ m}^{-1/3} \text{ s}$. The simulation is performed on 200×20 uniform grid cells with $\Delta t = 0.5 \text{ s}$ and the final time 64 s .

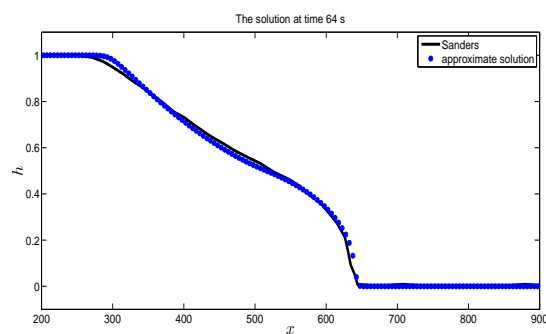


Figure 5.10: The comparison of our numerical results with the results from [34].

The comparison of cross-sections along the flow direction between the numerical results and the results from [34] is shown in Figure 5.10. The comparison shows

that the numerical results obtained from the developed scheme is as accurate as the results from [34], in the case of shallow-water flows with friction effect.

5.5.5 Well-balanced test in two-dimensions

This experiment is performed to check the exact C-property of the present scheme. To satisfy the exact C-property, the numerical solution should approach the still water stationary solution at steady state, [31], i.e., having zero errors. In this experiment, we consider a rectangular domain $[0, 1] \times [0, 1]$ with the bottom function defined by

$$z(x, y) = 0.8e^{-50((x-0.5)^2+(y-0.5)^2)}. \quad (5.39)$$

The initial water height is $h(x, y) = 1 - z(x, y)$ with zero initial discharges $hu(x, y) = 0$ and $hv(x, y) = 0$.

The simulation is run on 50×50 uniform cells for very large final time, in this case we use $t = 100s$. The RMS errors for h , hu , and hv are 2.0974×10^{-16} , 7.7270×10^{-14} , and 8.5070×10^{-14} , respectively. The observed errors are approximately the round-off errors of the machine, which implies that the obtained numerical solution is exact. This shows that the developed scheme satisfies the exact C-property. Figure 5.11 shows the water profile of the still water at $t = 100s$.

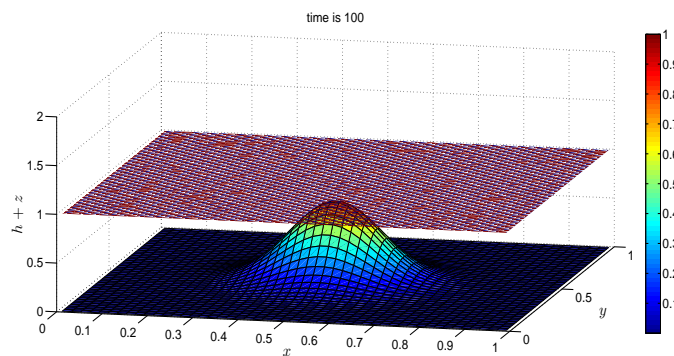


Figure 5.11: Water surface profile for very large time.

5.5.6 Subcritical flows over a bump

This experiment illustrates the second-order accuracy of the developed scheme for the smooth flow with the bottom slope source term. We consider a subcritical shallow water flow over a bump in one-dimension. The rectangular channel is 25 m long. The bump elevation is defined by

$$z(x) = \begin{cases} 0.2 - 0.05(x - 10)^2, & \text{if } 8 < x < 12, \\ 0, & \text{otherwise.} \end{cases} \quad (5.40)$$

The upstream boundary is imposed by $hu = 4.42 \text{ m}^2/\text{s}$ and the downstream boundary is set in term of water surface, $h = 2 \text{ m}$. The initial water depth in the domain is $h + z = 2 \text{ m}$ with zero initial discharge and the time step is $\Delta t = 0.01 \text{ s}$. The approximate solution compared with the analytical solution from the WAF with the linear reconstruction scheme is displayed in Figure 5.12. The numerical accuracy is measured in terms of MAE and RMSE, when compared with existing analytical solutions. Again, we compare the error of the results when the scheme is performed with and without the linear reconstruction to check the accuracy of the solutions. In addition, the accuracy is compared between the two numerical fluxes, HLL and WAF. The comparison of errors in Table 5.3 and Table 5.4 shows that the developed scheme with WAF is more accurate than that with HLL, for the case of flow with bottom source term.

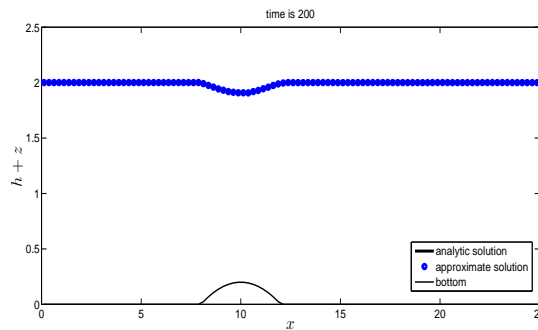


Figure 5.12: Subcritical flows over a bump from WAF with the linear reconstruction scheme when $K = 100$.

Scheme without the linear reconstruction				
	$K = 25$	$K = 50$	$K = 100$	order
	RMSE	RMSE	RMSE	RMSE
HLL	1.85×10^{-2}	1.03×10^{-2}	5.40×10^{-3}	0.89
WAF	1.46×10^{-2}	5.60×10^{-3}	2.70×10^{-3}	1.22
Scheme with the linear reconstruction				
	$K = 25$	$K = 50$	$K = 100$	order
	RMSE	RMSE	RMSE	RMSE
HLL	1.35×10^{-2}	3.70×10^{-3}	1.00×10^{-3}	1.88
WAF	1.22×10^{-2}	3.00×10^{-3}	7.44×10^{-4}	2.02

Table 5.3: The RMSE errors for subcritical flows over a bump.

Scheme without the linear reconstruction				
	$K = 25$	$K = 50$	$K = 100$	order
	MAE	MAE	MAE	MAE
HLL	1.01×10^{-2}	5.60×10^{-3}	2.90×10^{-3}	0.90
WAF	6.80×10^{-3}	2.60×10^{-3}	1.20×10^{-3}	1.25
Scheme with the linear reconstruction				
	$K = 25$	$K = 50$	$K = 100$	order
	MAE	MAE	MAE	MAE
HLL	6.90×10^{-3}	1.80×10^{-3}	4.79×10^{-4}	1.92
WAF	5.40×10^{-3}	1.20×10^{-3}	2.89×10^{-4}	2.11

Table 5.4: The MAE errors for subcritical flows over a bump.

The numerical results in Tables 5.3 and 5.4 also show that the numerical scheme without the linear reconstruction are not second-order accurate in space for smooth flow problem as discussed recently in Section 10.6 by Ata et al. [2]. To obtain a higher order approximation in space, we apply the linear reconstruction (5.21)-(5.24) to HLL and WAF schemes. The order of convergence is second-order measured by the MAE and RMSE errors.

5.5.7 Dam break flows over a trapezoidal bump

In this section, we run a numerical experiment of a dam break flow over a trapezoidal bump, and compare with the real experiment presented by Ozmen-Cagatay and Kocaman [32]. The flow is considered on a rectangular domain of 8.9 m long with the wall of the dam located at 4.65 m from the channel entrance, and the trapezoidal bump with 0.075 m high and 1 m base length at 1.53 m from the wall of the dam, see Figure 5.13. The reservoir is on the upstream side with 0.25 m of water, while the downstream side is dry and with zero initial velocity.

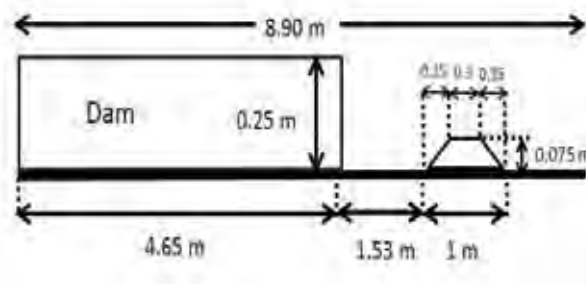


Figure 5.13: Initial setup of dam break flows over a trapezoidal bump.

The simulation is performed on 200 uniform cells with time step $\Delta t = 0.01s$. To compare the numerical results with the experimental data, we set h_0 and $\sqrt{g/h_0}$ as the length scale and time scale, respectively. The dimensionless time is $T = t\sqrt{g/h_0}$. The comparisons at snapshot of times $T = 11.9, 17.54, 20.67, 23.05, 29.69,$ and 41.84 are shown in Figure 5.14, showing that the numerical results agree closely with the experimental data at various times.

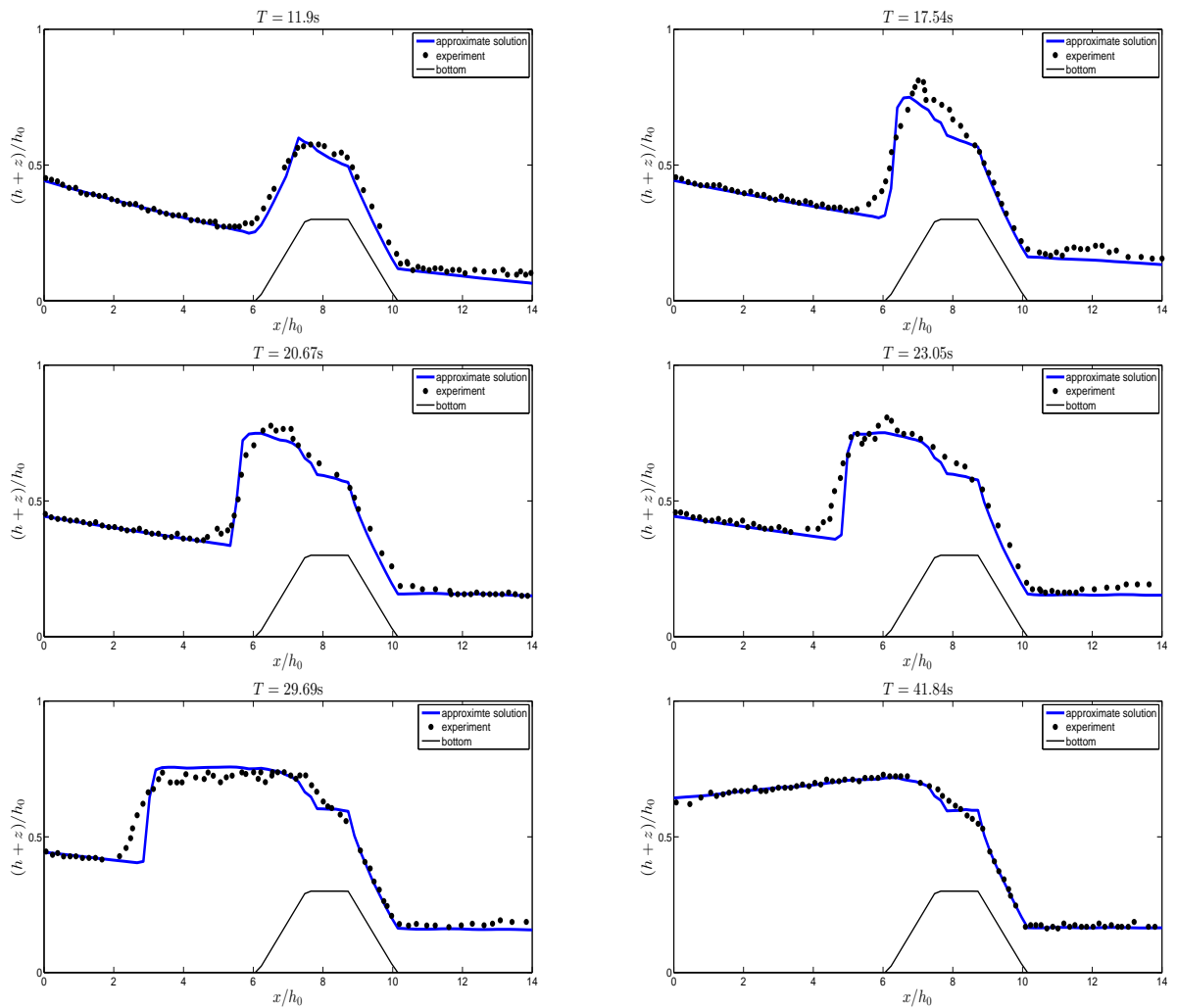


Figure 5.14: The comparisons between numerical results and experimental data from [32] for dam break flows over a trapezoidal bump for various $T = 11.9, 17.54, 20.67, 23.05, 29.69,$ and 41.84 .

5.5.8 Dam break flows over three humps

In this experiment, we consider the dam break flows over three humps defined by

$$\begin{aligned}
z(x, y) = \max \left\{ 0, 1 - \frac{1}{8} \sqrt{(x - 30)^2 + (y - 6)^2}, \right. \\
\left. 1 - \frac{1}{8} \sqrt{(x - 30)^2 + (y - 24)^2}, \right. \\
\left. 3 - \frac{3}{10} \sqrt{(x - 47.5)^2 + (y - 15)^2} \right\},
\end{aligned} \tag{5.41}$$

on 75 m x 30 m rectangular domain. The dam is located at 16 m from the upstream boundary with initial water depth $h + z = 1.875$ m and with zero depth on downstream boundary. The simulation is performed on 85×85 uniform grid cells with the Manning coefficient 0.018. The water depth profile and its contour plot at $t = 12$ s are shown in Figure 5.15. The obtained result agree closely with the previous results presented by [18, 27]. This experiment has illustrated the ability of the developed scheme for solving flows over dry bed with friction. As shown in the Figure 5.15, the strong shock front that attacks the largest hump is detected correctly. This demonstrates that the developed scheme is capable of simulating flows that have both wet and dry beds, as well as the effect from a large bottom slope. We have also found that the splitting implicit scheme enables us to use larger time step size when comparing with direct calculation.

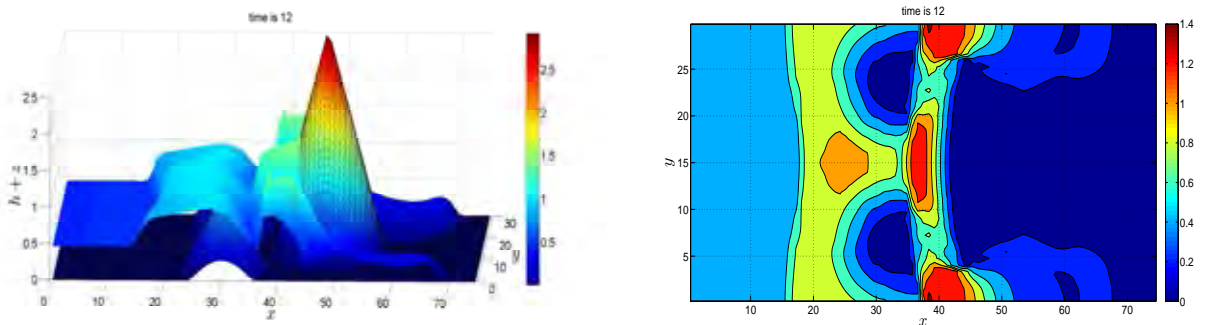


Figure 5.15: The water surface profile (left) and contour plot (right) of a dam break flows over three humps at $t = 12$ s.

When simulating wet/dry flow interactions, numerical schemes can result in non-conserved water mass. We have checked this by setting an initial mass in our

simulation as 893.3824. After running to 100 simulation time, the water mass is remains as 893.3824. This demonstration is numerical evidence that our scheme can preserve mass during time integration. The result is shown in Figure 5.16.

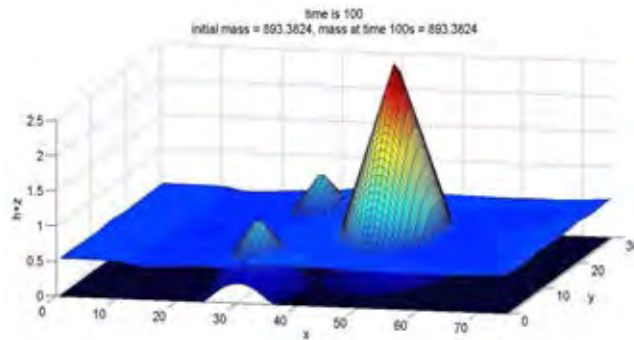


Figure 5.16: Water surface profile of a dam break flows over three humps at $t = 100s$.

5.5.9 Flood simulation in Thailand, 2011

The Chao Phraya river, Thailand, consists of several basins such as Ping, Wang, Yom, Nan, Sakae Krang, Pa Sak, Tha Chin, and finally the Chao Phraya basin itself. The lower part of this river goes through a region that is both the most populous and of significant economic interest to Thailand. Occasional flooding of this region has had deleterious impact on the country. In this experiment, we apply the developed scheme to simulate the great flood near the Chao Phraya river in 2011. We check the performance of the simulation by comparing the results with the real flood flow determined from the satellite images. The studied area is from the latitude $15.000000^{\circ}\text{N}$ to $15.190800^{\circ}\text{N}$ and from the longitude $100.165800^{\circ}\text{E}$ to $100.340800^{\circ}\text{E}$, known as the Chao Phraya river basin, from Chai Nat to Sing Buri provinces (see Figure 5.17), with the gauging stations located at c13 in Chai Nat province and c44 in Sing Buri province. The topography in this area is generally low land next to the Chao Phraya river. The bottom elevation is obtained from the NASA Shuttle Radar Topographic Mission (SRTM) in digital elevation data (DEM) format with resolution 90×90 m [55], while the Manning coefficient is assumed to be 0.03. In this simulation, we have adjusted DEM in the Chao Phraya

river to be lower approximately 10 meters from the original SRTM format [55]. This error can be measured from the measurement of water depth at c13 and c44 stations [54], while the DEM on the land area remains unchanged.

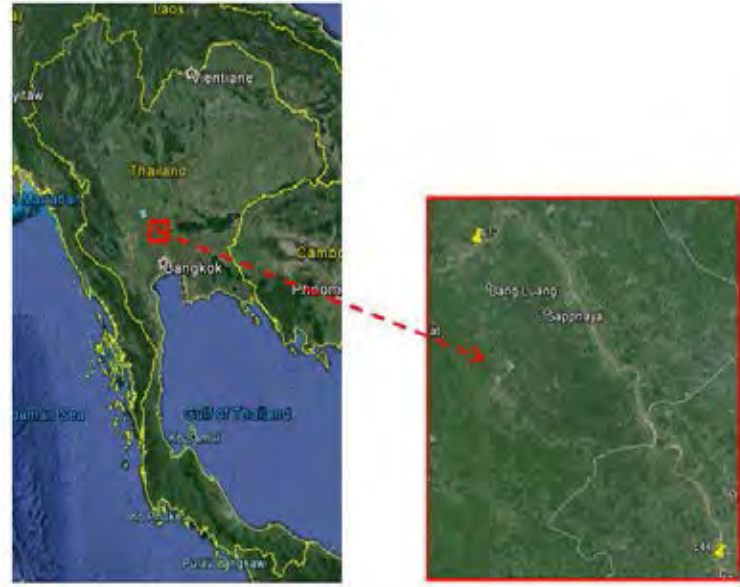


Figure 5.17: The studied area, the Chao Phraya river at Chai Nat to Sing Buri provinces, Thailand.

Since the initial condition in our simulation is not trivial, we simulate two different cases of initial conditions with the grid resolution $\Delta x = 90$ m, $\Delta y = 90$ m and time step $\Delta t = 5$ s. For the first case, we assume the whole domain to be dry and we allow the water flows along the Chao Phraya river using the water depth and velocity at c13 station. For the second case, we assume the domain is already flooded. By collecting the data from the satellite image on October 15, 2011 and the water depth data on the same day at c13 and c44 stations, we can fill the water depth to the land to be the same value as the measurement data.

	13 Oct 2011	14 Oct 2011	15 Oct 2011	16 Oct 2011	17 Oct 2011
water height (<i>m</i>)	17.59	17.57	17.56	17.55	17.55
discharge (m^3/s)	3534.2	3522.6	3516.8	3511	3511

Table 5.5: The measurement data of water heights and discharges average per day at c13 station on October 13-17, 2011.

For the first case, the initial water depth is set to be dry for the whole domain. Water is released from a source along the river where the water depth and its discharge are set to be the same values as the data obtained from the c13 station on October 13-17, 2011 [54]. Details are shown in table (see Table 5.5). Then, we consider five days simulation on October 13-17. We compare the discrepancy on the last day where the water distribution from the satellite image on October 17 is shown in Figure 5.18(a). The simulation result on the same day is shown in Figure 5.18(b). The difference between real and simulation results on the lower part of the river is shown in Figure 5.18(c). The comparison is only made on the left of the river as specified by the pink-shaded area of Figure 5.18(c). The flood simulation in this case is due to the massive source of water from the river that flows over to the lower land area. The agreement between real and simulation results is shown. It should be noted that the flooded area on the right or on the top of the river appears. This situation is from the other sources of water over the land that are not included initially in our simulations. Thus, we can see the flooded area only on the lower part of the river.

15 to 17, and is compared with the real data from the satellite image again on October 17.

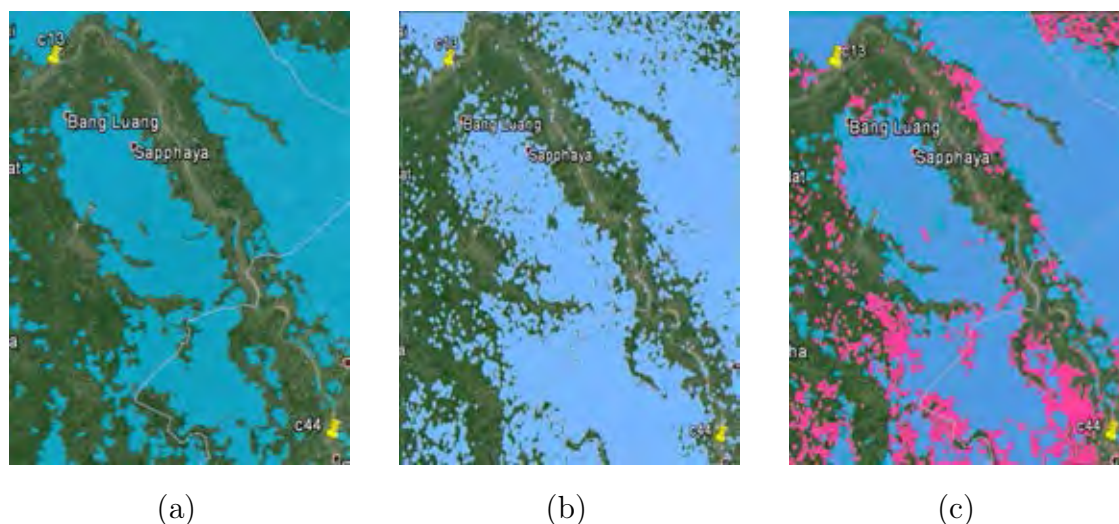


Figure 5.20: The initial water distribution on October 15, 2011. (a) The real data from satellite image on October 15, 2011. (b) The assumed initial water distribution on October 15, 2011. (c) The difference (pink) between real data from satellite image and the assumed initial water distribution.

The results from the numerical simulation (Figure 5.21(b)), the satellite image on October 17 (Figure 5.21(a)) and the difference between the satellite image and the numerical simulation (Figure 5.21(c)) show the agreement of the simulation result and the real data. As seen in the simulation result, after 2 days, the distribution of water area is enlarged similar to that from the satellite image. Some of the water from the river has flowed to cover the lower land next to the river on previously dry areas, this occurred in area indicated by the yellow frame in Figure 5.21(c).

The numerical simulation from the two cases of initial condition agree with the real data from the satellite image as discussed above. These results from Figures 5.18, 5.19 and 5.21 show that the developed scheme is quite capable of simulating real floods for this area, where the accuracy is quite reasonable.

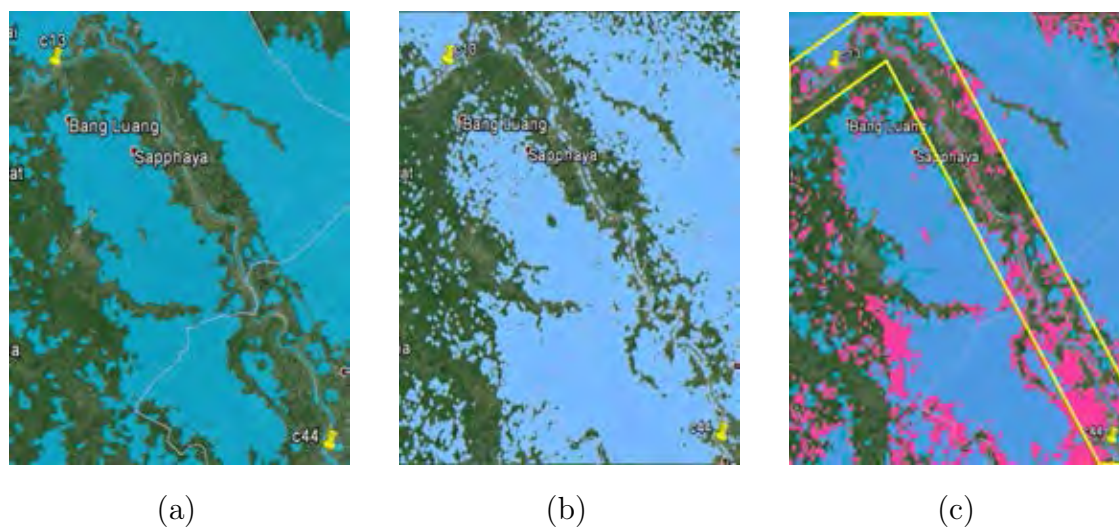


Figure 5.21: The results on October 17, 2011. (a) The real data from satellite image on October 17, 2011. (b) The simulation result on October 17, 2011. (c) The difference (pink) between real data from satellite image and the simulation result.

5.6 Conclusions

A well-balanced FVM with the WAF is developed in this work to simulate water flows such as dam break and flood. Combining with semi-implicit scheme for estimating friction source terms yields an efficient numerical method for simulating shallow water flows for both wet and dry beds. Importantly, we improve the scheme to have the second-order accuracy for smooth flow by applying the linear reconstruction. The wet/dry cell tracking technique is also employed to reduce the computational time for problems with the less wetted area by calculating just the updated wet cells. The accuracy of our numerical scheme is investigated by various numerical experiments including one- and two-dimensional problems. The scheme is shown to be well-balanced by demonstrating that it exhibits the exact C-property as described in the numerical experiment 5.5.5. Moreover, the validity and accuracy of the scheme is illustrated in the experiments 5.5.6-5.5.8 for flows with friction and bottom slope, by comparison to other results in literature. It is

also shown by numerical evidences that the present scheme can preserve mass and non-negativity of the water depth during time integration. For real applications, the developed scheme is applied to simulate the great flood which occurred in Thailand, 2011. The numerical simulations show results that agree with the existing data obtained from satellite images. All of these experiments have demonstrated that the presented scheme is capable of simulating various kinds of shallow water problems with accuracy and efficiency.

CHAPTER VI

CONCLUSIONS

In this dissertation, we have developed three numerical schemes for solving the SWE. The first scheme, see Chapter III, is the TVD-RK DG method with WAF for one-dimensional SWE, which is shown to be consistent. In addition, the scheme is modified to be well-balanced and used to simulate various steady and unsteady flows.

The second scheme, see Chapter IV, is developed to obtain more realistic results for the one-dimensional flow, where the one-dimensional SWE is considered for arbitrary cross-sectional areas, based on the FVM. In this scheme, the reconstruction and bottom modification techniques is applied to handle the difficulty of the dry area. The developed scheme is shown to be accurate when compared with the known results in literature and preserve the still water stationary solution. This scheme is also applied to simulate the real river flow for the Yom river in Phrae province, Thailand, from August 27 to September 10, 2014.

The third scheme, see Chapter V, is developed to real world flows by considering the two-dimensional SWE, based on the well-balanced FVM with WAF. The scheme is improved to be more efficient by combining with the splitting implicit technique for estimating friction source term and applying the linear reconstruction to have second-order accuracy for smooth flows. In addition, the wet/dry tracking technique is employed to reduce the computational time. The accuracy of the scheme is confirmed by various numerical experiments when compared with exact solutions or known results in literature and the scheme is applied to simulate the great flood which occurred in Thailand, 2011.

REFERENCES

- [1] Anastasiou K., Chan C. T.: Solution of the 2D shallow water equations using the finite volume method on unstructured triangular meshes, *Int. J. Numer. Meth. Fluids.* **24**, 1225–1245 (1997).
- [2] Ata R., Pavan S., Khelladi S., Toro E. F.: A weighted average flux (WAF) scheme applied to shallow water equations for real-life applications, *Adv. Water Resour.* **62**, 155–172 (2013).
- [3] Audusse E., Bouchut F., Bristeau M. O., Klein R., Perthame B.: A fast and stable well-balanced scheme with hydrostatic reconstruction for shallow water flows, *SIAM J. Sci. Comput.* **25**, 2050–2065 (2004).
- [4] Aureli F., Mignosa P., Tomirotti M.: Numerical simulation and experimental verification of dam-break flows with shocks, *J. Hydraul. Res.*, **38**, 197–206 (2010).
- [5] Bermudez A., Vazquez M. E.: Upwind methods for hyperbolic conservation laws with source terms, *Comput. Fluids.* **23**, 1049–1071 (1994).
- [6] Billett S. J., Toro E. F.: On WAF-type schemes for multidimensional hyperbolic conservation laws, *J. Comput. Phys.* **130**, 1–24 (1997).
- [7] Cockburn B., Shu C. W., Johnson C., Tadmor E.: *Advanced numerical approximation of nonlinear hyperbolic equations in Lectures given at the 2nd session of the Centro Internazionale Matematico Estivo (C.I.M.E.) held in Cetraro, Italy, June 23-28, 1997*, Springer Verlag, Telos, (1998).
- [8] Crossley, A. J.: *Accurate and efficient numerical solutions for the Saint Venant equations of open channel flow*, Ph.D. Thesis, University of Nottingham, 1999.
- [9] Cunge J. A., Holly F. M., Verwey A.: *Practical aspects of computational river hydraulics*, Pitman Advanced Publishing Program, 1980.
- [10] Delestre O., Lucas C., Ksinant P.-A., Darboux F., Laguerre C., Tuoi Vo F., Cordier S.: SWASHES: a compilation of shallow water analytic solutions for hydraulic and environmental studies, *Int. J. Numer. Meth. Fluids.*, 346–365 (2012).
- [11] Fernández-Nieto E.D., Narbona-Reina G.: Extension of WAF type methods to non-homogeneous shallow water equations with pollutant, *J. Sci. Comput.* **36**, 193–127 (2008).

- [12] Gallouët T., Hérard J. M., Seguin N.: Some approximate Godunov schemes to compute shallow-water equations with topography, *Comput. Fluids.*, **32**(2003), 479–513 (2003).
- [13] Harten A., Lax P.D., Van Leer B.: On upstream differencing and Godunov-type schemes for hyperbolic conservation laws, *SIAM Rev.*, **25**, 36–51 (1983).
- [14] Harten A., Tal-Ezer H.: On a fourth order accurate implicit finite difference scheme for hyperbolic conservation laws.II five-point Scheme, *J. Comput. Phys.* **41**, 329–356 (1981).
- [15] Hesthaven J. S., Warburton T.: *Nodal Discontinuous Galerkin Methods: Algorithms, Analysis, and Applications*, Springer, 2008.
- [16] Kantadong N.: *Flood Warning of Yom River in Amphur Mueng Phrae Using a Hydrodynamic Model*, Master's Thesis, Chiang Mai University, 2005.
- [17] Kesserwani G., Liang Q.: Well-balanced RKDG2 solutions to the shallow water equations over irregular domains with wetting and drying, *Comput. Fluids.* **39**, 2040–2050 (2010).
- [18] Kesserwani G., Liang Q.: A discontinuous Galerkin algorithm for the two-dimensional shallow water equations, *Comput. Methods Appl. Mech. Engrg.* **199**, 3356–3368 (2010).
- [19] Khan A. A., Lai W.: *Modeling Shallow Water Flows Using the Discontinuous Galerkin Method*, CRC Press, 2014.
- [20] Lai W., Bouchut A. A.: Discontinuous Galerkin method for 1D shallow water flow with water surface slope limiter, *Int. J. Civil and Env. Eng.* **3**, 167–176 (2011).
- [21] Lai W., Khan A. A.: Discontinuous Galerkin method for 1D shallow water flow in nonrectangular and nonprismatic channels, *J. Hydraul. Eng.* **138**, 285–296 (2012).
- [22] Lai W., Khan A. A.: Discontinuous Galerkin method for 1D shallow water flows in natural rivers, *Eng. Appl. Comp. Fluid.* **6**, 74–86 (2012).
- [23] Leveque R. J.: *Numerical Methods for Conservation Laws*, Birkhäuser Verlag Press, 1992.
- [24] Leveque R. J.: Balancing source terms and flux gradients in high-resolution Godunov methods: The quasi-steady wave-propagation algorithm, *J. Comput. Phys.* **146**, 346–365 (1998).

- [25] Leveque R. J.: *Finite Volume Method for Hyperbolic Problem*, Cambridge University Press, 2005.
- [26] Liang Q.: Flood simulation using a well-balanced shallow flow model, *ASCE J. Hydraul. Eng.*, **136**, 669–675 (2010).
- [27] Liang Q., Borthwick A. G.L.: Adaptive quadtree simulation of shallow flows with wet-dry fronts over complex topography, *Comput. Methods Appl. Mech. Engrg* **38**, 221–234 (2009).
- [28] Loukili Y., Soulaïmani A. W.: Numerical tracking of shallow water waves by the unstructured finite volume WAF approximation, *Int. J. Comput. Methods Eng. Sci. Mech.* **8**, 75–88 (2007).
- [29] Maleewong M.: Modified predictor-corrector WAF method for the shallow water equations with source terms, *Math. Prob. Eng.*, 1–17 (2011).
- [30] Murillo J., García-Navarro P.: Accurate numerical modeling of 1D flow in channels with arbitrary shape. Application of the energy balanced property, *J. Comput. Phys.* **260**, 222–248 (2014).
- [31] Noelle S., Pankratz N., Puppo G., Natvig J. R.: Well-balanced finite volume schemes of arbitrary order of accuracy for shallow water flows, *J. Comput. Phys.* **213**, 474–499 (2006).
- [32] Ozmen-Cagataya H., Kocamanb S.: Dam-break flow in the presence of obstacle: experiment and CFD simulation, *Eng. Appl. Comp. Fluid.* **5 (4)**, 541–552 (2011).
- [33] Pongsanguansin T.: *Adaptive Discontinuous Galerkin Method for One-dimensional Shallow Water Equations*, Master’s Thesis, Chulalongkorn University, 2011.
- [34] Sanders B. F.: Integration of a shallow water model with a local time step, *J. Hydraul. Res.* **46 (4)**, 466–475 (2008).
- [35] Schwanenberg D., Kiem R., Kongeter J.: A discontinuous Galerkin method for the shallow-water equations with source terms. Discontinuous Galerkin Methods: Theory, Computations and Applications, B. Cockburn, G. E. Karniadaki, and C.-W. Chu, Eds. in *Lecture Notes in Computational Science and Engineering*, Springer, 1419–424 (2000).
- [36] Shu C. W.: Total variation diminishing time discretizations, *SIAM J. Sci. Stat. Comput.* **9**, 1073–1084 (1988).

- [37] Tassi P. A., Vionnet C. A.: Discontinuous Galerkin method for the one dimensional simulation of shallow water flows, *Mecànica Computational Vol. XXII, Bahía Blanca*. **22**, 2403–2428 (2003).
- [38] Toro E. F.: A weighted average flux method for hyperbolic conservation laws, *Proc. R. Soc. Lond. A*. **423**, 401–418 (1989).
- [39] Toro E. F.: Riemann problems and the WAF method for solving the two-dimensional shallow water equations, *J. Philos. Trans. R. Soc. London Ser.* **338**, 43–68 (1992).
- [40] Toro E. F.: *Riemann Solvers and Numerical Methods for Fluid Dynamics: A Practical Introduction*, Springer, 1999.
- [41] Toro E. F.: *Shock-Capturing Methods for Free-Surface Shallow Flows*, John Willy and sons LTD, 2001.
- [42] Toro E. F., Roe P. L.: A hybridised high-order random choice method for quasi-linear hyperbolic systems, edited by Gronig, *Proc. 16th Intern Symp. on Shock Tubes and Waves*, Aachen, Germany, 701–708 (1987).
- [43] Triki A.: A finite element solution of the unidimensional shallow-water equation, *J. Appl. Mech* **80(2)**, 1–8 (2013).
- [44] Van Leer B.: Toward the ultimate conservation difference scheme ii., *Comput. Phys.***14**, 361–376 (1974).
- [45] Van Leer B.: Toward the ultimate conservation difference scheme v., *Comput. Phys.***32**, 1–136 (1979).
- [46] Vosoughifar H-R., Dolatshah A., Shokouhi S-K.S.: Discretization of multi-dimensional mathematical equations of dam break phenomena using a novel approach of finite volume method, *J. Appl. Math.*, 1–12 (2013).
- [47] Xing Y., Shu C. W.: High order well-balanced finite volume WENO schemes and discontinuous Galerkin methods for a class of hyperbolic systems with source terms, *J. Comput. Phys.* **214**, 567–598 (2006).
- [48] Xing Y., Shu C. W.: High-order finite volume WENO schemes for the shallow water equations with dry states, *Adv. Water Resour.*, **34**, 1026–1038 (2011).
- [49] Xu Z., Xu J., Shu C. W.: A high order adaptive finite element method for solving nonlinear hyperbolic conservation laws, *Technical Report 2010-14*, Scientific Computing Group, BrownUniversity, Providence, RI, USA, Apr., (2010).
- [50] Ying X., Wang S. S. Y.: Improved implementation of the HLL approximate Riemann solver for one-dimensional open channel flows, *J. Hydraul. Res.*, **46**, 21–34 (2008).

- [51] Ying X., Wang S. S. Y.: Improved HLL scheme for 1D dam-break flows over complex topography, *Arch. Hydro-Eng. Environ. Mech.*, **57**, 31–41 (2010).
- [52] <http://www.gistda.or.th>
- [53] <http://www.hydro-1.net/>
- [54] <http://www.hydro-5.com>
- [55] <http://srtm.csi.cgiar.org>

VITA

Name	Thida Pongsanguansin
Date of Birth	16 October 1986
Place of Birth	Bangkok, Thailand
Education	B.Sc. (Mathematics, First Class Honors) Kasetsart University, 2009 M.Sc. Chulalongkorn University, 2011
Scholarship	Science Achivement Scholarship Thailand (SAST)
Proceeding	Pongsanguansin T., Mekchay K., Maleewong M.: Adaptive Discontinuous Galerkin Method for One-Dimensional Advection Equation. <i>Annual Pure and Applied Mathematics Conference</i> , 41-56 (2011).
Publication	1) Pongsanguansin T., Mekchay K., Maleewong M.: Adaptive TVD-RK discontinuous Galerkin algorithms for shallow water equations, <i>International Journal of Mathematics and Computers in Simulation</i> 6(2) , 257–273 (2012). 2) Pongsanguansin T., Maleewong M., Mekchay K.: Consistent weighted average flux of well-balanced TVD-RK discontinuous Galerkin method for shallow water flows, <i>Modelling and Simulation in Engineering</i> , 1–11 (2015). 3) Pongsanguansin T., Maleewong M., Mekchay K.: Shallow-water simulations by a well-balanced WAF finite volume method: a case study to the great flood in 2011, Thailand, <i>Computational Geosciences</i> 20(6) , 1269–1285 (2016).